Print ISSN 0033-9008
Online ISSN 1880-1765

QUARTERLY REPORT of RTRI

Feb. 2026 Vol. 67 No. 1

CONTENTS

[H] Human factors
[I] Infrastructure
[N] Natural hazards
[O] Operations
[R] Rolling stock
[T] Technical system integration and interaction

RAILWAY TECHNICAL RESEARCH INSTITUTE

QUARTERLY REPORT of RTRI

Print ISSN 0033-9008
Online ISSN 1880-1765

February 2026 Vol. 67 No. 1

CONTENTS

PAPERS

SUMMARIES

[H] Human factors
[I] Infrastructure
[N] Natural hazards
[O] Operations
[R] Rolling stock
[T] Technical system integration and interaction

Identifying Sources of Unpleasant Odors in Men's Railway Station Restrooms and Verifying Effectiveness of Countermeasures to Reduce Those Odors

Takashi KYOTANI
Comfort Science and Engineering Laboratory, Human Science Division

Akiko KAMEDA
East Japan Railway Company

Tsuyoshi UEDA
New Cosmos Electric co., ltd.

Tamami KAWASAKI
Comfort Science and Engineering Laboratory, Human Science Division

Unpleasant odors in restrooms in railway stations and on trains are one of the objects of many complaints from railway customers. Therefore, countermeasures to reduce these unpleasant odors are required. In railway station restrooms, we are investigating the sources of ammonia, one of the main compounds responsible for unpleasant odors in public restrooms. To conduct this investigation, we developed a prototype of a portable, highly sensitive ammonia measuring instrument. We used this instrument to search for sources of ammonia in men's railway station restrooms and confirmed the difference in concentration of ammonia depending on cleaning methods and seasons. In addition, we verified the effectiveness of countermeasures implemented by cleaning companies to reduce unpleasant odors.

***Key words*:** *restrooms in railway stations, odor, high-sensitivity ammonia measuring instrument, source, countermeasures to reduce unpleasant odors*

1. Introduction

From the perspective of improving passenger services, providing comfortable environment in railway stations and trains for customers is extremely important. Among them, unpleasant odors in station and train restrooms are one of the objects of many complaints from railway customers. The authors previously conducted a survey on railway customer perceptions of the quality of cleaning in men's station restrooms. Results revealed that "odor satisfaction" is one of the evaluation indicators that affect customer decision to use the same station restroom again [1]. Specifically, we found that as improved "odor satisfaction," more customers would like to use the same restroom again. These findings suggest that reducing unpleasant odors in station and train restrooms can improve restroom environments for customers.

Railway operators are already implementing countermeasures to reduce unpleasant odors in restrooms and improve air quality. These include replacing "wet cleaning" (using water) with "dry cleaning" (not using water) methods (hereinafter, we refer to this change as "dry conversion"). This countermeasure suppresses the growth of bacteria by eliminating the use of water, because one of the causes of ammonia (hereinafter referred to as "NH_3"), a key component of unpleasant odors in restrooms, is the bacteria decomposition of urine stains [2, 3, 4]. There are reports indicating that dry conversion reduces unpleasant odors [5, 6]. Results of the abovementioned survey also revealed that station restrooms using dry cleaning received significantly better odor evaluations than those using wet cleaning [1].

Sources of NH_3 in men's station restrooms have been investigated to identify areas where cleaning companies should concentrate on odor countermeasures and improve cleaning efficiency. Initially, NH_3 detection tubes were used (detection tube method [7]), but the detection limit of the detection tubes (200 ppb) is higher than the human detection threshold concentration (100 ppb [8]) (Table 1). This meant that sources of NH_3 could not always be identified, even when people could smell the odors of the restroom, as the concentrations of NH_3 in the air or near the floor were undetectable. Therefore, we required a sensor capable of detecting concentrations of NH_3 below the human detection threshold. We focused on an NH_3 sensor element with approximately 20 times the sensitivity of conventional NH_3 detection tubes. This element was developed for breath sensors aimed at early detection of various diseases by detecting trace amounts of NH_3 in exhaled breath (Table 1) [9, 10]. We collaborated with a manufacturer to prototype a portable, highly sensitive NH_3 measurement instrument equipped with this NH_3 sensor element (See Chapter 2) [11].

Using this instrument, we identified sources of NH_3 and measured their concentration in men's station restrooms. We also investigated optimal cycle for dry cleaning as a countermeasure to reduce unpleasant odors and evaluated their effectiveness of countermeasures implemented by cleaning companies commissioned by railway operators. In this paper, we report on the results of these studies.

Table 1 Detection limit for ammonia using detection tube method and high-sensitivity NH_3 measuring instrument

Detection method	Lower limit of detection concentration of NH_3
Detection tube method	200 ppb
High-sensitivity NH_3 measurement instrument	10 ppb

Human detection threshold concentration: 100 ppb [8]
(Equivalent to odor intensity 1)

2. High-sensitivity NH_3 measurement instrument

2.1 Overview of the high-sensitivity NH_3 measurement instrument

Figure 1 shows the prototype of the high-sensitivity NH_3 measurement instrument used in this study (hereinafter, we refer to as "the instrument"). The instrument consists of a main unit incorporating an NH_3 sensor and a suction pump (suction flow rate: 2.6 L/min), a silicon tube, a three-way valve, a stainless-steel suction tube (inner diameter: 6 mm, length: 1 m), and a data logger. By switching the flow path of the three-way valve, an operator can select either sample air or purified air passed through an activated carbon tube to be sucked into the main unit. When sampling air, the tip of the suction tube is moved while continuously sucking in the target air and the sensor response is recorded. A person taking the measurement can check the sensor response on the data logger display.

2.2 Floor NH_3 source identification and concentration measurement method

When searching for sources of NH_3 on the floor, we moved the suction tube tip at a speed of approximately 5 cm/sec, around 1 cm above the floor surface inside the men's restroom, while continuously sampling the air in a sweeping motion (Fig. 2). During the search, we monitored the sensor response on the data logger display and recorded the location where the response peaked as the source of NH_3. Once scanning was completed, we calculated the concentration of NH_3 using the sensor response value at the source of NH_3 and the previously created calibration curve (Fig. 3).

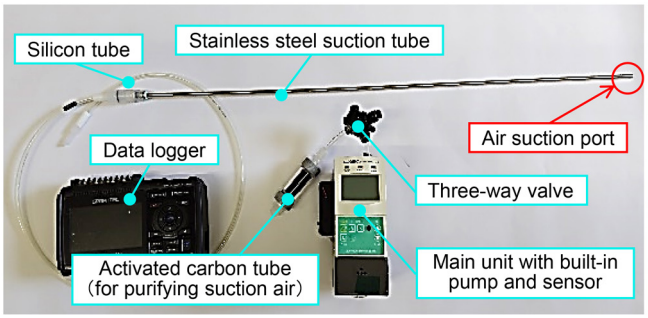

Fig. 1 High-sensitivity NH_3 measuring instrument

Fig. 2 Use of high-sensitivity NH_3 measuring instrument in men's station restroom

2.3 NH_3 concentration measurement method in the space inside the restroom

When sampling the air inside the restroom, we connected a 15 cm long suction tube (inner diameter: 6 mm) to a silicone tube instead of a 1 m long suction tube and continuously sampled the air at a height of approximately 150 cm above the floor in the same manner as the floor. Confirmation of sensor responses, recording of peak positions, and calculation of NH_3 concentration were performed in the same manner as described in Section 2.2.

3. Odor survey in men's station restrooms

3.1 Identification of sources of NH_3 in men's station restrooms

Using the instrument, we searched the sources of NH_3 on the floors of the men's restrooms in Stations A and B in the Tokyo metropolitan area, using the method described in Section 2.2. We conducted this survey in spring and summer and examined the differences in the test results. Table 2 shows the cleaning methods and finishes used for the floors of the men's restrooms in both stations, and Fig. 4 shows schematic diagrams of those restrooms.

The results of this survey revealed multiple peaks in sensor responses within the red-framed area in Fig. 4, indicating the presence of multiple sources of NH_3 within that area. Common sources of NH_3 in both restrooms were near handrail-equipped urinals and gutters beneath wash basins. Additional sources of NH_3 found in the Station A restroom were in front of urinals not equipped with handrails, and in the Station B restroom was in a gutter installed in front of the urinals.

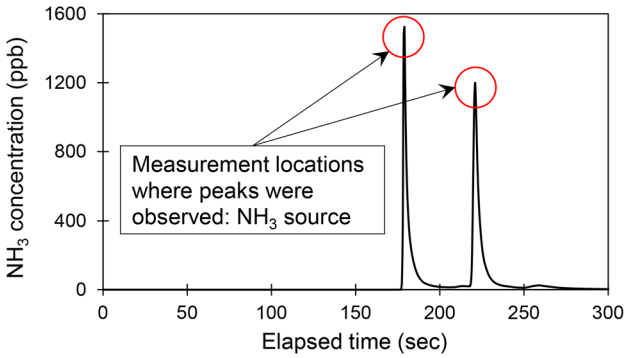

Fig. 3 Example of measurement data obtained using instrument

Table 2 Floor cleaning method, floor finish, and survey date

Station	A	B
Floor cleaning method	Dry	Wet
Floor finish	Rubber tiles	Porcelain tiles (Joints are used)
Survey date	(Spring) 2021.4.26-27 (Summer) 2021.7.20-21	

3.2 Differences in NH_3 concentration depending on cleaning methods and season

For restrooms in Stations A and B, we calculated the average concentration of NH_3 for the multiple sources identified in Section 3.1 and compared the results by season (spring and summer). These results are shown in Fig. 5. The error bars in Fig. 5 indicate the standard deviation. In both restrooms, the average NH_3 concentration tended to be higher in summer than in spring. Additionally, regardless of the season, the average NH_3 concentration tended to be higher in the Station B restroom with wet cleaning than in the Station A restroom with dry cleaning.

In Fig. 5, the vertical axis shows the average concentration of NH_3. If all concentrations from multiple sources were at this value, detection tubes would not detect NH_3 except in the Station B restroom in summer. Furthermore, in the Station A restroom, it was not possible to identify the source of NH_3 regardless of whether it is spring or summer.

From the results described in Section 3.1 and the above findings, continuous measurements of NH_3 near the floor surface of actual restrooms in stations using the instrument revealed the presence of multiple sources of NH_3. Depending on the position and timing of measurement, concentrations of NH_3 were too low to be detected by the detection tube method and were at levels imperceptible to humans.

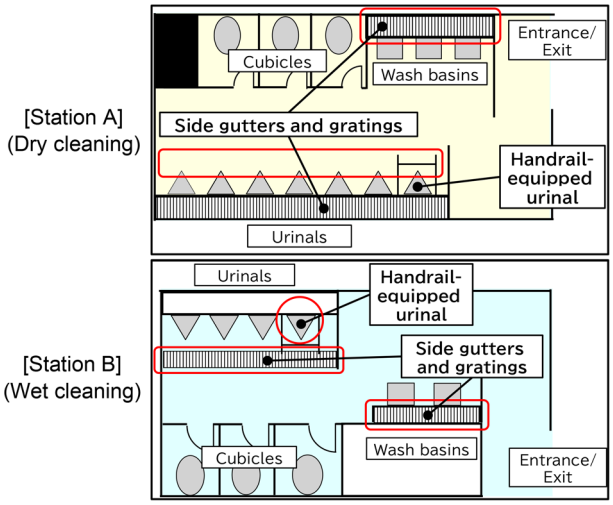

Fig. 4 Sources of NH_3 on the floor of the men's restroom at Stations A and B (Red frames: positions of sources of NH_3)

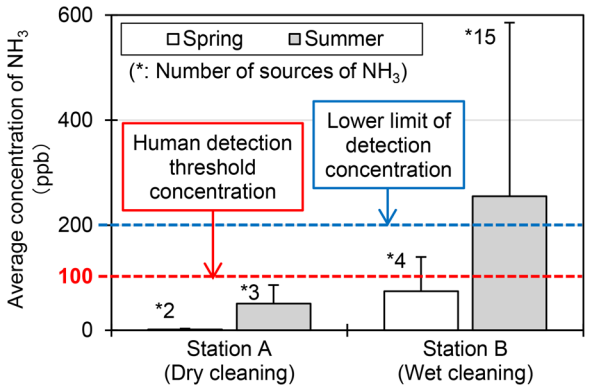

Fig. 5 Average concentration of NH_3 for the multiple sources on the floor of the men's restroom at Stations A and B shown in Fig. 4

4. Verification of the effectiveness of countermeasures to reduce unpleasant odors

There are two main types of countermeasures to reduce unpleasant odors in station restrooms: those implemented by railway operators and those implemented by cleaning companies commissioned by railway operators. One of the measures implemented by railway operators is a skirting board ventilation system (Fig. 6) that exhausts unpleasant odors generated around urinals before they reach nose height. This measure needs to be considered from the design stage when installing or renovating station restrooms and involves major construction work when implemented. In contrast, cleaning companies commissioned by railway operators implement measures such as dry conversion in restrooms with wet cleaning and gutter cleaning. These measures are implemented by cleaning companies during their regular cleaning operations and do not require restroom installation or renovation.

However, until now, the effectiveness of these measures has depended on human olfaction, making it impossible to objectively evaluate the extent to which unpleasant odors have been reduced.

Therefore, we used the instrument to monitor changes in concentration of NH_3 over time before and after implementing these countermeasures in this study, thereby verifying the effectiveness of reduction of unpleasant odors. This paper presents two case studies verifying the effectiveness of countermeasures implemented by cleaning companies to reduce those odors.

4.1 Dry conversion in a men's restroom

The first case study is an example of verifying the effectiveness of dry conversion in a men's restroom. Figure 7 shows a schematic diagram of the men's restroom in Station C, which was the subject of the verification. The floor consists of ceramic tiles and joints, with three drains. Note that there is no skirting board ventilation system as shown on Fig. 6.

4.1.1 Method of dry conversion and verification of effectiveness the countermeasure to reduce unpleasant odors

After interviewing the cleaning company contracted by the railway operator to perform cleaning in Station C, we investigated

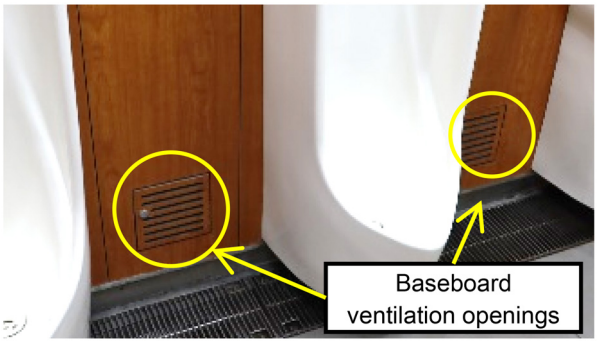

Fig. 6 The example of baseboard ventilation opening (the same restroom as shown in Fig. 11)

how to implement efficient and effective cleaning without modifying the existing equipment, such as changing the floor finish. We then narrowed down the measures to the following two cleaning methods and compared their effects with that of conventional wet cleaning (hereinafter referred to as "conventional cleaning"). These measures do not involve sprinkling water on the floor and can therefore be considered a type of dry cleaning. Verification took place over a period of three days, from July 19 to 21, 2022 (Table 3).

Countermeasure cleaning A: Use a dry mop to wipe urine stains, etc., without sprinkling water.
Countermeasure cleaning B: Spray a solution of detergent diluted 100 times with water, then wipe with a dry mop.

Prior to the cleaning work on the first day, we identified the sources of NH_3 using the method described in Section 2.2. The cleaning work was carried out as follows: on the first day, conventional cleaning; on the second day, countermeasure cleaning A; and on the third day, countermeasure cleaning B. This work was carried out at approximately the same time (11:00 to 12:00). We measured the concentrations of NH_3 at the identified sources and in the restroom space before and after cleaning, as well as two and four hours after cleaning (Table 3). As described in Section 2.3, we measured the entire space approximately 150 cm above the floor and recorded the maximum concentration of NH_3 (hereinafter referred to as "The concentration of NH_3 in space") along with the measurement location.

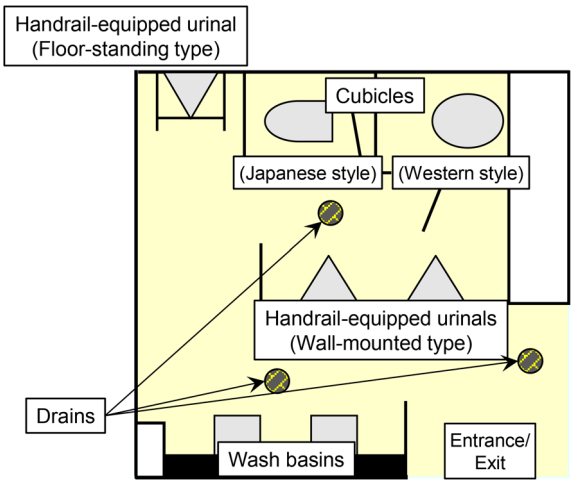

Fig. 7 The schematic diagram of a men's restroom at Station C

Table 3 Date and time of effectiveness verification for countermeasure cleaning (Station C)

Verification date	2022.7.19 - 21
Cleaning work	7.19: Conventional cleaning 7.20: Countermeasure cleaning A 7.21: Countermeasure cleaning B
Verification time	10:00 (Before cleaning) 12:00 (Immediately after cleaning) 14:00 (2 hours after cleaning) 16:00 (4 hours after cleaning)

4.1.2 Verification results

The sources of NH_3 identified on the first day of verification were the following four locations. Figure 8 shows the specific locations of each source.

Source 1: The ground contact area between the rear right corner of the floor-mounted urinal with a handrail and the floor
Source 2: The ground contact area between the front of the same urinal and the floor
Source 3: The floor in front of the same urinal
Source 4: The drain in front of cubicles

Note that the location where the maximum concentration of NH_3 in space was measured was near Source 3 at all verification times.

Figure 9 shows the results comparing the effects of reduction of concentration of NH_3 by cleaning. We will discuss the results for each measurement location below.

First, we discuss the concentration of NH_3 in space. As shown in Fig. 9 (a), the concentration of NH_3 rose to approximately 250 ppb four hours after conventional cleaning. The level was the same as before cleaning. In contrast, in countermeasure cleanings A and B, the concentration was approximately 250 ppb before cleaning and approximately 50 ppb four hours after cleaning. Additionally, as shown in Fig. 9 (b), the reduction rate of the concentration of NH_3 due to cleaning was higher for countermeasure cleanings A and B than conventional cleaning. From these results, we concluded that countermeasure cleanings A and B are more effective than conventional cleaning in reducing unpleasant odors for customers.

Secondly, we discuss the four sources of NH_3. For sources 1 and 2 (Fig. 9 (c) and (d)), we confirmed that the concentration of NH_3 was generally lower with countermeasure cleanings A and B than with conventional cleaning, although there were cases where the concentration ratio reversed over time from the start of cleaning. The areas where sources 1 and 2 are located, specifically the contact points between the urinals and the floor, are difficult to reach with mops. This makes it hard to remove dirt and can push it into surrounding areas. This is considered to be one of the reasons why the concentration ratio is reversed over time.

On the other hand, for source 3 (Fig. 9 (e)), the concentration of NH_3 decreased immediately after cleaning with all cleaning methods, but in conventional cleaning, it increased four hours after clean-

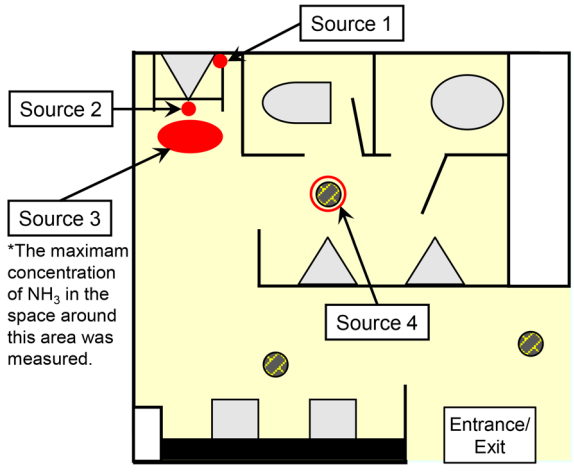

Fig. 8 Sources of NH_3 in a men's restroom at Station C

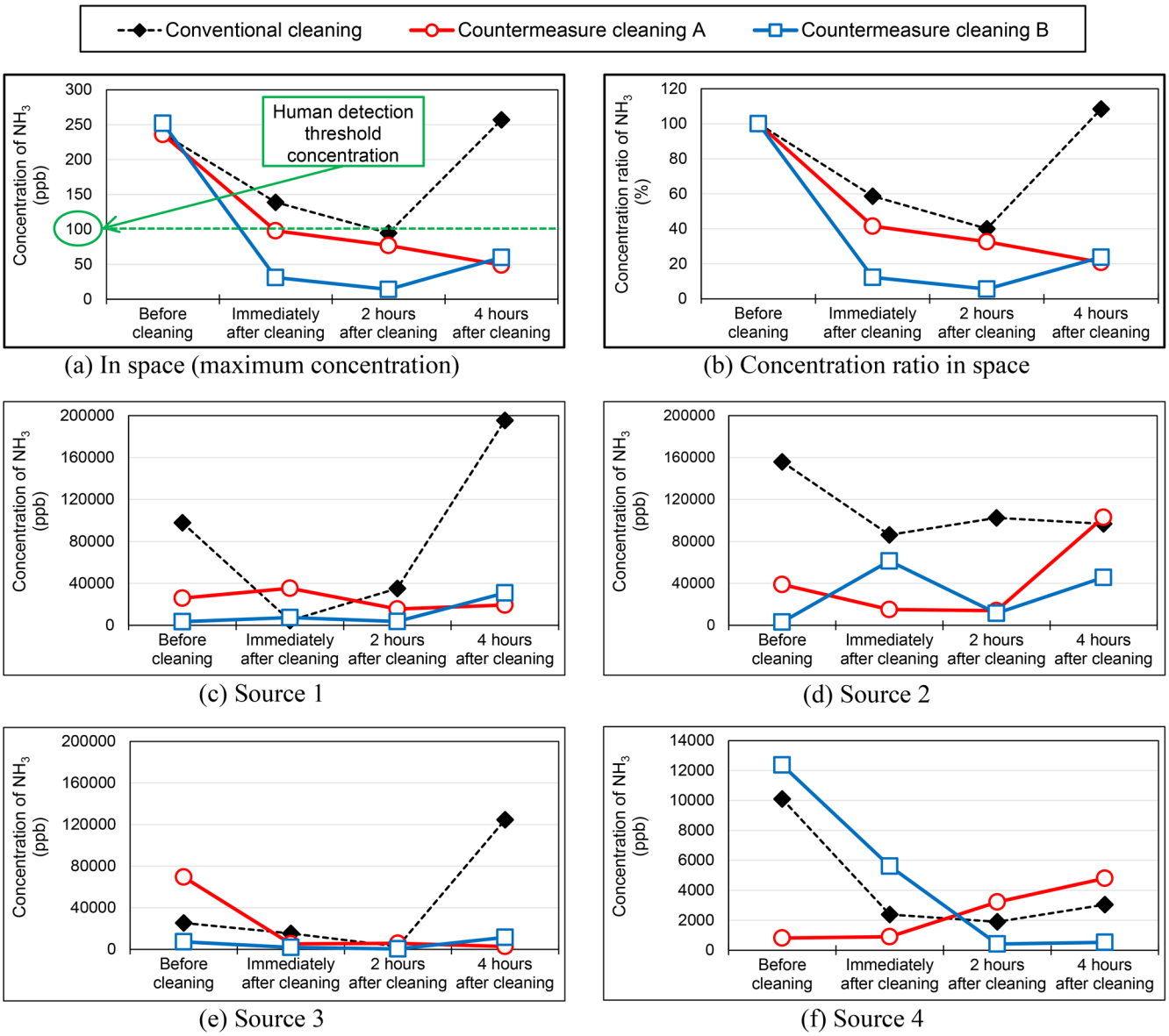

Fig. 9 Results of verifying the effectiveness of measures to reduce NH_3 through countermeasure cleaning (Station C)

ing and exceeded pre-cleaning levels. Source 3 is located on the floor in front of the urinal, making it the most likely location for new urine stains to appear among the four sources. Therefore, in conventional cleaning, residual moisture left behind after cleaning creates an environment where bacteria, including NH_3-producing bacteria, can grow. This is considered to be one of the causes of an increase in the concentration of NH_3 four hours after cleaning.

Finally, for source 4 (Fig. 9 (f)), in both conventional cleaning and countermeasure cleaning B, the concentration of NH_3 decreased immediately after cleaning. In countermeasure cleaning A, there was little change in the concentration of NH_3 before and after cleaning. Four hours after cleaning, the concentration of NH_3 was the lowest in countermeasure cleaning B.

Note that the detergent used in the countermeasure cleaning B is a neutral detergent containing a disinfectant. By applying this detergent to the floor surface, bacteria including NH_3-producing bacteria are killed, thereby creating an environment where NH_3 is less likely to be produced.

From the above analysis of the three cleaning methods compared in this study (conventional cleaning, countermeasure cleaning A and countermeasure cleaning B), we concluded that the countermeasure cleaning B, which involves spraying a detergent solution diluted 100 times and then wiping with a mop, is the most effective restroom maintenance method for odor control.

4.1.3 Daily cleaning cycle

Based on the results obtained in Section 4.1.2, we conducted a simple investigation to determine the optimal cycle for implementing countermeasure cleaning B on a daily basis. Specifically, once the studies described in Sections 4.1.1 and 4.1.2 had been completed, we requested that the same cleaning company replace the conventional cleaning conducted daily at 11:00 to 12:00 with countermeasure cleaning B. Approximately three months later, from October 27 to 28, we measured concentrations of NH_3 at source 3 shown in Fig. 8 and inside the restroom. The measurement times were set as follows: October 27 at 10:00 (before cleaning), every hour at 00 minutes from 12:00 to 16:00 (1 to 5 hours after cleaning),

and every hour at 00 minutes from 10:00 to 16:00 on the following day, October 28 (23 to 29 hours after cleaning) (Table 4). Additionally, after the implementation of the countermeasure cleaning B on October 27, we requested that the cleaning company refrain from any cleaning until this investigation was complete.

Figure 10 shows the results of the measurements of concentration of NH_3 at Source 3. Note that the concentration of NH_3 in space was below the detection limit (10 ppb) throughout the entire measurement period. Countermeasure cleaning B, implemented on the first day (added in red in Fig. 10), reduced the concentration of NH_3 at Source 3. Thereafter, the concentration remained at around 100 ppb on the day of cleaning, but it rapidly increased 23 hours after cleaning and reached its maximum 25 hours after cleaning (around 12:00). In this verification, the concentration of NH_3 in space was below the detection limit. However, depending on usage conditions and temperature, NH_3 exceeding the human olfactory threshold may diffuse into the space, which could cause discomfort to customers. From these results, we considered it is appropriate to start the daily cleaning cycle at around 11:00 (every 24 hours) as before. However, even in the same restroom in station C, usage conditions may vary from day to day, leading to different conclusions. Furthermore, the optimal time and cycle for daily cleaning in men's restrooms in different stations may differ from those in station C due to factors such as time-dependent changes in customer numbers. We plan to conduct further evaluations and periodically review the cleaning cycle to further improve the efficiency and rationalization of restroom maintenance operations.

Table 4 Date and time of daily cleaning cycle verification (Station C)

Date	2022.10.27-28
Cleaning work	10.27: Countermeasure cleaning B 10.28: (Not done)
Measurement time	<10.27> 10:30 (before cleaning) every hour at 00 minutes from 12:00 to 16:00 (1 to 5 hours after cleaning) <10.28> every hour at 00 minutes from 10:00 to 16:00 (23 to 29 hours after cleaning)

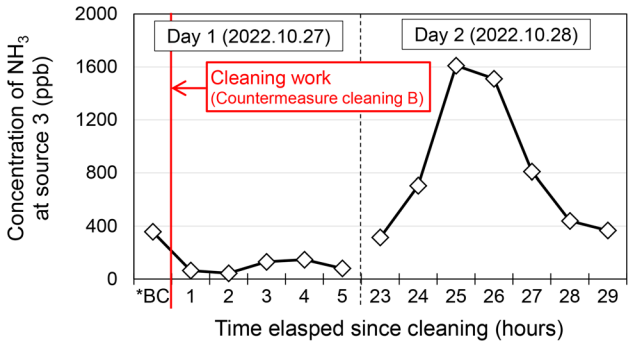

Fig. 10 Investigation into the cycle for implementing countermeasure cleaning B (Station C)
***BC: Before cleaning**

4.2 Cleaning of men's restroom gutters

The second case study demonstrates how cleaning gutters can reduce unpleasant odors in the men's restroom where the standard floor cleaning method is wet, like Station C. The floor of the restroom in Station D (Fig. 11), which was the subject of the verification, is made of ceramic tiles and joints, with gutters and gratings installed. The gutters are cleaned twice a week.

As described in Section 4.2.1 below, the investigation into the source of the odor revealed that it was located near the gutter. This led to the hypothesis that cleaning the gutters could also be an effective measure for odor control.

4.2.1 Verification Method

Using the instrument, we identified the source of NH_3 on the men's restroom floor in Station D and measured its concentration. Specifically, after identifying the source of NH_3 using the instrument, we carried out conventional cleaning, including the gutters. Measurements of concentration of NH_3 were carried out in the same manner as in Station C (Section 4.1), including before and after cleaning, as well as two and four hours after cleaning. These measurements targeted the identified sources of NH_3 and the space of the restroom. The methods used to measure and record the concentrations of NH_3 in space were also the same as in Station C. The verification was conducted on November 25, 2022.

4.2.2 Verification Results

From the result of investigating the source of NH_3, it was confirmed that the source of NH_3 was located near the gutters on both sides of a handrail-equipped urinal (sources 1 and 2 shown in Fig. 11). Furthermore, the location where the maximum concentration of NH_3 was measured remained near sources 1 and 2 throughout the measurements.

Figure 12 shows the results comparing the effects of reducing the concentration of NH_3 by cleaning. The concentrations of NH_3 before cleaning at sources 1 and 2 were 10,000 ppb, but they reduced to approximately 200 to 1,100 ppb immediately after cleaning. Additionally, two hours after cleaning, the concentration of NH_3 at source 2 increased to approximately 5,000 ppb, before reducing again to four hours after the cleaning. We believe that the re-in-

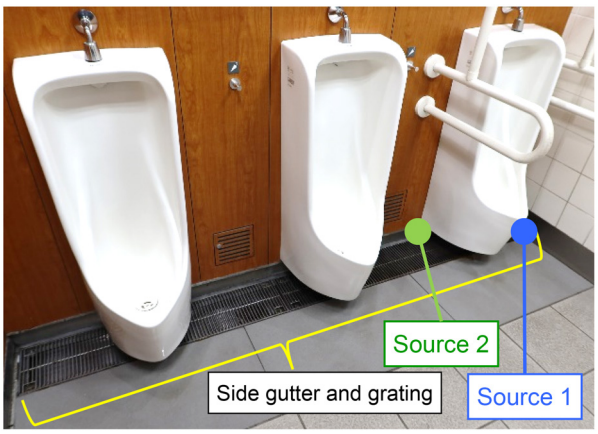

Fig. 11 Men's restroom at station D (Both sources 1 and 2 are located within the gutter.)

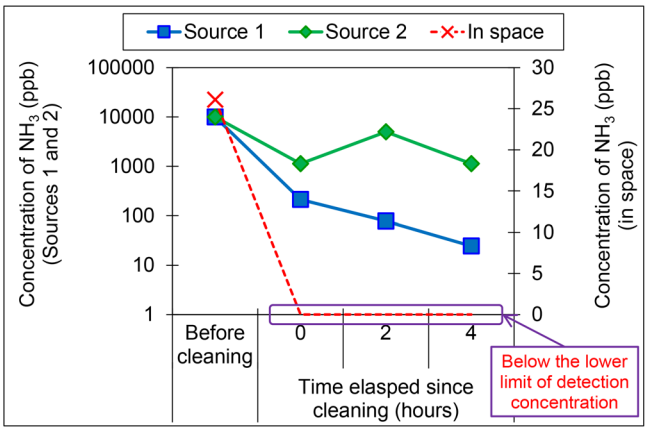

Fig. 12 Changes in NH_3 concentration of sources on the floor of the men's restroom at the station D and in space.

crease in concentration of NH_3 two hours after cleaning is due to new sources of NH_3 being generated by customers' urination after cleaning.

On the other hand, the maximum concentration of NH_3 in the space was 26 ppb before cleaning, but it decreased to below the detection limit immediately after cleaning and remained so for up to four hours. These results suggest that, even if new sources of NH_3 are temporarily generated due to customers' urination after cleaning of gutters, they do not significantly affect the concentration of NH_3 inside the restroom. As mentioned above, cleaning gutters is also an effective way of preventing unpleasant odors in station restrooms, like the dry conversion introduced in Section 4.1.

5. Summary

We developed a portable, high-sensitivity NH_3 measurement instrument equipped with an NH_3 sensor element approximately 20 times more sensitive than NH_3 detection tubes. We then used this instrument to identify the source of NH_3 and measure its concentration in men's restrooms in railway stations. We also investigated how concentration changes with measurement season and verified the effectiveness of countermeasures to reduce unpleasant odors. The results are presented below.

(1) At Station A with dry cleaning and Station B with wet cleaning, we identified sources of NH_3 on the floor and investigated the differences in concentration of NH_3 between spring and summer. The results indicated that the concentrations of NH_3 were higher in summer than in spring at both stations. Additionally, Station B showed higher concentrations of NH_3 than Station A, regardless of the season.

(2) As part of countermeasures to reduce unpleasant odors in station restrooms, we studied methods of converting wet-cleaning restrooms to dry-cleaning (countermeasure cleaning) and verified their effectiveness. The results showed that countermeasure cleaning, which involves spraying a 100-fold diluted detergent solution followed by mopping, is an effective method of maintaining restrooms from the perspective of odor control.

(3) In station restrooms equipped with gutters and gratings, we investigated the source of NH_3 and identified it as being located near the gutters. We then verified the effectiveness of the odor countermeasures by cleaning the gutters and confirmed their efficacy.

In this study, we measured the concentrations of NH_3 using the instrument in the men's restrooms in railway stations. As a result, we identified multiple sources of NH_3. Additionally, depending on the measurement location and season, the concentrations of NH_3 were found to be below the detection limit of the NH_3 detection tubes or below the human detection threshold. The effectiveness of two different unpleasant odor countermeasures methods was also verified using objective data on NH_3 concentrations, confirming their efficacy.

In Japan, where the population is steadily declining, labor-saving and manpower-saving measures in various industries, including railway operations. This is particularly the case for tasks such as cleaning and maintaining various facilities. The authors aim to improve the measurement instrument to make it easier and more convenient for cleaning companies and railway operators to use. This will enhance the effectiveness of the odor countermeasures they implement. This will, in turn, contribute to making public restrooms, including those in stations and trains, more pleasant.

This study was conducted in collaboration with New Cosmos Electric Co., Ltd.

This article is a reprint of the reference [12].

References

[1] Kyotani, T., Ikeda, Y., Oishi, H. and Kawasaki, T., "Survey of Railway Customer Perception of Men's Restroom Cleanliness in Railway Stations," *Quarterly Report of RTRI*, Vol. 66, No. 1, pp. 1-8, 2025. (DOI: https://doi.org/10.2219/rtriqr.66.1_1)

[2] Kawasaki, T., Kyotani, T., Ushiogi, T., Hayakawa, T., Kameda, A. and Sakamoto, K., "Research on Countermeasures to Reduce Unpleasant Odors in Toilets of Railway Stations (Part 2): Relationship between Concentrations of Bacteria and Ammonia on the Floor Tiles of Railway Station," *Annual Meeting of the Society of Indoor Environment*, pp. 60-61, 2012 (in Japanese).

[3] Kawasaki, T., Yoshie, S., Kyotani, T. and Ushiogi, T., "Comparison of Microbiomes on Floors of Men's Restrooms, before and after Cleaning with Different Cleaning Methods at Two Railway Stations," *Japan Architectural Review*, Vol. 5, No. 4, pp. 633-643, 2022. (DOI: https://doi.org/10.1002/2475-8876.12285)

[4] Kawasaki, T., Kyotani, T., Ushiogi, T and Yoshie, S., "Quantitative and Qualitative Research of Surface Bacteria on the Floor of Station Restrooms with Two Types of Cleaning Method," *Quarterly Report of RTRI*, Vol. 62, No. 4, pp. 281- 286, 2021. (DOI: https://doi.org/10.2219/rtriqr.62.4_281)

[5] Ikeda, Y, et al, "Study on cleaning method of dry process at railway station Part 1: Outline and result of laboratory survey," *Summary of Technical Papers of Annual Meeting, Environmental Engineering I, Architectural Institute of Japan,* pp. 591-592, 2015 (in Japanese).

[6] Ikebe, T., et al, "Study on cleaning method of dry process at railway station Part 2: Result of field survey," *Summary of Technical Papers of Annual Meeting, Environmental Engineering I, Architectural Institute of Japan,* pp. 593-594, 2015 (in Japanese).

[7] Japanese Industrial Standards, JIS K 0804, Gas detector tube measurement system (Length-of-stain type) (in Japanese).

[8] Japan Association on Odor Environment, "Handbook of Offensive Odor Control Law (Six edition)," *Gyosei*, 2012 (in Japanese).
[9] Fujitsu Press Releases, "Fujitsu Successfully Develops a Breath Sensor Device That Quickly Measures Gas Components in People's Breath," https://www.fujitsu.com/global/about/resources/news/press-releases/2016/0418-01.html (Date of reference: 2025. 7.22).
[10] Tsuboi, O., Momose, S. and Takasu, R., "Mobile Sensor that Quickly and Selectively Measures Ammonia Gas Components in Breath," *FUJITSU*, Vol. 68, No. 1, pp. 59-64, 2017 (in Japanese).
[11] Kyotani, T., Kawasaki, T., Yoshie, S., Ushigome, M. and Tsuboi, O., "Application of a highly sensitive portable ammonia sensor for explore odor sources in public restrooms," *Indoor Environment*, Vol. 21, No. 3, pp. 189-197, 2018 (in Japanese). (DOI: https://doi.org/10.7879/siej.21.189)
[12] Kyotani, T., Kawasaki, T., Kameda, A. and Ueda, T., "Searching for Sources of Unpleasant Odors in Men's Restrooms in Railway Stations and Verifying the Effectiveness of Countermeasures to Reduce Them," *RTRI Report*, Vol. 39, No. 5, pp. 21-28, 2025.

Authors

Takashi KYOTANI
Senior Researcher, Comfort Science and Engineering Laboratory, Human Science Division
Research Areas: Analytical Chemistry, Biological Chemistry

Akiko KAMEDA
Assistant Center Chief, East Japan Railway Company
Tokyo Architecture Technology Center
Research Areas: Architectural Environmental Engineering

Tsuyoshi UEDA
Unit Head, Sensor Development Department, R&D Division, New Cosmos Electric co., ltd.
Research Areas: Gas sensors, Nanomaterials

Tamami KAWASAKI, Ph.D.
Senior Researcher, Comfort Science and Engineering Laboratory, Human Science Division
Research Areas: Environmental Biochemistry

Numerical Analysis of Contribution to Structure-borne Sound of Each Member in Reinforced Concrete Rigid-frame Viaducts

Tsutomu WATANABE
Track Dynamics Laboratory, Railway Dynamics Division

Toki UDA
Environmental Engineering Division

Mariko AKUTSU
Noise Analysis Laboratory, Environmental Engineering Division

Tamiko SEINO
AdvanceSoft Corporation

In this study, a numerical experiment was carried out using a finite element method to quantify the contribution to structure-borne sound of each member in a RC rigid-frame viaduct. As examples of specific results, the contribution to the overall value at the 25 m point on a reinforced concrete (RC) rigid-frame viaduct was 73% for the center slab, 10% for the soundproof wall, and 17% for the cantilever slab. In addition, the contribution of the RC rigid-frame viaduct and the adjustable RC girders were 67% and 33% respectively. This indicates that both the rigid-frame viaduct and the RC girder may contribute significantly to structure-borne sound along the railway line.

Key words**:** *structure-borne sound, structure member vibration, concrete, numerical analysis*

1. Introduction

Structure-borne sound is generated as a result of varying forces acting on structures. These forces are called "excitation forces" and are generated, for example, by trains running on roughness of rail surface and wheel tread of the order of several micrometers. These roughness are a permanent feature of wheel tread and rail surfaces. Excitation forces are also generated by track irregularity with a wavelength of the order of several meters in the direction of the track, which causes the wheels and rails to vibrate. These vibrations are transmitted to the track structure, which consists of sleepers and track slabs. They are also transmitted to civil structures that support the track, such as girder bridges, viaducts, and truss bridges. These structures radiate sound from their vibrating surfaces. Structure-borne sounds generated from reinforced concrete (hereafter called "RC") viaducts or other types of RC bridges mainly comprise frequency components between several tens of Hz and 1,000 Hz. For high-speed railway, the dominant zone in this frequency range lies in the range below 200 Hz [1, 2].

The RC rigid-frame viaduct that is the subject of this study is a Rahman structure, whose components, such as soundproof walls, slabs, beams, and columns, are rigidly connected. Previous research has revealed that the structure-borne sound of RC rigid-frame viaducts greatly contributes to noise along the railway line within the frequency bands where the natural vibration modes of each member of the viaduct predominate [3, 4]. On the other hand, the structure-borne sound of an RC rigid-frame viaduct is a composite sound of the sounds generated by its members. It is assumed that the components contributing most to the structure-borne sound vary depending on the frequency band. However, no previous studies have quantitatively examined how each member contributes to structure-borne sound in each frequency band.

In this study, we carried out numerical experiments using a numerical finite element method (hereafter called "FEM") simulation model to quantitatively clarify the contribution of each member to structure-borne sound in the frequency range up to 200 Hz. Note that RC rigid-frame viaducts often have RC adjustable girders made of reinforced concrete placed between them to counteract structural misalignment during earthquakes. Therefore, this study also included RC girders adjacent to RC rigid-frame viaducts in the numerical simulation model, considering them as subjects of the study.

2. Numerical analysis method

2.1 Outline of RC rigid-frame viaduct and RC girder

Figure 1 shows the outline of the structure to be analyzed. Table 1 shows the material properties for each element. We analyzed the Shinkansen standard 3-span RC rigid-frame viaduct with a block length of 25 m and RC girders of 10 m spans at each end. The column intervals on RC rigid-frame viaduct were 7.875 m for the side spans and 8.1 m for the middle span. The columns had a cross section of 1.1 m × 1.1 m and height of 10 m. The central spacing between the columns was 5.6 m; the thickness of the center slab, 0.28 m; the height of the soundproof wall, 2 m; the vertical beam cross section, 0.85 m × 1.4 m; the cross beam cross section, 0.85 m × 1.3 m; the height of the RC girder's main girder, 1.0 m; and the thickness of the slab, 0.25 m. The cross section of the roadbed concrete was 2.5 m × 0.25 m. This viaduct had pile foundations. The track was a standard slab track with JIS 60kg-Rail. The size of one-track slab was 4930 mm × 2340 mm × 190 mm, while the thickness of the cement asphalt (hereafter called a "CA") mortar was 25 mm.

RC rigid-frame viaducts support double tracks, while RC girders support single tracks, and are arranged in parallel. Furthermore, standard designs of structures are used for Shinkansen, and many structures with similar dimensions are constructed along the entire railway line [5]. By targeting this RC rigid-frame viaduct and RC

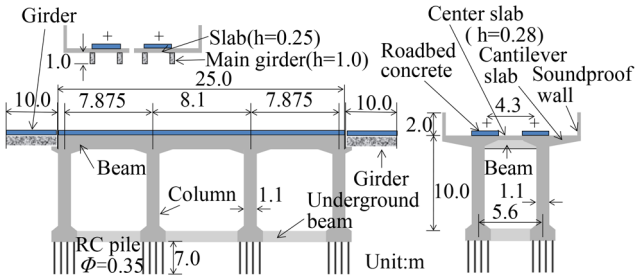

Fig. 1 Shinkansen standard 3-span RC rigid-frame viaduct and RC girders

Table 1 Material properties

		RC rigid-frame viaduct	RC girder
Rail		JIS 60kg-Rail	
Spring constant of railpad (MN/m)		60	
Track slab	Dimension (mm)	4930×2340×190	
	Young modulus (kN/mm^2)	31	
CA mortar	Young modulus (kN/mm^2)	3.5	
	Thickness (mm)	25	
Concrete	Young modulus (kN/mm^2)	26.5	24.0
Damping Constant (All modes)		2%	

girder, it is thus possible to evaluate most of the characteristics of structure-borne sound along Shinkansen lines.

2.2 Outline of numerical simulation model [3]

Figure 2 shows the outline of the numerical simulation model. In order to efficiently analyze structure-borne sound along railway lines up to 200 Hz, we developed a weak coupled structural-acoustic analysis model consisting of two vibration analyses and one acoustic analysis.

Specifically, the excitation force on the structure is calculated using a vibration analysis of vehicle/track. This excitation force is then used as input for a vibration analysis of the structure to calculate vibration of the structure. Furthermore, the vibration velocity of each FEM node obtained from the vibration analysis is used as a boundary condition in the acoustic analysis to determine structure-borne noise along the railway line.

The vibration analysis was conducted using DIASTARS [6], a program designed to analyze the dynamic interactions between vehicles and railway structures. In the vibration analysis of vehicle/track, the vehicle was assumed to be composed of a rigid body consisting of the car body, bogie, and wheelsets. These were connected by springs and dampers in a three-dimensional model, forming a multibody with 31 degrees of freedom per vehicle. The train was constructed by connecting the cars with springs and dampers at their ends. The vehicle specifications consisted of six standard Shinkansen cars, with a vehicle length of 25 m and a static wheel load of approximately 60 kN. The train speed was set to 270 km/h. In the track model, the rail and track slabs were modeled using beam elements, and the rail pads and CA mortar using spring elements. The dynamic interaction force between the vehicle and the rail is modeled as the vertical contact force using Hertz's contact spring. In the structure model, center slabs, cantilever slabs, vertical and cross beams, and soundproof walls were modeled using shell elements. The columns were modeled using beam elements. The damping constant in the vibration analysis of the structure was set to 2% [7]. The bottom ends of the columns were not modeled as ground springs and were to be completely fixed. Previous research had confirmed that, even if the bottom ends were completely fixed, the effect on the members of the superstructure was small [8].

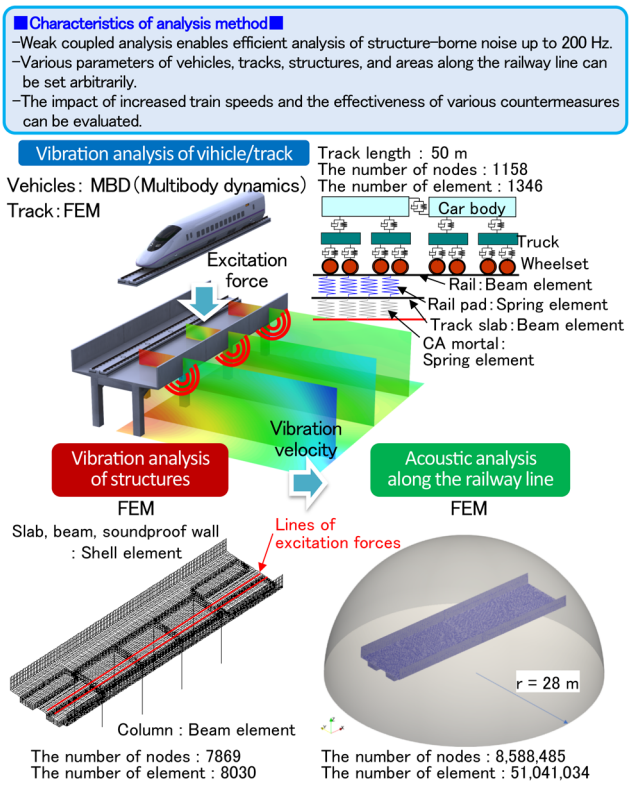

Fig. 2 Numerical simulation model

The acoustic analysis was conducted using Advance/FrontNoise [9]. Table 2 shows the analysis constants and boundary conditions in the acoustic analysis. The area of acoustic analysis was defined to include the RC rigid-frame viaduct, which has a block length of 25 m and RC girders with 10 m spans at each end. Specifically, a tetrahedral mesh with a one mesh size of 0.2 m and with 8,588,485 nodes and 51,041,034 elements was created in a hemispherical dome-shaped area with a radius of 28 m from the ground surface. This structure was then used as the internal boundary surface. The acceleration time history data of each node of the structure, calculated by vibration analysis, was converted into the frequency domain up to 200 Hz using Fourier transform. The result was then input into the internal interface as the sound source. The ground was defined as a perfect reflecting boundary, and the hemisphere was defined as an infinite boundary. Although the track is double tracks, the train runs on the side of the track indicated by the red line in the finite element model of "Vibration analysis of the structure" in Fig. 2.

Table 2 Analysis constants and boundary conditions in acoustic analysis

	Value		Boundary condition
Acoustic velocity (m/s)	340	Hemispherical dome-shaped area	Infinite boundary
Air density (kg/m^3)	1.225	Ground	Perfect reflection boundary
Analysis Frequency (Hz)	0.49~200 ($\Delta f \fallingdotseq 0.49$)	Viaduct	Area source of sound

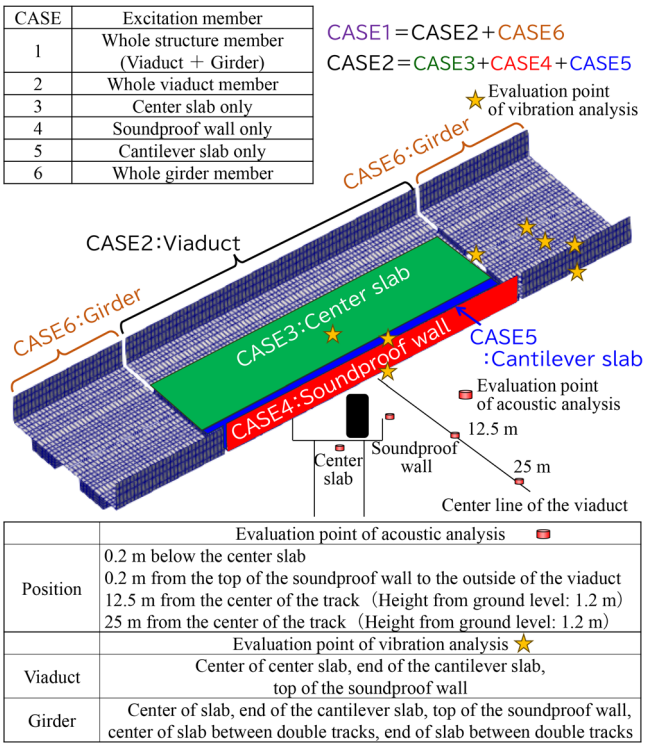

CASE	Excitation member
1	Whole structure member (Viaduct + Girder)
2	Whole viaduct member
3	Center slab only
4	Soundproof wall only
5	Cantilever slab only
6	Whole girder member

	Evaluation point of acoustic analysis
Position	0.2 m below the center slab 0.2 m from the top of the soundproof wall to the outside of the viaduct 12.5 m from the center of the track (Height from ground level: 1.2 m) 25 m from the center of the track (Height from ground level: 1.2 m)
	Evaluation point of vibration analysis
Viaduct	Center of center slab, end of the cantilever slab, top of the soundproof wall
Girder	Center of slab, end of the cantilever slab, top of the soundproof wall, center of slab between double tracks, end of slab between double tracks

Fig. 3 Analysis case and evaluation points

2.3 Analysis cases and evaluation point

Figure 3 shows the analysis cases. Six cases were set up to determine the contribution of each member to structure-borne sound along the railway line. Specifically, in CASE 1 the sound source is the whole structure member (RC rigid frame viaduct and the RC girder); in CASE 2 the sound source is the whole RC rigid-frame viaduct member; in CASE 3 the sound source is only the center slab of the RC rigid-frame viaduct; in CASE 4 the sound source is only the soundproof wall on the train running side; in CASE5 the sound source is only the cantilever slab on the train running side; and in CASE 6 the sound source is the whole RC girder member. The same vibration analysis results were used in all six cases. When setting the boundary conditions for each acoustic analysis in "acoustic analysis of railway line" shown in the bottom right of Fig. 2, only the target members were set as the sound sources. For example, in CASE 1, the boundary conditions were set so that all the members of the RC rigid-frame viaduct and RC girder structures in the acoustic analysis model were treated as sound sources. In CASE 3, the boundary conditions were set so that only the center slab of the RC rigid-frame viaduct was treated as the sound source.

As shown in Fig. 3, the evaluation points of acoustic analysis were set at:
- 0.2 m below the center of the center slab;
- 0.2 m from the top of the soundproof wall to the outside of the viaduct;
- 12.5 m from the center of the track on the train side (height from the ground level: 1.2 m);
- 25 m from the center of the track on the train side (height from the ground level: 1.2 m).

The 25 m point is the standard measurement point described in the Japanese Shinkansen Railway Noise Measurement and Evaluation Manual [10]. The height of 1.2 m above ground level is the height described in this manual as the height for microphone installation. All four points were set on the center line of the RC rigid-frame viaduct perpendicular to the track direction.

Furthermore, the focus of the vibration analysis was on representative members of each structure. Specifically, for RC rigid-frame viaducts, the evaluation points of vibration analysis were set at:
- the center of the center slab;
- the end of the cantilever slab;
- the top of the soundproof wall.

For RC girders, the evaluation points of vibration analysis were set at:
- the center of the slab;
- the end of the cantilever slab;
- the top of the soundproof wall;
- the center of the slab between double tracks
- the end of the slab between double tracks.

3. Analysis results

3.1 Vibration modes

Figure 4 and Fig. 5 show examples of vibration modes for the RC rigid-frame viaduct and the RC girder, respectively. Although there are many other vibration modes, only those corresponding to the peak frequencies of the sound pressure levels at each evaluation point of the acoustic analysis are extracted and shown as examples.

Figure 4 shows that, for the RC rigid frame viaduct, a vibration mode of the cantilever slab coupled with the soundproof wall perpendicular to the track direction appeared at 11.1 Hz. The primary vibration mode of the center slab appeared at 21.1 Hz. As the frequency increased to 32.2 Hz, 40.0 Hz, etc., the number of antinodes and nodes of the vibration mode increased. It was confirmed that each vibration mode was complexly coupled with each member. In addition to the examples shown here, many complex vibration modes appeared in the frequency band from 60 Hz to 100 Hz, in which members were connected.

Figure 5 showed that the primary bending vibration mode appeared at 11.8 Hz for the RC girder of train running side. At 83.8 Hz, the W-shaped vibration mode of the slab, which has three antinodes and four nodes, coupled with the vibration mode of the cantilever slab on the inter-track side. On the other hand, on the no train running side, the corresponding natural frequencies for the RC girder on the side not running trains were 10.5 Hz and 82.6 Hz, respectively. The difference in natural frequencies between the two girders is due to the cantilever lengths of their respective cantilever being different (1.0 m on the side where trains run and 0.5 m on the side

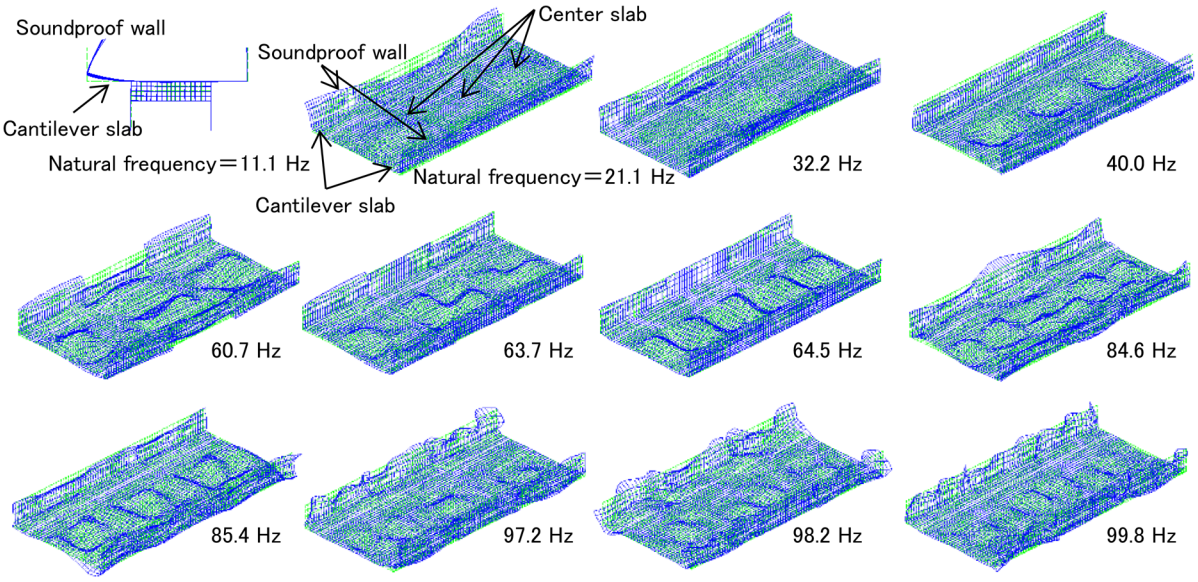

Fig. 4　Example of vibration modes for RC rigid-frame viaduct

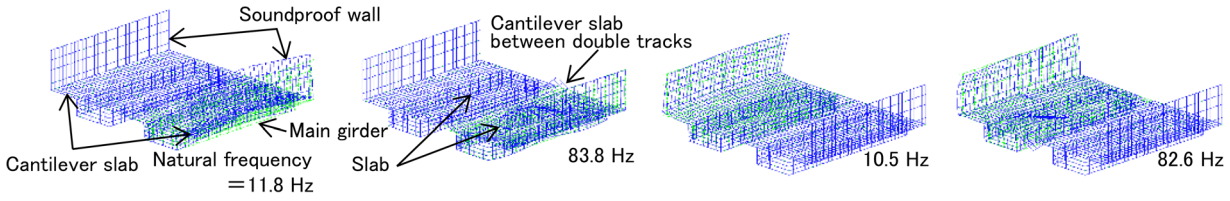

(a) Girder of train running side　　**(b) Girder of no train running side**

Fig. 5　Example of vibration modes for the RC girder

where trains do not run).

3.2 Vibration acceleration level at each evaluation point of vibration analysis

Figure 6 shows the vibration acceleration level at each evaluation point of vibration analysis. The vertical axes of the two figures show the same values. These were vibration acceleration levels at a single one representative point for each member. It should note that, in the frequency band below 12.5 Hz, the response of the slab, cantilever slab, soundproof wall, and center of slab between double tracks of the RC girder responded stronger than each member of the RC rigid-frame viaduct. Additionally, at frequencies of 20 Hz and 31.5 Hz, the response of the RC girder soundproof wall was higher than that of each member of the RC rigid-frame viaduct. Furthermore, even in the frequencies band higher than 63 Hz, the response of the slab, soundproof wall, the center of slab between double tracks and the end of slab between double tracks were higher than that of each member of the RC rigid-frame viaduct.

3.3 Sound pressure level at each evaluation point of acoustic analysis

3.3.1 Comparison of sound pressure levels for each analysis case of RC rigid-frame viaduct

Figure 7 shows a comparison of the sound pressure levels of the RC rigid-frame viaduct at each evaluation point of acoustic analysis for each 1/3 octave band frequency. It should be noted that the values on the vertical axis of the four figures are all the same. Figures 8 and 9 are similar to Fig. 7 with the same values on the vertical axis. In this paper, the evaluation focuses on low-frequency components that cause rattling in fittings. Therefore, the frequency weighting was set to Z (FLAT) when evaluating noise. Also, the overall value (hereafter called “O.A.”) represents the sum of the total power of all frequencies in the range up to 200 Hz.

The sound pressure levels of the case where the whole RC rigid-frame viaduct member was the sound source and the case where only the center slab was the sound source were compared at the evaluation point 0.2 m below the center of the center slab. As a result, the sound pressure of each case was almost the same. This result indicated that the contribution of the center slab was large. The contribution of the center slab was also large at the evaluation points 0.2 m from the top of the soundproof wall to the outside of the viaduct, the 12.5 m and 25 m from the center of the track.

Figure 8 shows an example of the sound pressure distribution around 63 Hz, which is the frequency band where peaks are observed in the sound pressure levels for each 1/3 octave band frequency at the 12.5 m and 25 m points shown in Fig. 7. The cross section shown in Fig. 8 is a cross section perpendicular to the track direction on the center line of the RC rigid-frame viaduct. The same color in the figure indicates the same sound pressure level in the figures shown below. As can be found in Fig. 8, the sound pressure distribution was almost identical for cases where either the whole viaduct member or only the center slab was the sound source. Therefore, the contribution of the center slab was significant. Additional-

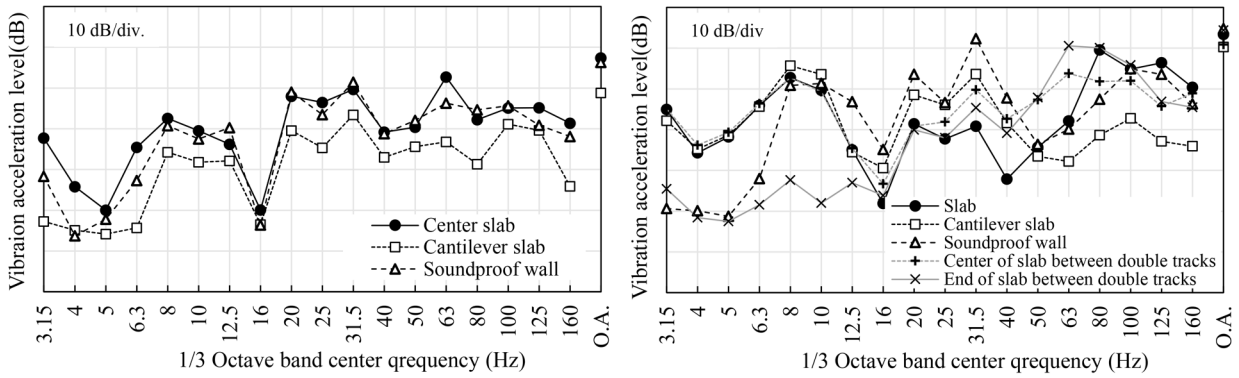

Fig. 6 Vibration acceleration level at each evaluation point of vibration analysis

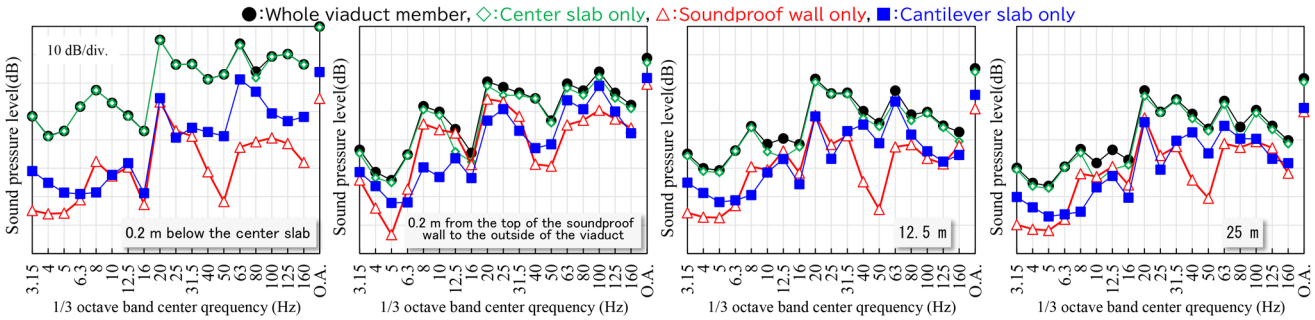

Fig. 7 Comparison of sound pressure levels of RC rigid-frame viaduct

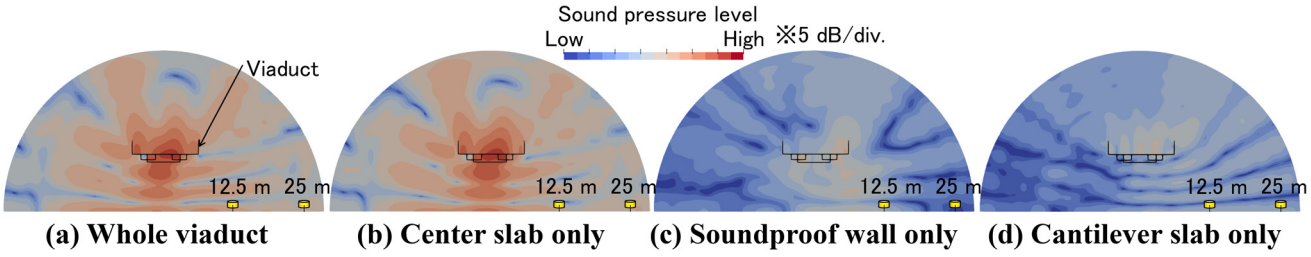

Fig. 8 Example of the sound pressure distribution around 63 Hz

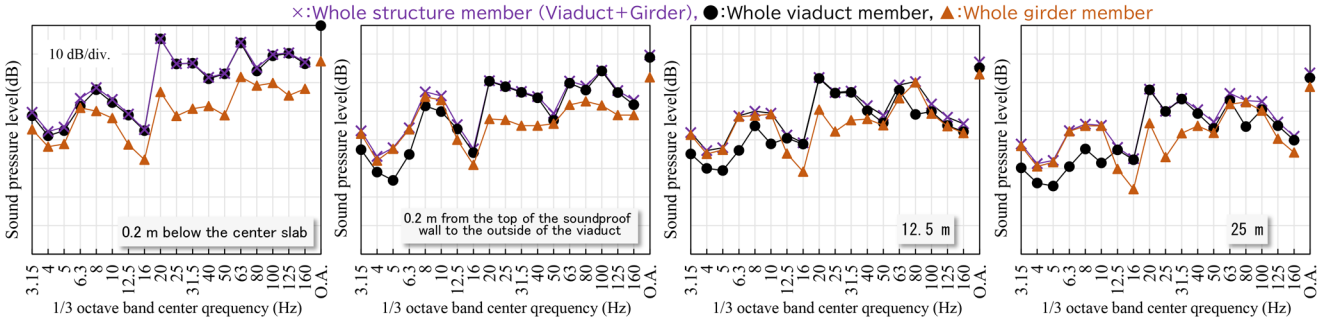

Fig. 9 Comparison of the sound pressure levels between RC rigid-frame viaduct and RC girder

ly, in cases where the sound source was either the soundproof wall or the cantilever slab, the sound pressure level was high in some places. However, this contribution was small compared to that of the center slab.

3.3.2 Comparison of sound pressure levels between RC rigid-frame viaduct and RC girder

Figure 9 shows a comparison of the sound pressure levels between the RC rigid-frame viaduct and the RC girder at each evaluation point of the acoustic analysis for each 1/3 octave band frequen-

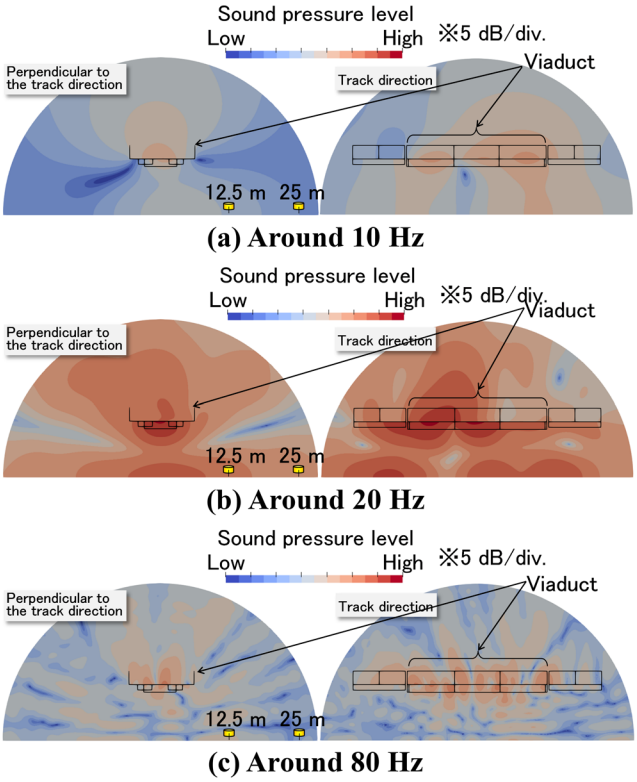

Fig. 10 Example of sound pressure distribution when whole viaduct member is sound source

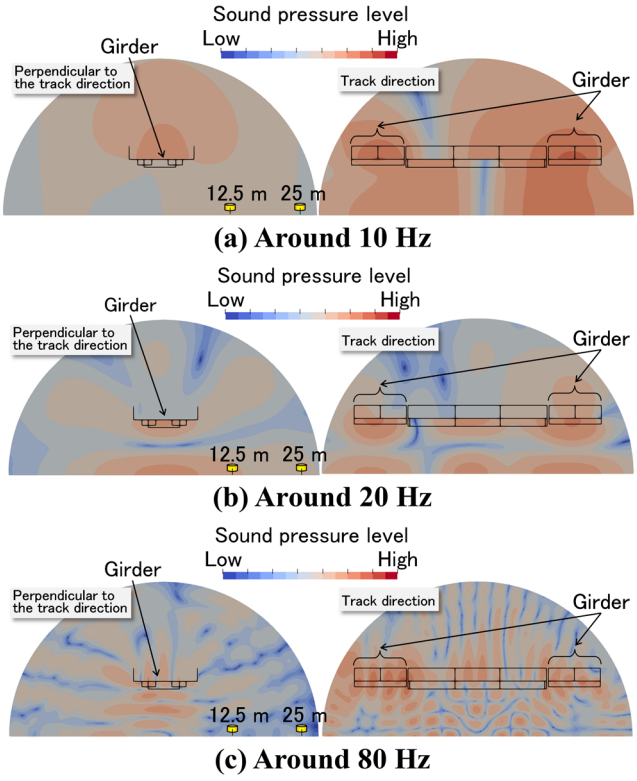

Fig. 11 Example of sound pressure distribution when whole girder member is sound source

cy. As can be seen in Fig. 9, the sound pressure level was higher when the whole girder member was the sound source than when the whole viaduct member was the sound source, especially at the 12.5 m and 25 m points, within the frequency range below 10 Hz and at 80 Hz. The evaluation position was the center line of the RC rigid-frame viaduct perpendicular to track direction. Nevertheless, it was found that there were frequency bands in which the RC girder adjacent to the RC rigid-frame viaduct made a larger contribution.

Figure 10 shows examples of sound pressure distribution around 10 Hz, 20 Hz, and 80 Hz from top to bottom for a case where the whole viaduct member is the sound source. In the same way, Fig. 11 shows sound pressure distribution around 10 Hz, 20 Hz, and 80 Hz for a case where the whole girder member is the sound source. Note that "around" refers to the analysis frequency closest to the relevant frequency. The primary bending vibration mode of the RC girder was around 10 Hz, and the primary vibration mode of the intermediate slab of the RC rigid-frame viaduct was around 20 Hz. The frequency band where peaks were seen in the RC girder at the 12.5 m and 25 m points shown in Fig. 9 was around 80 Hz. The cross section shown in Figs. 10 and 11 are two sections: a section perpendicular to the track direction on the center line of the RC rigid-frame viaduct, and a section in the track direction. As shown in Fig. 6, the vibration acceleration level of the RC girder was high at around 10 Hz. Consequently, the sound pressure level in the RC girder was higher than in the RC rigid-frame viaduct, with the sound pressure generated in the RC girder propagating to the RC rigid-frame viaduct. On the other hand, at around 20 Hz, due to the influence of the primary vibration mode of the center slab of the RC rigid-frame viaduct, the sound pressure level in the RC rigid-frame viaduct was higher than in the RC girder. It can also be seen that the sound pressure generated in the RC rigid frame viaduct propagated to the RC girder, no significant difference was observed in Figs. 10 and 11 in terms of the sound pressure levels generated near the RC rigid-frame viaduct and the RC girder at around 80 Hz . However, as with around 10 Hz vibration, the vibration acceleration level of the RC girder was higher. This was thought to be the reason why the sound pressure level was higher for the RC girder than for the RC rigid-frame viaduct. Additionally, the sound generated from the RC girder attenuated less over distance, with the sound pressure level propagating without attenuation up to the center line of the RC rigid-frame viaduct. This is presumably because the cross section perpendicular to track direction focused on Figs. 10 and 11 was the center of the analysis model. Therefore, the vibration mode of the center slab in the RC rigid-frame viaduct was close to the node of the mode shape. However, in the RC girder, as shown in Fig. 5, the vibration mode of the cantilever slab between the double tracks corresponds to the antinode of the mode shape, therefore, the sound pressure from the RC girder propagated further.

3.4 Contribution of each member to structure-borne sound along the railway line

Figure 12 shows the contribution of each member to structure-borne sound along the railway line. Figure 12(a) shows the comparison of contribution of each member to structure-borne sound about the RC rigid-frame viaduct. The contribution of the center slab was significant at all evaluation points. Conversely, at the evaluation points 0.2 m from the top of the soundproof wall to the outside of the viaduct, the 12.5 m and 25 m from the center of the track, the contribution of the soundproof wall and the cantilever slab exceeded that of the center slab at frequencies of 12.5 Hz, 63 Hz, and 80 Hz. It was thought that this was due to the presence of two vibration modes: one at 11.1 Hz, in which the cantilever slab perpendicular to track direction and coupled with the soundproof

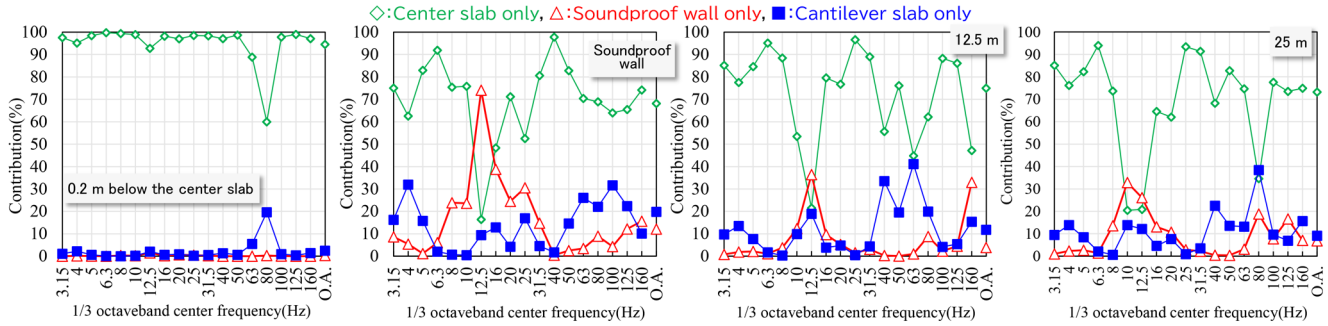

(a) Comparison of contribution to structure-borne sound about each member of RC rigid-frame viaduct

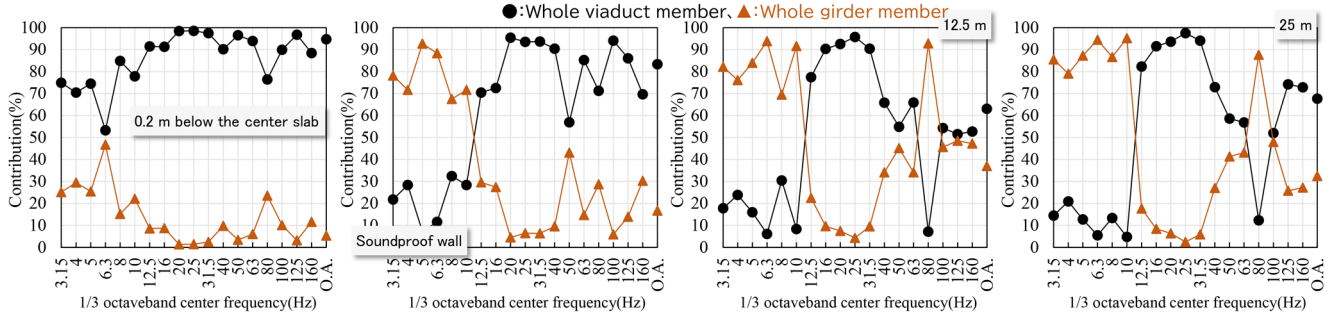

(b) Comparison of contribution to structure-borne sound between RC rigid-frame viaduct and RC girder

Fig. 12 Contribution of each member to structure-borne sound along railway line at each evaluation point

wall; two at 60.7 Hz and 84.6 Hz, in which antinodes and nodes can be identified in the cantilever slab and the center slab. In this way, it was made clear that the center slab, which was a plate-like component, was thought to have a significant influence on structure-borne sound along RC rigid-frame viaducts. On the other hand, there were also cases in which members other than the center slab had a higher sound pressure level depending on the frequency band.

Figure 12(b) shows the comparison of contribution to structure-borne sound between the RC rigid-frame viaduct and the RC girder. As shown in Fig. 5, at 12.5 m and 25 m from the center of the track, the RC girder had a larger contribution than the RC rigid-frame viaduct, especially in the frequency range below 10 Hz and at 80 Hz. It was thought that this was because the vibration acceleration level of the RC girder was higher than that of the RC rigid-frame viaduct within the relevant frequency band, as shown in Fig. 6. Additionally, the existence of the primary bending mode of the RC girder at 11.8 Hz and the vibration mode coupled between the slab and the cantilever slab between double tracks at 83.8 Hz, shown in Fig. 5, was also thought to be an influence.

Figure 13 shows the contribution to O.A. of sound pressure level at 25 m from the center of the track. The contribution to the O.A. at 25 m from the center of the track on the RC rigid-frame viaduct was 73% for the center slab, 10% for the soundproof wall, and 17% for the cantilever slab. Additionally, the contribution of the RC rigid-frame viaduct and the adjustable RC girders were 67% and 33% respectively. This indicates that not only the RC rigid-frame viaduct but also the RC girder may have a relatively significant contribution to structure-borne sound along the railway line.

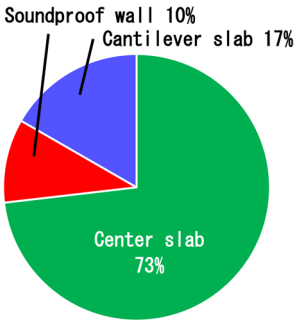

(a) Comparison between each member of RC rigid-frame viaduct

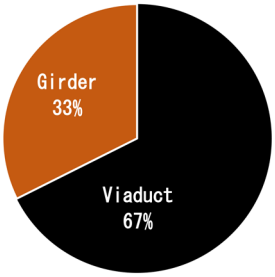

(b) Comparison between RC rigid-frame viaduct and RC girder

Fig. 13 Contribution to O.A. of sound pressure level at 25 m from center of track

4. Conclusions

In this study, we carried out numerical experiments using a numerical simulation model based on the FEM to quantify the contribution of each member of a RC rigid-frame viaduct and RC girder to structure-borne sound within the frequency range up to 200 Hz. Specifically, the contribution to the O.A. at 25 m from the center of the track on the RC rigid-frame viaduct was 73% for the center slab, 10% for the soundproof wall, and 17% for the cantilever slab. In addition, the RC rigid-frame viaduct and the adjustable RC girders contributed 67% and 33% respectively. This indicates that both the

RC rigid-frame viaduct and the RC girder may contribute significantly to structure-borne sound along the railway line. In the future, we plan to conduct a detailed analysis of the vibration mode of the RC girder, since it has been newly revealed that it makes a significant contribution to structure-borne sound along the railway line.

References

[1] Nagakura, K., "Problem of Shinkansen Super-express Railway Noise," *Acoustical Science and Technology*, Vol. 60, No. 5, pp. 284-289, 2004 (in Japanese).
[2] Kitagawa, T., "Noise and vibrati on control of railway vehicle," *Acoustical Science and Technology*, Vol. 64, No. 12, pp. 629-634, 2008 (in Japanese).
[3] Watanabe, T., "Numerical Simulation based Evaluation Method of Structure-borne Noise of Reinforced Concrete Viaduct," *Quarterly Report of RTRI*, Vol. 62, No. 2, pp. 130-136, 2021.
[4] Watanabe, T., Sogabe, M., Tokunaga, M., "Analytical Study on Structure Member Vibration Characteristics of Reinforced Concrete Viaducts," *Journal of Advanced Simulation in Science and Engineering*, Vol. 2, No. 1, pp. 16-33, 2015.
[5] Japan National Railways, *Tohoku Shinkansen Construction Report, Omiya-Morioka section*, 1983 (in Japanese).
[6] Wakui, H., Matsumoto, N., Tanabe, M., "A Study on Dynamic Interaction Analysis for Railway Vehicle and Structures," *QR of RTRI*, Vol. 35, No. 2, pp. 96-104, 1994.
[7] Railway technical institute, *Design Standards for Railway Structures and Commentary (Concrete Structures)*, 2007.
[8] Watanabe, T., Matsuoka, K., Fuchigami, S., "Mechanism and Reduction Countermeasure of Structure Borne Sound of Reinforced Concrete Viaducts," *Noise and Vibration Mitigation for Rail Transportation Systems*, Vol. 139, pp. 659-670, 2018.
[9] Matsubara, K., Ogawa, S., Infinite Element scheme in Advance/FrontNoise," *Advance simulation*, Vol. 23, 2016 (in Japanese).
[10] Ministry of the Environment, *Shinkansen Railway Noise Measurement and Evaluation Manual*, 2015 (in Japanese).

Authors

Tsutomu WATANABE, Dr.Eng.
Senior Chief Researcher, Head of Track Dynamics Laboratory, Railway Dynamics Division
Research Areas: Concrete Sleeper, Numerical Simulation, Structure-borne Sound, Vibration

Toki UDA, Ph.D.
Director, Head of Environmental Engineering Division
Research Areas: Railway Noise

Mariko AKUTSU, Ph.D.
Senior Researcher, Noise Analysis Laboratory, Environmental Engineering Division
Research Areas: Railway Noise

Tamiko SEINO
Main Researcher, AdvanceSoft Corporation
Research Areas: Computational Mechanics

Numerical Analysis Methods for Predicting the Impact on Existing Tunnels during Closely-spaced Tunnel Intersection Construction

Takashi NAKAYAMA **Akihiko MIWA** **Tatsuki SHIMIZU**
Tunnel Engineering Laboratory, Structures Technology Division

This paper proposes a new numerical analysis method for neighboring construction where a new shield tunnel is excavated close beneath an existing tunnel. These tunnels are mathematically modeled using detail 3D shell elements and the ground between the tunnels is modeled using interaction springs. The strength of the interaction springs is determined using stability calculations of the ground above the new shield tunnel. We conducted a trapdoor test that reproduces this neighboring construction and measured the interaction between the intersecting tunnels. The results confirmed that the proposed analysis method can simulate the test result of ground reaction forces and tunnel deformation.

***Key words*:** *tunnel, adjacent construction, trap door test, numerical analysis*

1. Introduction

In recent years, there has been an increasing trend towards the underground construction of infrastructure such as railways, roads, and water and sewage systems. Cases such as the example shown in Fig.1 where tunnels cross below ground are increasingly common. Excavating a new tunnel beneath an existing one whilst keeping it in service requires precise prediction of the displacement and stress increases which will affect the existing tunnel. Tunnel intersection projects are just one example of construction activities that may affect existing structures through the surrounding ground. These constructions are collectively referred to as "neighboring construction."

This term is typically used when the horizontal distance between the new and existing structures is less than two to three times the width of the new structure[1, 2]. The Manual for Assessment and Planning in Neighboring Construction of Urban Railway Structures [1] provides classification diagrams, such as the one shown in Fig. 2. The figure defines, neighboring construction as cases where the new structure overlaps with either the "Caution Zone" or the "Restricted Zone." In such cases, it is necessary to conduct impact assessments and consider whether reinforcement measures are needed. The manual also includes numerical analysis methods for evaluating the effects of construction and showcases examples of effective mitigation strategies.

However, as underground spaces become increasingly congested, the distance between structures tends to decrease. Therefore, it is necessary to improve conventional numerical analysis methods. The construction of tunnel intersections is often classified as being in the Restricted Zone, requiring detailed impact assessments. When the distance between tunnels is less than the outer diameter of the new tunnel, conventional numerical analysis methods alone are insufficient. In other words, ground improvement must be implemented regardless of the ground conditions. To develop more suitable countermeasures based on the ground conditions at the target site, it is necessary to enhance conventional numerical analysis methods.

This study proposes a new numerical analysis method for predicting the impact of construction on existing tunnels during closely spaced tunnel intersection construction. In this paper, the term "ultra-close tunneling" is defined as tunnel construction with extremely small clearances between new and existing tunnels, where conventional evaluation methods may be insufficient. The validity of the proposed method was verified through trap door test simulating ultra-close tunnel conditions. This paper presents the details of the proposed method and reports the results of a trial analysis conducted under assumed full-scale construction conditions. Additionally, this paper reports the evaluated potential impact on existing tunnels.

2. Numerical analysis method for predicting the impact on existing tunnels during tunnel intersection construction

2.1 Conventional methods

(1) Overview

The conventional numerical analysis method used in tunnel

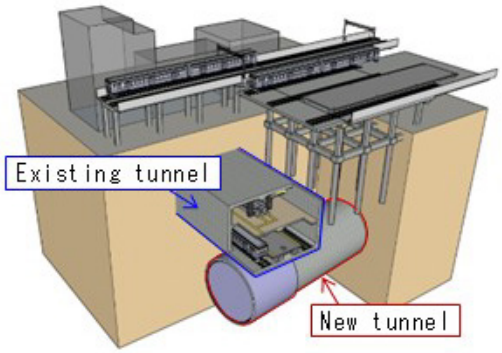

Fig. 1 Tunnel intersection project

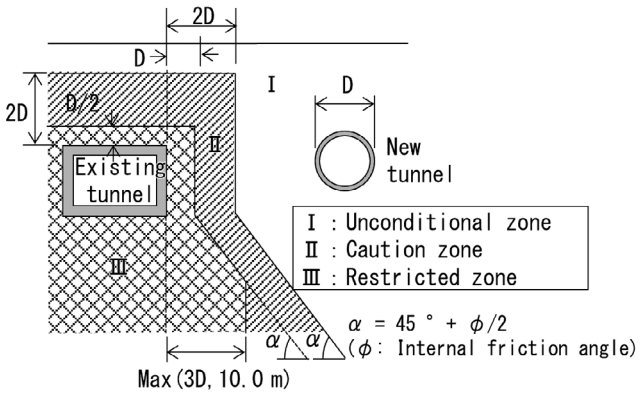

Fig. 2 Example of classification diagram

construction is based on the assumption that during excavation of a new tunnel, the surrounding ground behaves as a continuous medium and that the existing tunnel deforms as part of this medium. Figure 3 illustrates the flow of the analysis. First, the cross-section of the new tunnel is modeled using plane strain elements to represent the surrounding ground. Excavation is simulated by applying equivalent loads to the outer perimeter of the new tunnel. This simulation yields the ground displacement at the location of the existing tunnel axis (Fig. 3, STEP 1). Next, the existing tunnel is modeled as a beam on an elastic foundation. The ground displacements obtained in STEP 1 are applied to the spring supports of the beam model. As a result of this calculation, the displacement and stress increments necessary for evaluating the impact on the existing tunnel are obtained. (Fig. 3, STEP 2).

(2) Issues in ultra-close construction

During ultra-close tunnel construction, a "loosened zone" tends to form in the soil above the new tunnel due to excavation [3]. This zone, characterized by reduced confining pressure and loss of continuity with the surrounding ground, significantly affects the stiffness of the soil, especially in soft ground conditions. Figure 4(a) shows an example of the loosened zone. The zone is bounded laterally by straight lines inclined at an angle of $45° + \phi/2$ (where φ is internal friction angle) and forms an arch shape above the tunnel.

The width b of the loosened zone depends on the internal friction angle. For example, when $\phi = 30°$, the width is approximately 1.58 times the outer diameter D of the new tunnel. The smaller the friction angle, the wider the width of loosened zone. The height h of the zone generally ranges from approximately the same as the tunnel diameter D to twice the diameter, depending on the construction conditions [4, 5]. In ultra-close construction, thorough consideration of the loosened zone is crucial. This is particularly important in soft ground conditions, as reduced confining pressure significantly decreases ground stiffness, intensifying the impact of the loosened zone. Conventional methods assume that the existing tunnels deform in response to ground movement. However, as Fig. 4(b) shows there is also a risk of reduced ground reaction forces near the loosened zone. This could disrupt the load balance, and result in settlement or subsidence of the tunnel. Despite these risks, the extent to which the loosened zone has become less stiff has not yet been quantitatively clarified. It should be noted that, as a precaution, ground improvement measures have traditionally been applied to stabilize the loosened zone, regardless of the actual ground conditions, to prevent settlement.

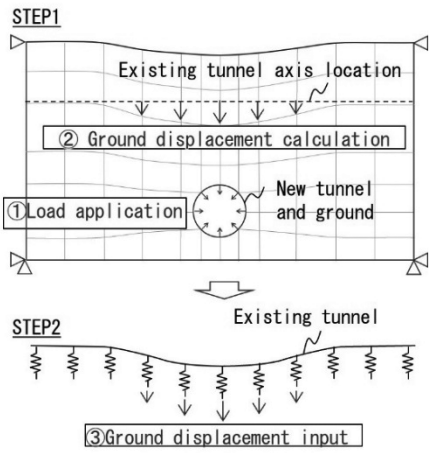

Fig. 3 Conventional calculation flow

2.2 Proposed methods

(1) Overview

Figure 5 illustrates the proposed numerical analysis method for intersection tunnel construction. This method can reproduce the settlement behavior observed in ultra-close construction. This method uses special springs, called 'interaction springs,' placed under the existing tunnel to reproduce the behavior of the loosened area. These interaction springs are made stiffer by applying a reduction factor to the original ground spring values. This reduction factor is based on the ratio of ultimate bearing capacity beneath the existing tunnel before and after the new tunnel is excavated (details are provided in reference [2]). All other design parameters follow the "Design Standards for Railway Structures (Cut-and-Cover Tunnels)" [6]). The effects of ground improvement can be included by adjusting the design ground parameters used in these calculations. Furthermore, in ultra-close construction, the size of the existing tunnel may be large compared to the separation distance. This makes it unclear whether the beam-on-elastic-foundation model remains valid. To address this issue, the existing tunnel has been modeled using a full three-dimensional geometry which reflects its actual shape.

(2) Method for calculating the reduction factor of interaction springs

To determine the reduction factor for the interaction spring stiffness, we followed a conventional approach from the 'Design Standards and Commentary for Railway Structures (Foundation Structures)' [7]. This method is widely used in practical design to

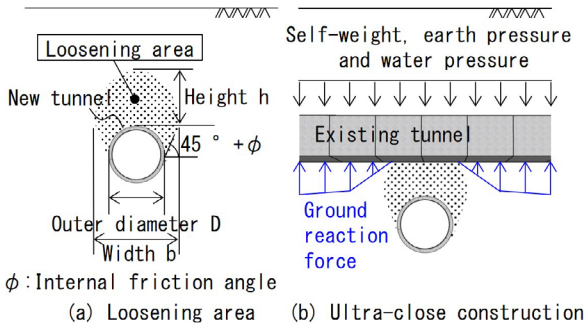

Fig. 4 Relationship between loosening area and ultra-close construction

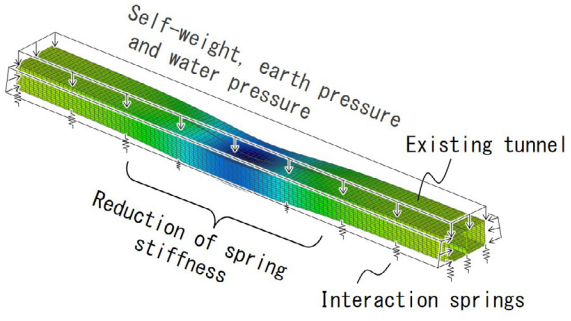

Interaction spring stiffness
= reduction ratio ×
original ground spring stiffness
Reduction ratio
= ratio of ultimate bearing capacity before and after excavation of the new tunnel

Fig. 5 Proposed method

calculate the ground spring values beneath foundation structures located near slopes. It involves calculating the ultimate bearing capacity [8] of foundations on flat ground and near slopes, and using the ratio to reduce the spring stiffness beneath foundations adjacent to slopes. We developed a method to simplify the calculation of ultimate bearing capacity. This introduces a virtual ground surface beneath the existing tunnel, enabling straightforward application of Terzaghi's bearing capacity formula (Equation 1), as illustrated in Fig. 6.

$$q = c\,N_c + \frac{\gamma^B}{2} N_r \qquad (1)$$

Where: q: ultimate bearing capacity, c: soil cohesion, γ: unit weight of the soil, B: foundation width, N_c, N_r: bearing capacity factors

When calculating the ultimate bearing capacity (q_1) before the new tunnel is excavated, we assumed a virtual ground surface (cd) and a slip surface (ab), as shown in Fig. 6(a), while ignoring the soil resistance above the existing tunnel. The bearing capacity factors used in Eq. (1) are in general those applied to surface foundations [7].

For the post-excavation bearing capacity q_2, we assumed a virtual ground surface (dec) and a slip surface extending toward (de), excluding the loosened zone, as illustrated in Fig.6(b). This value was calculated based on methods reported on the reference (8). By calculating q_1 and q_2 for various horizontal distances, we used the bearing capacity ratio q_2/q_1 as the reduction factor for each corresponding distance. Moreover, near the virtual surface (de), the post-excavation bearing capacity (q_2) can be extremely low, potentially lower than the applied load. In such cases, the reduction factor is set to zero.

3. Validation of the proposed method through soil tank experiments

3.1 Overview

We conducted soil tank experiments simulating ultra-close construction and performed simulation analyses based on the proposed method to verify its validity. Figure 7 shows the trap door test apparatus used in this study. The trap door test is a well-established method that has previously been used to develop earth pressure formulas for tunnel design [3, 9]. In this test, dry sand or aluminum rods are packed into a soil tank of the apparatus. A portion of the tank's bottom plate (the drop-bottom) is then lowered to simulate tunnel excavation. As illustrated in Fig. 8, we placed a model of the new tunnel on top of the drop-bottom and placed a model of the existing tunnel intersecting it within the soil. In the same manner reported in previous studies [3, 9], the new tunnel model was lowered by 1 mm to replicate excavation conditions. It should be noted that the behavior of the excavation boundary differs between actual tunnel excavation and the drop-bottom experiment, as shown in Fig. 8(c). In the trap door test, lateral loosening around the tunnel does not occur. As a result, the loosened zone width (b) tends to be narrower, being approximately equal to the outer diameter of the new tunnel. This has been identified as a limitation of this experimental method. A detailed discussion of how this issue is addressed is provided at the end of this section.

3.2 Experimental conditions and methodology

Based on the previous tunnel intersection projects included in Reference 1, where the new tunnel is typically constructed using tunnel boring machines and the existing tunnel is built by cut-and-cover methods, we modeled the new tunnel with a semicircular cross-section and the existing tunnel with a rectangular one. The material and dimensions of the existing tunnel model were set such that the stiffness ratio between the model and the ground is equivalent to that of a standard railway cut-and-cover tunnel (single layer, double span) existing within ground with an N-value of 25. Furthermore, the setup also ensured that strain variations could be accurately measured. The tunnel model was made from acrylic. The external

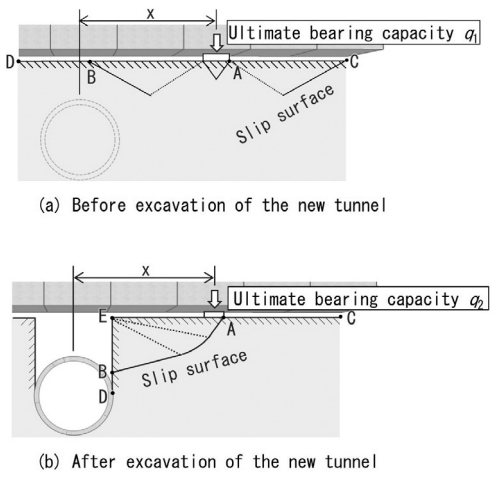

Fig. 6 Assumption for calculating ultimate bearing capacity below the existing tunnel

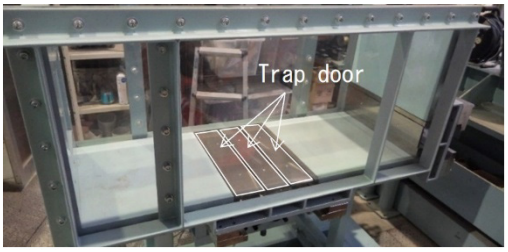

Fig. 7 Trap door test apparatus

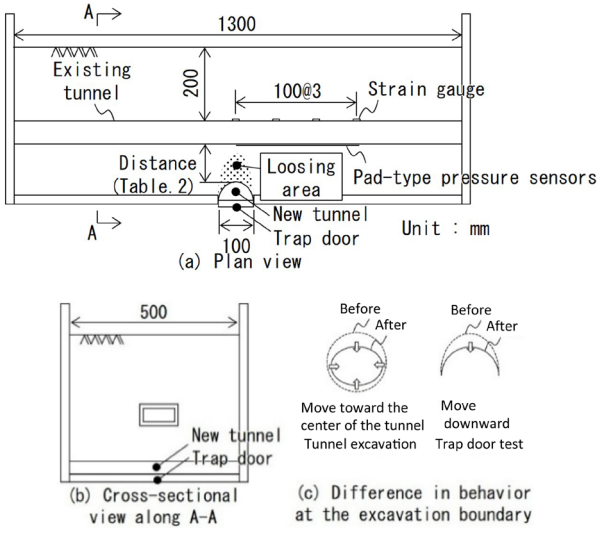

Fig. 8 Trap door test in this study

dimensions of the tunnel cross-section were set uniformly to 90 mm in height, 150 mm in width, and 10 mm in wall thickness. Dry silica sand No. 7, with the physical properties listed in Table 1, was used for the ground. It was compacted to achieve a target relative density of 70%. As shown in Table 2, the separation distances between two tunnels in the test cases were 100 mm and 200 mm. The separation distance of 100 mm corresponds to the ultra-close construction. Pad-type pressure sensors [10] were installed close intervals beneath the existing tunnel model to measure ground reaction forces. As shown in Fig. 9, strain gauges were also placed on the top surface in order to monitor deformation behavior.

3.3 Experimental results and validation of the proposed method

(1) Changes in ground reaction forces beneath the existing tunnel model

Figure 10 shows the relationship between the horizontal distance from the center of the new tunnel model and the measured distribution of ground reaction forces beneath the existing tunnel model. The distribution of ground reaction forces is expressed as a ratio of the forces before and after the new tunnel model is dropped. The solid and dashed lines indicate the moving averages of the measured ground reaction forces over a 30 mm interval. In both cases, the ground reaction force ratio gradually decreases as the center of the new tunnel model is approached. However, the rate and pattern of the decrease differ in the two cases. In the case of 100 mm separation, the ratio drops sharply from around 200 mm and approaches nearly zero within the 0-50 mm range. On the other hand, the case of 200 mm separation, the ground reaction forces decrease at generally constant gradient. In the ultra-close tunneling construction, when the reduction in ground stiffness varies significantly between inside and outside of the loosened zone, the ground reaction beneath the existing tunnel tends to drop sharply near the loosened area, as shown in Fig. 4(b). This distinctive reaction pattern was confirmed in the soil tank experiment, but it was observed only under ultra-close tunneling conditions with a separation of 100 mm.

(2) Verification of the method for calculating interaction spring values

Using the proposed method described in Section 2.2, specifically the procedure for calculating interaction spring values, the simulation analysis was conducted to evaluate tunnel–ground interaction. As shown in Fig. 11, the position of the virtual ground surface (de) in Fig. 6(b) was set in two ways for the calculation: at the center of the new tunnel (Condition A) and at its side (Condition B). Figure 12 compares the results for the 100 mm separation case, which corresponds to extremely close tunneling. Both calculation results show a similar gradient to the experimental data, but the results from Condition A are closer to the actual measurements. Figure 13 presents the results for the 200 mm separation case. In this case, regardless of the position of the virtual ground surface (de), the

Table 1 Physical properties of silica sand No. 7

Maximum dry density ρ_{dmax} (kN/m^3)		15.6
Minimum dry density ρ_{dmin} (kN/cm^3)		12.2
Triaxial test (CD)	Cohesion c (kN/m^2)	5.8
	Internal friction angle ϕ (deg)	42.4
	Deformation modulus E_{50} (MN/m^2)	33.3 (σ_3 = 25 kN/m^2) 33.4 (σ_3 = 50 kN/m^2) 57.1 (σ_3 = 75 kN/m^2)

Table 2 Case

Case	Distance (mm)
1	100
2	200

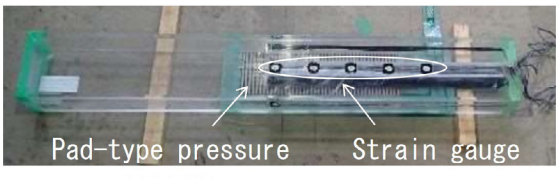

Fig. 9 Existing tunnel

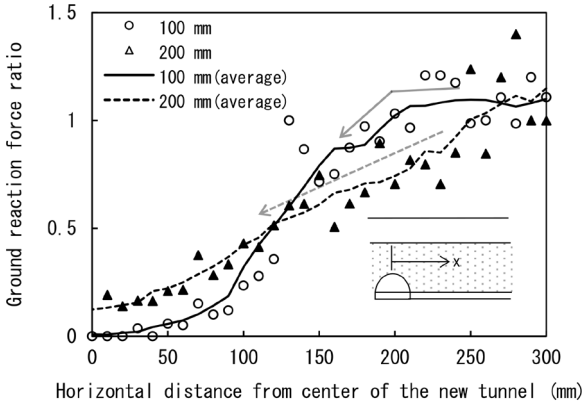

Fig. 10 Distribution of ground reaction force ratio under tunnel model

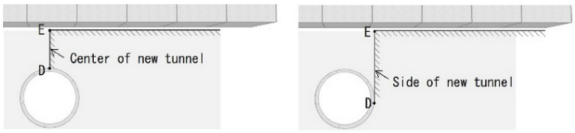

(a) Condition A (b) Condition B

Fig. 11 Setting position of the virtual ground surface (de)

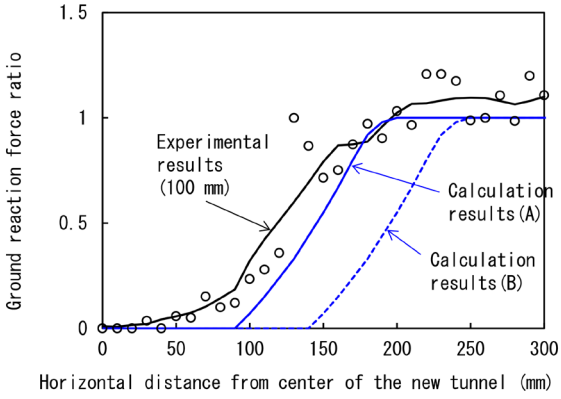

Fig. 12 Comparison between experimental results and calculated results (at a separation distance of 100 m)

calculated results deviate from the experimental data, indicating that the accuracy of the method decreases when the tunneling distance is not extremely close.

(3) Simulation analysis of the existing tunnel model

Using the proposed method described in Section 2.2, the strain distribution on the top surface of the existing tunnel model was calculated. The tunnel model was represented by using solid elements in the finite element method, with interaction springs incorporated. Loads including self-weight, vertical earth pressure, and horizontal earth pressure were applied to the existing tunnel model. Based on the findings in section (2), the analysis focused on the case with a separation of 100 mm. Figure 14(a) shows an example of the simulation results, presenting the deformation and stress contour when the virtual ground surface (de) is set to position A. From this figure, it can be seen that there is notable settlement along the tunnel axis in the central part of the tunnel. Figure 14(b) shows a comparison of the calculated and test results for axial strain on the top surface of the existing tunnel model. Although some deviation is observed at the horizontal position of 100 mm, which is similar to the ground reaction distribution, it is understood that the results from Setting A more accurately reflect the experimental behavior.

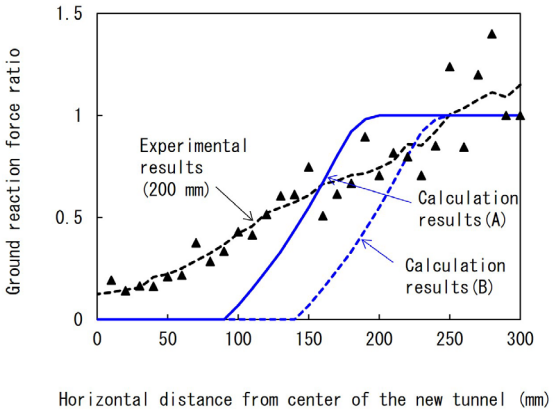

Fig. 13 Comparison between experimental results and calculated results (at a separation distance of 200 m)

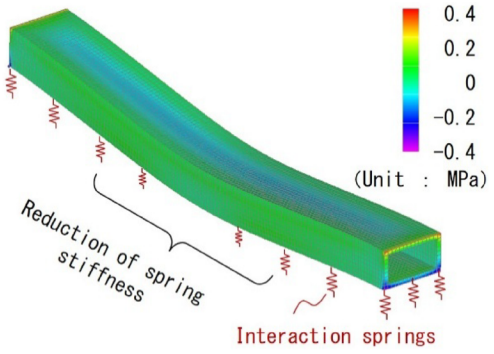

(a) Deformation and stress contour diagram (condition A)

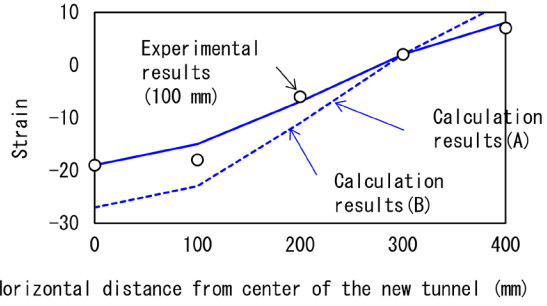

(b) Comparison of longitudinal strain distribution

Fig. 14 Simulation analysis results using the proposed method I

3.4 Summary

In the experiment, a ground reaction distribution influenced by the loosened zone was observed in the ultra-close tunneling case with a separation of 100 mm. Using the proposed method, a simulation analysis was conducted for this experiment. The results confirmed that when the virtual ground surface (de) in Fig. 6(b) was set at the center of the new tunnel model, the behavior beneath the existing tunnel model could be reasonably well reproduced. However, the width (b) of the loosened zone differs between the trap door test and actual tunnel excavation. Therefore, when applying the proposed method to field conditions, it is necessary to adjust the position of the virtual ground surface (de) to account for this difference. As shown in Fig. 4 (a), the width (b) of the loosened zone in actual tunnel excavation is determined by the internal friction angle φ. If we assume $\phi = 0°$, the width of the loosened zone reaches its maximum, which is twice the width observed in the trap door test. In this case, the position of the virtual ground surface (de) should be shifted from the center of the new tunnel to its side by D/2, as shown in Fig. 11(b). The position of the virtual ground surface (de) is expected to lie somewhere between the center and the side of the new tunnel. In practice, this adjustment can be determined using the internal friction angle φ obtained from field investigations.

4. Trial calculations using conventional method and proposed method

4.1 Overview

Based on assumed construction conditions, trial calculations were performed using both the conventional method and the proposed method, respectively. Figure 15 shows the tunnel intersection conditions assumed for the analysis. The ground is modeled as homogeneous cohesive soil (equivalent to an N-value of 30), and the construction conditions involve a new shield tunnel (single-track) crossing perpendicularly beneath an existing cut-and-cover tunnel (two-span, single-layer).

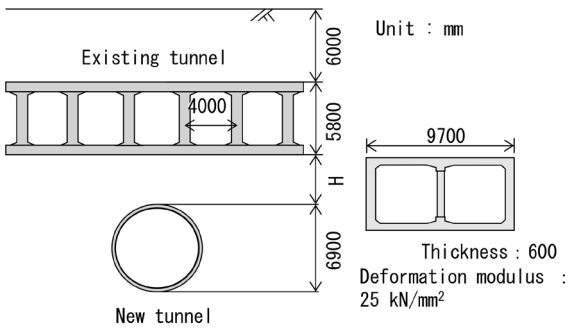

Fig. 15 Tunnel specifications

4.2 Trial calculations using the conventional method

Trial calculations were carried out based on “Manual for Assessment and Planning in Neighboring Construction of Urban Railway Structures” [1]. The ground deformation modulus E was estimated as equivalent to 2500 N (where N is the standard penetration test value). The area to be analyzed is determined as follows: on the sides, it extends to a distance five times the depth between the tunnel crown and the bottom of the neighboring tunnel, below the new tunnel, it stretches to twice the diameter of the excavation. This is illustrated in Fig. 16. Two cases were considered regarding tunnel separation, as shown in Table 3. In this context, the case with a separation of 3.5 m corresponds to ultra-close construction. An initial stress analysis was performed, and equivalent nodal forces were then applied to the area of the new tunnel to simulate ground deformation. The equivalent nodal forces are calculated by multiplying the pre-excavation in-soil stresses prior to excavation by a factor known as the stress release ratio. In general, the stress release ratio ranges from 8-15% in Pleistocene deposits and 15-30% in alluvial deposits. For this trial calculation, a value of 15%, representing the boundary between these two layers, was chosen. Figure 17 shows the absolute displacement beneath the existing tunnel. A comparison of the analysis results for the 3.5 m and 14 m separation cases shows that the smaller separation of 3.5 m results in a greater maximum settlement and a steeper displacement gradient.

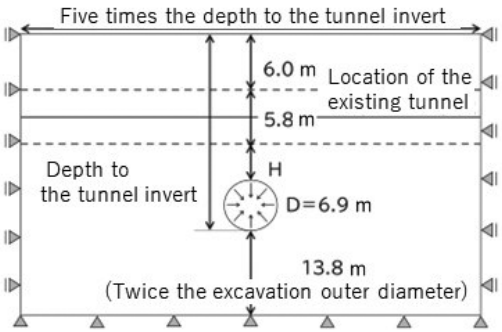

Fig. 16 Comparison between experimental results and calculated results (at a separation distance of 200 m)

Table 3 Case

Case	Distance
1	3.5 m
2	14 m

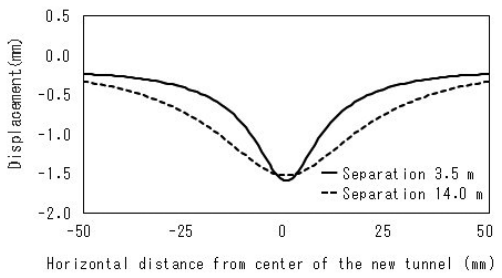

Fig. 17 Absolute displacement beneath the existing tunnel (conventional method)

4.3 Trial calculations using the proposed method

The floor slab, side walls, and longitudinal beams of the existing tunnel were modeled using shell elements, and the central columns were represented with beam elements. To ensure that boundary effects would not influence the analysis results, the length of the tunnel along the axis was set to 100 meters. The applied loads included self-weight, vertical earth pressure, and horizontal earth pressure. Since the proposed method was found to diverge from actual behavior in cases other than ultra-close tunneling, as confirmed by the trap door test, the analysis was conducted only for the separation of 3.5 m. Two simulations were conducted to evaluate the displacement increment caused by ultra-close separation. One simulation uses ground springs to represent the original ground conditions beneath the existing tunnel. Another uses interaction springs. Figure 18 shows the deformation and displacement contours of the existing tunnel. As can be seen in Fig.18, the tunnel shows significant settlement at its center along its the longitudinal axis. Figure 19 shows the absolute displacement beneath the existing tunnel. When the analysis results for the 3.5 m spacing case using the proposed method and the conventional method are compared, it becomes clear that the proposed method shows a steeper displacement gradient. However, the maximum value of absolute settlement is greater using the conventional method than the proposed method.

4.4 Comparison of conventional and proposed methods for ultra-close proximity construction

In railway operations, relative displacement is a key factor in assessing the safety of trains in operation, and it also correlates with the internal forces generated by existing tunnel components. When assessing the safety of railway operations relating to neighboring construction, track stiffness is excluded in the evaluation. Instead, the relative displacement of the track structure is calculated and compared with the

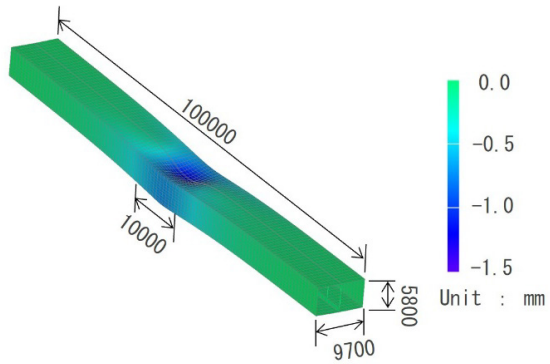

Fig. 18 Deformation contour of the existing tunnel

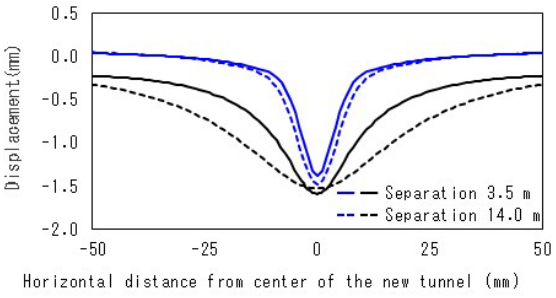

Fig. 19 Absolute displacement beneath the existing tunnel (conventional method and proposed methods)

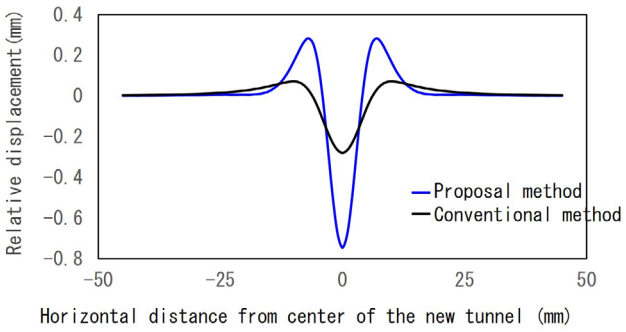

Fig. 20 Comparison of relative displacement (10 m chord) at a separation distance of 3.5 m

allowable limits defined by railway track maintenance standards for safety verification [1]. Figure 20 shows the absolute settlement converted into relative displacement over a 10-meter chord. These were obtained using the proposed and conventional methods for a separation of 3.5 m, respectively, the results show that the proposed method, which calculates a steeper displacement distribution, produces a greater maximum relative displacement. This suggests that, when both the proposed and conventional methods are used to evaluate the reinforcement of existing tunnels, the proposed method is likely to play a leading role in determining the design strategy. Furthermore, this finding is consistent with previous ultra-close tunneling projects, where the conventional method alone was insufficient to reproduce the observed tunnel behavior, and ground improvement was required regardless of soil conditions to prevent the deformation predicted by the proposed method.

5. Conclusions

In this study, a new numerical analysis method was developed to simulate the behavior of existing tunnels affected by the loosened ground zone, which is a characteristic feature of ultra-close tunneling.

(1) A soil tank experiment was conducted using a trap door test apparatus to simulate ultra-close tunneling conditions. The experiment successfully observed the characteristic ground reaction distribution beneath the existing tunnel.

(2) A simulation analysis was conducted using the proposed method for the experimental case of ultra-close tunneling. The results accurately reproduced both the ground reaction beneath the existing tunnel and the measured axial strain.

(3) Trial calculations were performed under assumed full-scale construction conditions using the proposed method. The analysis revealed that, in some cases, the proposed method produces greater relative displacements than the conventional method.

In ultra-close tunneling, ground improvement has traditionally been applied uniformly, regardless of soil conditions. However, by applying the method proposed in this study to predict the impact on existing tunnels make it becomes possible to plan ground improvement measures based on actual ground conditions. It is hoped that the proposed method will be a useful tool in carrying out more precise and efficient protective measures for existing tunnels.

References

[1] Railway Technical Research Institute, "*Manual for Assessment and Planning in Neighboring Construction of Urban Railway Structures,*" 2007 (in Japanese).
[2] Japanese Geotechnical Society, *Geotechnical Engineering Practice Series No. 28* – "*Neighboring Construction,*" Maruzen, 2011 (in Japanese).
[3] Terzaghi, K., "*Theoretical Soil Mechanics,*" John Wiley & Sons, New York, pp. 66-76, 1943.
[4] Railway Technical Research Institute, "*Design Manual for Countermeasures Against Tunnel Damage,*" 1998. Railway Technical Research Institute (in Japanese).
[5] Japan Society of Civil Engineers, "*Standard Specification for Tunneling (Shield tunnels),*" 2016 (in Japanese).
[6] Published under the supervision of the Railway Bureau, MLIT, Edited by the Railway Technical Research Institute, "*Design Standards for Railway Structures and Commentary (Cut and Cover Tunnel),*" Maruzen, 2020 (in Japanese).
[7] Published under the supervision of the Railway Bureau, MLIT, Edited by the Railway Technical Research Institute, "*Design Standards for Railway Structures and Commentary (Foundation Structures),* " Maruzen, 2012 (in Japanese).
[8] Kusakabe, O., "*Some calculation on bearing capacity of strip footings on slopes,*" Soils and Foundations, No.325, 1985 (in Japanese).
[9] Murayama, S., Matsuoka, H., "*EARTH PRESSURE ON TUNNELS IN SANDY GROUND,*" Proceedings of the Japan Society of Civil Engineers, No. 187, pp. 95-108, 1971.3 (in Japanese).
[10] NITTA, Tactile Sensor system, https://www.nitta.co.jp/product/sensor/detail/ (Retrieved on: 2024/4/1).

Authors

Takashi NAKAYAMA, Dr.Eng.
Senior Chief Researcher, Head of Tunnel Engineering
Laboratory, Structures Technology Division
Research Areas: Tunnel Engineering

Akihiko MIWA
Senior Researcher, Tunnel Engineering Laboratory, Structures Technology Division
Research Areas: Tunnel Engineering

Tatsuki SHIMIZU
Researcher, Tunnel Engineering
Laboratory, Structures Technology Division
Research Areas: Tunnel Engineering

Applicable Conditions for Polyurea Resin Spraying Method for Water Leakage and Uneven Tunnel Lining Surfaces

Kazuhide YASHIRO **Atsuya OE** **Keisuke SHIMAMOTO**
Tunnel Engineering Laboratory, Structures Technology Division

Tomoya USHIDA **Masayuki SUZUKI**
Tunnel Engineering Laboratory, Structures Technology Division

Falling pieces of tunnel lining hitting a train could cause an accident. Regular tunnel maintenance to prevent this is therefore essential. Repairs are planned and carried out in areas where there is a potential risk of spalling. A method called the "polyurea resin spraying method," has been developed to prevent spalling by spraying tunnel linings with polyurea resin. This paper presents the results of a study carried out to extend the applicability of this method and some application examples: the effect of surface moisture during application on the adhesion strength of the resin, long-term durability in the presence of leaking water, adhesion strength of the resin on an uneven surface, and results of its application in a real tunnel.

Key words**:** *tunnel, lining, polyurea resin, water leakage, uneven surface*

1. Introduction

Tunnel lining spalling directly impacts operational safety on railways. Prevention using appropriate measures is thus paramount. The authors developed a method of spraying polyurea resin to counteract the spalling of tunnel linings [1], and are currently applying this method in the field.

The applicability of this method was evaluated using the toughness coat method design and construction manual (hereinafter referred to as 'the manual') [2]. Water leakage and uneven surfaces are common in railway tunnels. This raises the risk of spalling, and increases the need for such a prevention method. However, although Table 1 shows general conditions where this method can be applied when there is water leakage and uneven surfaces, there is a lack of detail. Consequently, it is impossible to determine exactly when the method can be used under such conditions, and so the method was not applied.

This paper provides clarification of use conditions based on the results of laboratory tests, and field tests conducted in an abandoned tunnel where this method was applied seven years ago, and actual works in an in-service tunnel with water leakages and uneven surfaces.

2. Items and methods of consideration

The items and methods for clarifying the applicable conditions are shown below.

(1-1) Effect of water leakage during application on adhesion strength

Many railway tunnels are old and have numerous joints and cracks, which can cause water to leak and flow on the lining surface.

Table 1 Applicable conditions (Created from [2])

Item	Criteria for judgment
Water leakage	No water leakage within working area
Surface unevenness	Up to about 10 mm

In addition, relatively cooler temperatures inside tunnels in summer can cause condensation and increase the moisture content on the surface of tunnel linings. If water leakage is observed, mortar is used as a temporary measure to prevent this. If the moisture content of the lining is high, the surface is dried with a heater to reduce the moisture content to below 8% before application. It is generally known that the adhesion strength of a primer decreases when water is present on the applied surface, but the extent of the effect and the mechanism of this decrease were still unclear. To address this, laboratory tests were conducted to examine the presence of water immersion before applying primer or spraying resin. From the test results, measures were devised to reduce the effect of water leakage, and the applicable conditions were clarified through actual works in an in-service tunnel with water leakages.

(1-2) Effect of water leakage from behind the lining on adhesion strength after spraying

As mentioned in (1-1), temporary measures are used to stop water leaks before application of the method in environments where there is water leakage. However, the temporary nature of these measures implies that after the spraying of polyurea resin, leaking water will get between the resin and the lining, and might reduce the adhesion strength. There were still some unknowns regarding the change in adhesion strength over time when water acts from behind the resin. To address this issue, adhesion strength tests were conducted in an abandoned railway tunnel where this method had been used seven years previously.

(2) Effect of surface unevenness on adhesion strength

Tunnels constructed a long time ago may have uneven lining surfaces due to construction technologies used at the time or the passage of time since they were put into service, which may cause mortar to flow away and expose aggregate.

The manual specifies that the guidelines are applicable to cases where the lining is uneven with aggregate exposure of about 10 mm. However, this has been determined empirically and the load-bearing capacity of uneven surfaces has not been confirmed. Laboratory tests were conducted focusing on surface unevenness.

The manual does not describe specific conditions in detail, such as whether this method can be used in areas with continuous unevenness. Therefore, on the basis of the results of the laboratory tests, measures were devised to reduce the effect of surface uneven-

Table 2 Test cases

No.	Water immersion	
	Before primer application	Before spraying
Case1	No	No
Case2	Yes (Wiped off with towel)	No
Case3	Yes (Not wiped off)	No
Case4	No	Yes (Wiped off with towel)

ness, and this method was actually applied in a tunnel with continuous unevenness to clarify the applicable conditions.

3. Study on the effect of water leakage during application on adhesion strength

Suzuki et al. [3] focused on the effect of surface moisture and conducted adhesion strength tests using pull-off adhesion tests and peel tests to confirm the effect of differences in moisture conditions on the adhesion strength of primers and polyurea resin. This chapter outlines the tests conducted and presents new considerations.

In a pull-off adhesion test, an attachment (40 mm × 40 mm) is fixed to a specimen using an epoxy resin adhesive. Once the adhesive has hardened, a cut is made around the attachment using a disk sander to reach the base material. The maximum tensile load is then measured using a pull-off adhesion tester. This is divided by the area of the attachment to determine the adhesion strength. In a peel test, a cut is made with a disk sander that is 20 mm wide and 200 mm long, reaching the base material. The polyurea resin is then clamped with a jig and pulled in a 90-degree direction to measure the maximum tensile load. This is then divided by the peel width of 20 mm to determine the adhesion strength.

The difference between the two tests is that the pull-off adhesion strength test is a uniaxial tensile test, whereas the peel test simulates actual peeling phenomena. The manual specifies that the adhesion strength should be confirmed using the pull-off adhesion strength test after spraying [2].

The test cases are shown in Table 2. The test focused on the presence of water immersion before the primer application or polyurea resin spraying. Here, water immersion was achieved by soaking the test specimen in a vat of water, then removing it and wiping the surface of it with a towel. Note that in Case 3, water droplets on the surface were simply wiped off with a wiper instead of a towel.

Figure 1 shows the results of the pull-off adhesion strength test. The standard value of 1.5 N/mm^2, which is specified in the manual [2], is also shown. Figure 2 shows the results of the peel test. The material manufacturer's in-house standard value of 1.0 N/mm is also shown. In both tests, the cases with water immersion before primer application (Case 2, Case 3) exhibited lower adhesion strength than cases without water immersion (Case 1) or cases with water immersion before polyurea spraying (Case 4). In particular, the peel test showed a large decrease in adhesion strength due to water immersion.

These two tests evaluate adhesion strength. Therefore, it is important to confirm the mode of fracture to evaluate adhesion strength correctly. Figure 3 shows the area ratio of the fracture mode. In the pull-off adhesion strength test, base material fracture (A Fracture) was predominant regardless of water immersion. However, as

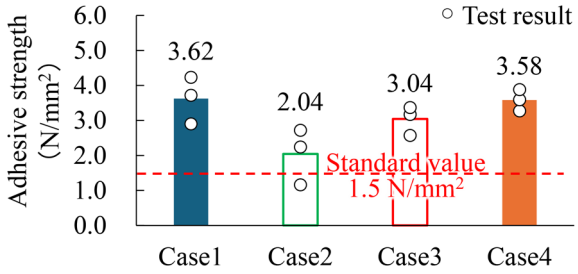

Fig. 1 Results of the pull-off adhesion strength test

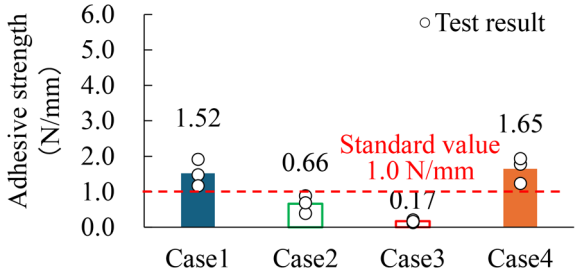

Fig. 2 Results of the peel test

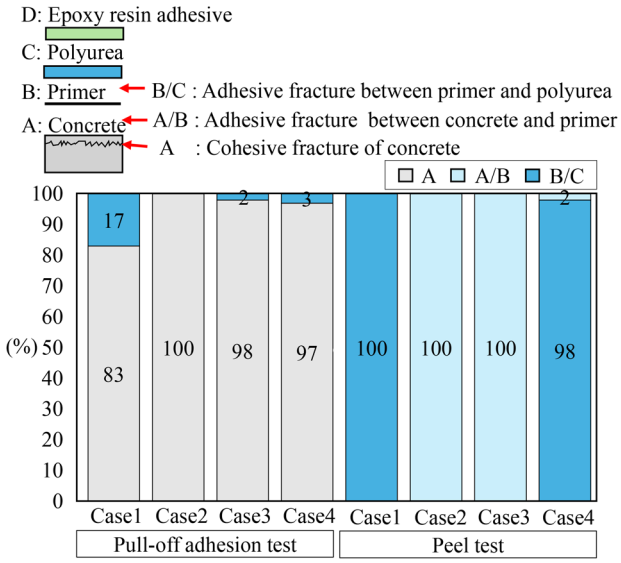

Fig. 3 Area ratio of fracture mode

shown in Fig. 4, it was found that the thickness of the fracture differed depending on whether or not the base material was immersed, even though the base material was the same. On the other hand, in the peel test, the fracture mode differed depending on water immersion. Primer/polyurea resin interface fractures (B/C Fracture) were seen without water immersion (Case 1 and 4), on the contrary, concrete/primer interface fractures (A/B Fracture) were seen with water immersion (Cases 2 and 3).

In the pull-off adhesion strength test, the tensile stress generated in the base material tends to be greater than in the peel test, and the rate of base material fracture tends to be higher. On the other hand, in the peel test, the tensile stress generated is small and base material fracture does not occur and it is thought that the decrease in interlayer adhesion due to water immersion is directly reflected in the adhesion strength.

From the above results, the fracture mechanism was considered

to be as shown in Fig. 5. The strength of the concrete surface is increased by the primer. In addition, if there is moisture on the surface, the penetration of the primer is inhibited. Specifically, without water immersion, applying the primer improves the adhesion strength of the interface between the primer and the concrete, as well as the strength of the concrete itself. Consequently, the concrete fracture depth is deeper in the pull-off adhesion strength test, and the primer/polyurea interface fracture occurs in the peel test. On the other hand, with water immersion, the effect of the primer on increasing the strength of the concrete surface is small, and the concrete fracture depth is shallower in the pull-off adhesion strength test. The fracture occurs at the concrete/primer interface in the peel test. It is thought that the presence of moisture on the surface inhibits primer penetration due to the formation of a poorly cured layer on the primer surface, which is caused by whitening, amine brushing, or reduced primer penetration into the concrete surface.

From the above, as the moisture content of the lining surface can significantly affect the adhesion strength of the polyuria resin, it is essential to stop the water leakage and dry the lining surface before application. In addition, a peel test is considered to be more effective than a pull-off adhesion strength test at identifying the tendency of adhesion strength to decrease due to the influence of water.

4. Examination of the effect of water leakage from the back of the lining after spraying on adhesion strength

In this chapter, we present the results of an adhesion strength test conducted seven years after spraying, to confirm the effect of a water leakage environment on the adhesion strength of sprayed polyurea resin. The tests were conducted using pull-off adhesion strength and peel tests [4].

The test site was a single-track tunnel on an abandoned line located in a cold region on the Japan Seaside of Honshu, where a test application of the polyurea resin spraying method was carried out in 2016 [5].

Table 3 shows the test cases. A total of six adhesion strength tests were carried out. Cases 1 to 3 show the results of tests carried out at locations where there was slight leakage before spraying. Cases 4 to 6 show the results of tests carried out at locations where there was no leakage before spraying, and are also shown for reference.

Figure 6 shows the temporary water stoppage at the location where there was leakage before spraying. Figure 7 shows the lining status of Cases 1 to 3 at the time of the adhesion strength test. Due to water leakage, a wide area was wet and it was assumed that the water leakage occurred between the resin and the base material after spraying.

Figure 8 shows the test results of the pull-off adhesion strength test. The triangles in the figure show the results of tests carried out on the concrete lining in 2016, which ranged 2.63 to 4.35 N/mm^2. The figure also shows the results of tests carried out one week and

Table 3 Test cases

No.	Water leakage		Surface treatment method (Reference)
	Before spraying (2016)	When tested (2023)	
Case1	Yes	Yes	Water jet (WJ)
Case2			Disc sander (DS)
Case3			Brushing
Case4*	No	No	Water jet (WJ)
Case5*			Disc sander (DS)
Case6*			Brushing

* Reference

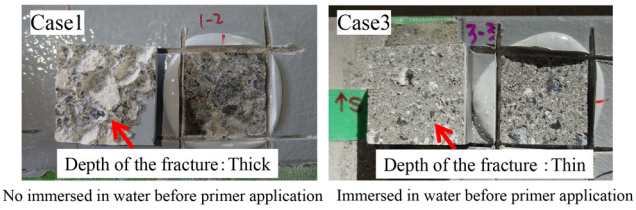

Fig. 4 Situation after adhesion strength test

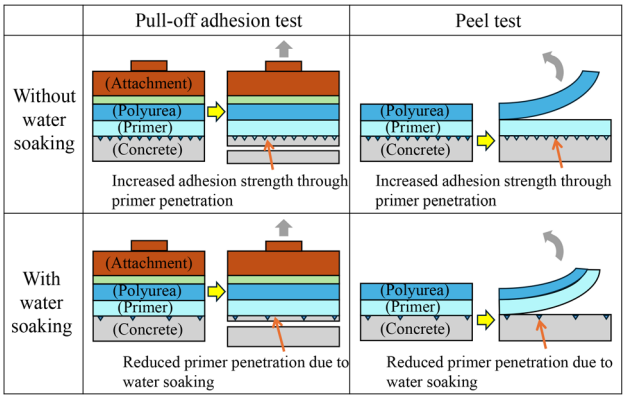

Fig. 5 Fracture mechanism

Fig. 6 Construction status of temporary water-stopping

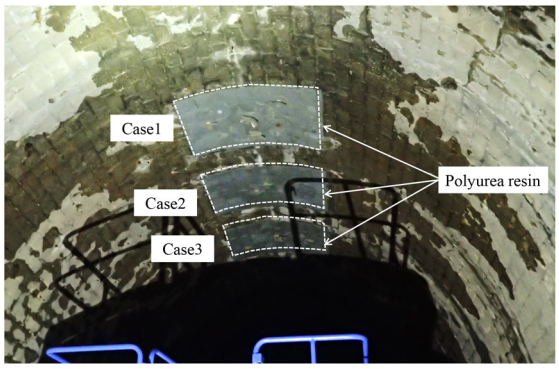

Fig. 7 Lining status at the time of an adhesion strength test

one year after spraying.

Considering these results, the influence of variation presumably due to the condition of the concrete blocks at the test site was significant. However, in all cases, the adhesion strength exceeded the average test value of 1.5 N/mm^2, which is the pass standard value for adhesion strength in the manual [2]. The pass standard value was satisfied even with the presence of water leakage and differences in surface treatment. In addition, in the test conducted seven years after spraying, more than half of the fraction occurred between the jig on the tester side and the adhesive that bonds the polyurea resin. This is thought to be because it was humid on the day of the test, the lining surface was wet due to condensation, and moisture prevented proper hardening of the adhesive. Therefore, the adhesion strength for the polyurea resin in the test results conducted seven years after spraying may be higher.

Figure 9 shows the results of the peel test. The adhesion strength in all cases exceeded the 1.0 N/mm in-house standard value specified by the material manufacturer, regardless of the presence of water leakage or differences in surface treatment. Focusing on the presence of water leakage, the peel test adhesion strength was generally lower in cases with water leakage than in cases without water leakage, but no tendency to change over time was observed.

For peel tests in which differences in adhesion strength were observed depending on the presence of water leakage, Fig. 10 shows the area ratio of the fracture mode. In the laboratory test in Chapter 3 [3], as shown in Fig. 3, the fracture mode was a concrete/primer interface fracture (A/B fracture) due to the influence of water immersion before primer application. However, in this test, even after 7 years, a concrete/primer interface fracture (A/B fracture) was not observed. This result shows the importance of drying the lining surface prior to applying the primer in order to improve penetration into the concrete surface and strengthen adhesion at the concrete/primer interface. This finding is consistent with laboratory tests in Chapter 3.

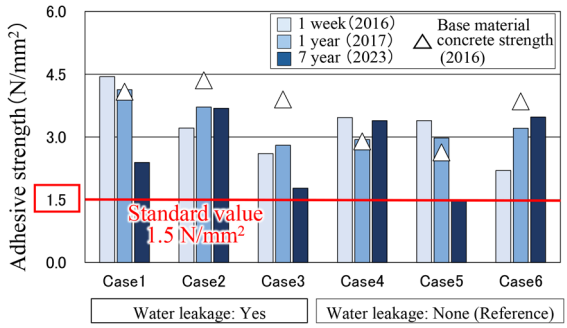

Fig. 8 Results of pull-off adhesion strength tests

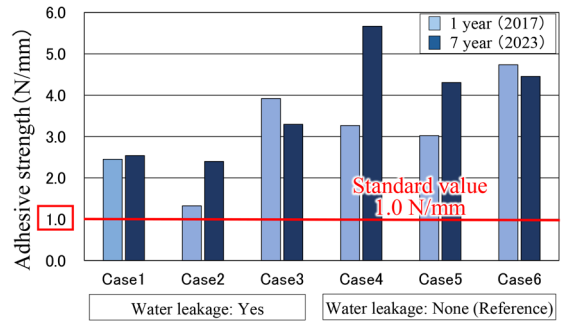

Fig. 9 Results of peel tests

5. Application and applicable conditions for tunnels with water leakage points

The test results in Chapters 3 and 4 showed that surface moisture due to water leakage during primer application significantly affects the adhesion strength of the polyurea resin. Therefore, it is essential to dry the lining surface before primer application. In addition, it was found that provided the surface is dried before application, the adhesion strength will not decrease significantly over the long term even if water leakage occurs behind the resin after application.

In this chapter, on the basis of the above findings, we present a case study in which the polyurea resin spraying method was employed in a real tunnel. We also demonstrate the water stopping and water guiding methods for addressing water leakage in the lining, and the applicability of these methods to different leaking patterns based on the results of actual works [4].

The tunnel in question was a single-track tunnel located in a mountainous area. It was 96 years old and had a concrete block lining. To prevent spalling of the coarse aggregate, the arch section of 142 m^2 was to be treated using the transparent polyurea resin spraying method [6], but an inspection of the tunnel lining surface revealed many water leakage points within the application area.

As the degree of leakage is subjective, we decided to classify the leakage into patterns according to source, shape of the source, and amount, and then created a process for judging whether it can be applied. As a result of the on-site investigation after surface treatment using water jets, leakage patterns were confirmed in the red square in Fig. 11, and a total of 104 leakage points (Fig. 12) were confirmed. The source of each leakage was identifiable.

Following application of mortar as a temporary measure to stop leaking water, it was expected that leakage would re-occur from adjacent points due to changes in the water path. Therefore, we considered installing a water guide pipe to steer dripping water onto the ballast, but taking care not to drip water onto the rail. The construction sequence for the water guide pipe involves three steps: (1)

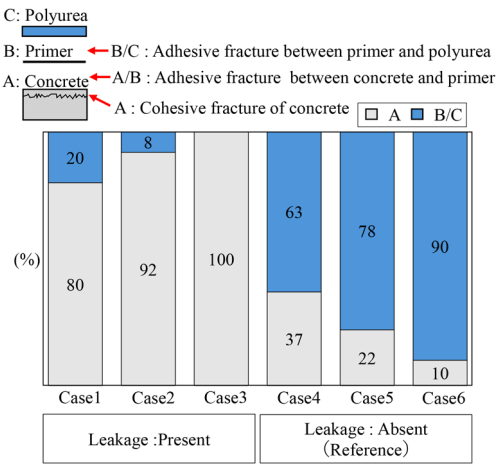

Fig. 10 Area ratio by fracture mode (Peel tests)

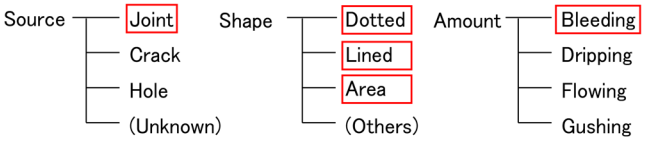

Fig. 11 Leakage patterns

drilling a hole at the source of the leakage, (2) inserting the water guide pipe, and (3) applying water stopping mortar (Fig. 13).

The work took a total of 19 days to complete the 142 m^2 working area, including six days for surface preparation using water jets, five days for water stopping and water guiding, four days for primer application, and four days for spraying polyurea resin. Working hours were about six hours during the night.

The actual work revealed that the effectiveness of the water guide pipes varied depending on the location of the water leakage.

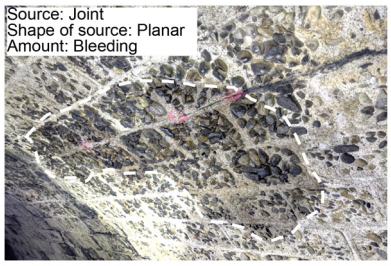

Fig. 12 Example of water leakage

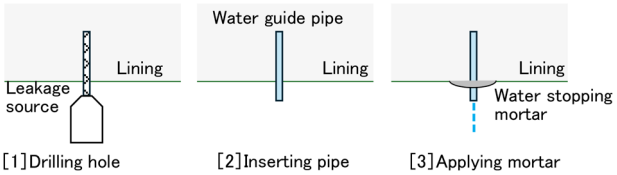

Fig. 13 Construction sequence of water guide pipe

Fig. 14 Example of water guiding work (At shoulder part of tunnel)

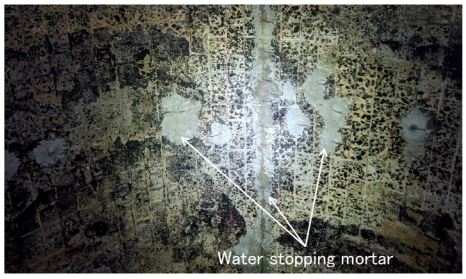

Fig. 15 Example of water guiding work (At crown of tunnel)

Figure 14 shows an example of water guiding work in the arched section, excluding the crown. It can be seen that water drips directly onto the ballast, while the surface of the lining remains dry. Figure 15 shows the water guiding work near the tunnel crown. It can be seen that, in the area where the water guide pipes were installed, water is not directed sufficiently and the water stopping mortar is wet. This is thought to be because the gradient behind the lining in the crown is gentle, which makes it easy for groundwater to pool behind the lining and easily leak into the interior of the lining through the joints. However, since the wet area was mostly contained within the area where water stopping mortar was applied, it can be said that in terms of reducing the wet area the effect was sufficient. It is thought that water guide pipes could be an effective means of expanding the area where this method can be applied.

Figure 16 shows the condition of the lining surface after spraying. It was possible to spray the polyurea resin continuously over a wide area, including the area where water leakage had been confirmed. In addition, the transparent resin provides sufficient visibility of the coarse aggregate parts and joints of the lining, facilitating subsequent inspections of the lining condition.

Adhesion strength tests were carried out on the lining, and an average strength of 1.7 N/mm^2 was achieved, with a minimum of 1.2 N/mm^2. These values exceeded the respective pass standard value of 1.5 N/mm^2 and 1.2 N/mm^2, specified in the manual [2] [7].

Figure 17 shows a flow chart for determining whether or not this method can be applied to a location with a water leakage. This chart was created based on the results of the actual work. Specifically, the site conditions are classified according to the degree of leakage in a preliminary survey, and the application area is determined by applying either a temporary water stopping mortar or water guide pipes, depending on the flow. Note that this flow chart assumes a tunnel made of concrete blocks.

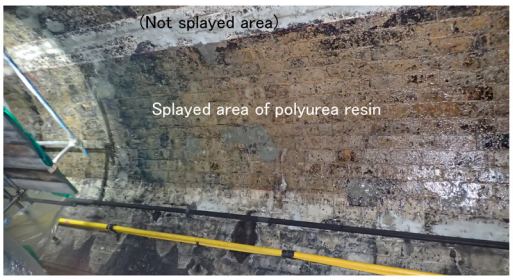

Fig. 16 Condition of lining surface after spraying

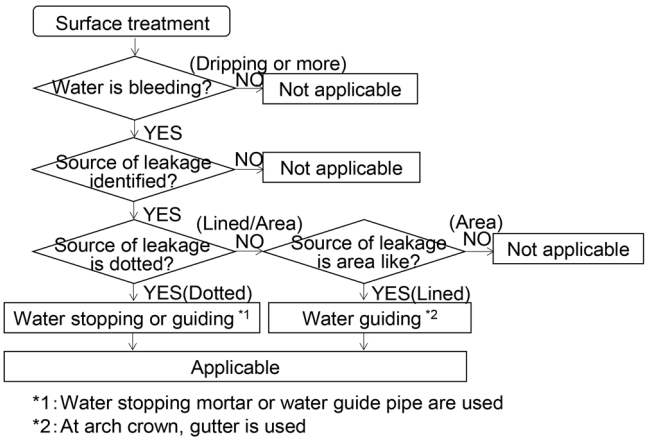

*1 : Water stopping mortar or water guide pipe are used
*2 : At arch crown, gutter is used

Fig. 17 Flow chart for this method

6. Consideration of the effect of surface unevenness on adhesion strength

This chapter outlines push-out tests [8] focusing on the presence of surface unevenness.

The tests were carried out using the loading test device shown in Fig. 18. Loading was performed at a speed of 5 mm/min, and temporarily stopped at each displacement of 5, 10, 20, and 30 mm, and the peeling area was marked on the test specimen.

The test cases were set as shown in Table 4, focusing on the presence of unevenness. Note that in Cases 2 and 3, unevenness was created on the surface using a pick-up hammer. In Case 2, the dents were made about 1 to 2 mm deep, while in Case 3 (Fig. 19), the dents were made approximately 5 to 8 mm deep in about 10 places within an area of 10 cm square.

Figure 20 shows the load-displacement curves for Cases 1 to 3. It can be seen that all cases met the performance satisfaction range (1.5 kN or more at a displacement of 10 mm or more [7]) according to the expressway standards of Japan. The maximum load was greater in the following order, Case 3 (large unevenness) < Case 1 (smooth) < Case 2 (small unevenness). The maximum load increased in Case 2 (small unevenness) compared to Case 1 (smooth). This is thought to be because the presence of unevenness allowed the resin to grip the surface more firmly, improving the apparent adhesion, as well as increasing the adhesion area itself. On the other hand, the failure mode in Case 3 (large unevenness) was the same as in Case 2 (small unevenness), but the maximum load was lower than in Case 1 (smooth). This is thought to be because the presence of large unevenness caused a large variation in the spraying thickness [8], which resulted in a thin coating forming in local areas and creating weak points. Therefore, in uneven areas, if the design value of the spraying thickness can be ensured, sufficient load-bearing capacity can be ensured, so thick spraying and additional spraying are considered important.

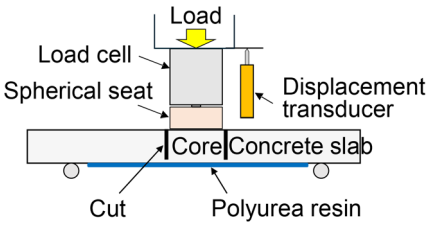

Fig. 18 Loading test device

Table 4 Test cases

No.	Surface condition
Case1	Smooth
Case2	With small unevenness
Case3	With large unevenness

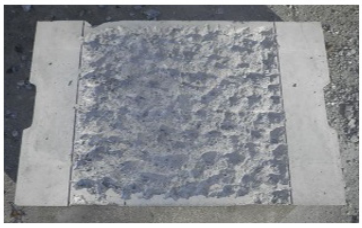

Fig. 19 Specimen with unevenness (Case3)

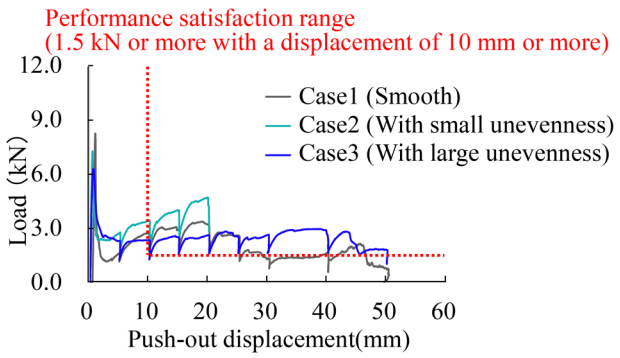

Fig. 20 Load-displacement curves

7. Application and applicable conditions for tunnels with continuous surface unevenness

In Chapter 6, it was found that, when applying the polyurea resin spraying method to a lining with surface unevenness, the required load-bearing capacity could be achieved by ensuring the specified spraying thickness through thick spraying and additional spraying. This chapter presents a case [9] in which the polyurea resin spraying method was applied, building on the knowledge presented in Chapter 6, and the scope of application was expanded through practical work.

The 87-year-old tunnel was located in a mountainous area, and had a lining made of cast-in-place plain concrete. The plan was to apply the polyurea resin spraying method to 15 m^2 of the sidewall to prevent the coarse aggregate from spalling. Following the surface treatment, an investigation revealed that the coarse aggregate was exposed and that there was unevenness of about 10 to 20 mm in the direction of the tunnel length (Fig. 21).

The polyurea resin spraying method relies on the adhesion strength of the resin. The current manual [2] states that the weight of the expected spalling area should be up to 0.5 kN. Therefore, an area with this adhesion strength is expected to exist around this area (Table 5). The manual also states that an anchoring length of 20 cm or more must be secured around the periphery of the expected spalling area (Fig. 22). Therefore, the conditions used in this case were not anticipated in the manual. However, since no water leakage was observed, the weak parts were removed by surface treatment, and attention was paid to the application of primer and polyurea resin spraying based on the degree of unevenness. It was therefore deemed that application of the method was possible.

The working area was 15 m^2, and each of the following processes was carried out during polyurea resin spraying. Actual work time was approximately three hours each night, when trains were not running. Figure 23 shows the primer being applied. The primer

Fig. 21 Unevenness of lining

was applied with a roller and a brush, to cover the entire surface of the uneven parts. The amount of primer used was 2.1 times the standard amount due to the increased surface area of the uneven parts.

Figure 24 shows the condition of the surface of the lining after spraying the polyurea resin. The polyurea resin was sprayed thickly because it was thought that it would be difficult to control the thickness of the coating due to the unevenness. The amount of polyurea resin used was 1.9 times the standard amount.

As a result of application, it was confirmed that the surface of the aggregate was covered with resin and that adjacent aggregates were joined together. After spraying, the adhesion strength measured by the adhesion strength test was found to be 1.9 N/mm^2 on average and 1.2 N/mm^2 at its minimum. These values exceeded the pass standard for adhesion strength in the manual [2], which is an average test value of 1.5 N/mm^2 and a minimum test value of 1.2 N/mm^2. The expected spalling from the target lining is similar in size to the coarse aggregate, and the expected spalling weight is much smaller than the 0.5 kN assumed in the manual (Fig. 22). Therefore, from the results of the actual work, the applicable conditions were organized as follows.

Table 5 Guideline to determine areas where adhesion can be expected (Addition to [2])

Item	Passing criteria
Soundness of base material	No loosening or floating of aggregate
Compressive strength of base material	Above design standard strength
Tensile strength of base material	Average: Over 1.5 N/mm^2 Minimum: Over 1.2 N/mm^2

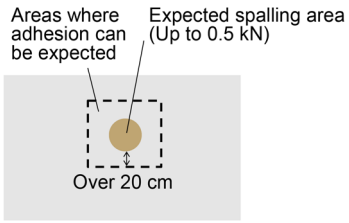

Fig. 22 Spraying area [2]

Fig. 23 Application of primer

Fig. 24 Condition of surface of lining after spraying

In cases where the expected spalling area is large and adhesion cannot be secured around the 20 cm length, but the expected spalling weight is small, the following conditions [1] to [3] must be met for this method to be applicable.

[1] The expected size of the spalling pieces is similar to that of coarse aggregate, so there is no concern of large concrete blocks falling off.
[2] Any weak parts have been sufficiently removed by prior preparation so that the lining surface does not easily fall off.
[3] The lining does not contain corroding or expanding materials, such as steel bars that promote spalling.

8. Summary

We organized the applicable conditions for the polyurea resin spraying method through laboratory tests, field tests, and actual works in tunnels in service with water leakage and continuous unevenness. The findings are summarized below.

(1) Effect of water leakage during application on adhesion strength
- It was found that a high moisture content in the lining surface due to water leakage during application has a significant impact on the adhesion of the polyurea resin. Therefore, it is essential to dry the lining surface before application.
- Compared to the adhesion test, which does not show the influence of fracture mode due to water immersion, the peel test is considered to be more effective in determining the tendency for adhesion strength to decrease due to water immersion.

(2) Effect of water leakage from the back of the lining after spraying on adhesion strength
- An adhesion test was conducted 7 years after spraying. As a result, no tendency of adhesion strength to decrease over time was observed.

(3) Application and applicable conditions for tunnels with water leakage
- Installing a water guide pipe before applying the prime helps to keep the lining surface free from water leaks.
- A flow was proposed through actual works to determine whether the polyurea resin spraying method could be applied, by classifying the leakage conditions into patterns.

(4) Consideration of the effect of surface unevenness on adhesion strength
- Even in areas with large unevenness, sufficient load-bearing capacity can be ensured as long as the design value for the spraying thickness is ensured. In such areas, thick spraying or additional spraying is important.

(5) Application and applicable conditions for tunnels with continuous surface unevenness
- This method can be applied by spraying the resin thickly.
- We have outlined the applicable conditions for cases where the expected spalling area is large and the length outside of that range where adhesion is required cannot be secured to the necessary 20 cm, but the expected spalling weight is small.

References

[1] Ito, N., Yashiro, K., Koshiishi, M. and Ide, K., "Development of spray-type anti-spalling measures using polyurea resin," *JSCE 71st annual meeting*, September 2016 (in Japanese).
[2] "Toughness coat method design and construction manual and commentary," JSCE, 2021 (in Japanese).

[3] Suzuki, M., Shimamoto, K., Kinoshita, K. and Yashiro, K., "Investigation on the effects of various factors on adhesion strength of polyurea resin spraying," *Proceedings of tunnel engineering*, JSCE, Vol. 33, I-33, 2023 (in Japanese).
[4] Oe, A., Ushida, T., Shimamoto, K., Yashiro, K., Miyata, Y., Ide, K. and Sasaoka, R., "Applicability of polyurea resin spraying method to tunnel with water leakage," *JSCE 79th annual meeting*, September 2024 (in Japanese).
[5] Yashiro, K., Shimamoto, K., Kamada, K. and Komiyama, M., "Test application of anti-spalling method for tunnel lining using polyurea resin at actual tunnel," *JSCE 72nd annual meeting*, September 2017 (in Japanese).
[6] Kubo, M., Miyata, Y. and Ide, K., "Development of the polyurea resin spraying method that allows visual inspection of the condition of the base concrete," *JSCE 77th annual meeting*, September 2022 (in Japanese).
[7] "Structure construction management guidelines," East Nippon expressway Co., Ltd. and others, pp. 2-322, 2013 (in Japanese).
[8] Itaya, S., Yashiro, K. and Shimamoto, K., "Performance evaluation of polyurea resin as an anti-spalling measure," *JSCE 72nd annual meeting*, September 2017 (in Japanese).
[9] Murata, K., Tagawa, K., Kubo, M., Miyata, Y., Oe, A., Sasaoka, R. and Ide, K., "Anti-spalling measure in railway tunnels by spraying transparent polyurea resin," *JSCE 79th annual meeting*, September 2024 (in Japanese).

Authors

Kazuhide YASHIRO, Dr.Eng.
Manager, Tunnel Engineering Laboratory, Structures Technology Division
Research Areas: Mountain Tunnels, Maintenance, Repair and Reinforce Works

Tomoya USHIDA
Assistant Senior Researcher, Tunnel Engineering Laboratory, Structures Technology Division
Research Areas: Mountain Tunnels, Maintenance, Repair and Reinforce Works

Atsuya OE
Researcher, Tunnel Engineering Laboratory, Structures Technology Division
Research Areas: Mountain Tunnels, Maintenance, Repair and Reinforce Works

Masayuki SUZUKI
Researcher, Tunnel Engineering Laboratory, Structures Technology Division
Research Areas: Mountain Tunnels, Maintenance, Repair and Reinforce Works

Keisuke SHIMAMOTO, Dr.Eng.
Senior Researcher, Tunnel Engineering Laboratory, Structures Technology Division
Research Areas: Mountain Tunnels, Maintenance, Repair and Reinforce Works

Impact of Tamping on Repeated Ballast Settlement

Takahisa NAKAMURA **Tomoaki HIROO**
Track Structures & Geotechnology Laboratory, Track Technology Division

Akiko KONO
Track Dynamics Laboratory, Railway Dynamics Division

It has been confirmed that track irregularity gradually returns to its original shape after ballast tamping on ballasted track even under the same track and support structure conditions. However, the details of this mechanism are not yet clear. Therefore, we surveyed an actual situation using track inspection data for this phenomenon. In addition, we performed tests with small-model, discontinuum analysis for ballast density after ballast tamping and cyclic loading tests, to reveal the mechanism of reversion in settlement after and before ballast tamping.

***Key words*:** *ballast memory, small model test, discontinuum analysis, ballast density, tamping*

1. Introduction

In ballast tracks, cyclic train loading induces settlement of the ballast beneath the sleepers, resulting in differential settlement of the rail level (hereinafter referred to as *track irregularity*). Such displacement not only deteriorates riding comfort but also reduces running safety. Previous studies have shown that ballast settlement tends to be greater at specific locations, such as structural boundaries—where track support stiffness changes abruptly, for example at transitions between embankments and viaducts (Fig. 1)—and at rail joints, where large impact loads are likely to occur [1-5].

Track irregularity is routinely monitored, and maintenance operations are conducted to restore the level of the rail at locations exhibiting significant displacement. During these operations, the rail is lifted using jacks, and a specialized vibrating device known as a *tamping machine* is used to compact the ballast beneath the sleepers (hereinafter referred to as *tamping*). This work not only restores the level of the rail, but also significantly alters the arrangement of the particles in the ballast beneath the sleepers. Consequently, except in locations prone to track irregularity—such as structural boundaries and rail joints—it is generally unlikely that the distribution of track irregularity after tamping would be the same as before tamping.

However, in track sections with continuous and uniform cross-sectional profiles and support structures along the longitudinal direction, instances have been observed where track irregularity recurs at the same locations after tamping, with the distribution of track irregularity returning to its pre-tamping state. The underlying mechanisms of this phenomenon remain unclear. This recurrence of track irregularity patterns is referred to internationally as *Ballast Memory* [6].

To elucidate the mechanism underlying ballast memory, this study analyzes its occurrence using track monitoring data. It also conducts reproduction experiments using small-scale physical models and performs discontinuous numerical analysis, focusing on ballast density after tamping. These approaches examine the influence of tamping on the manifestation of ballast memory.

2. Investigation of ballast memory phenomenon

2.1 Analysis of ballast memory occurrence

Using track measurement data from Shinkansen tracks, locations exhibiting characteristics of ballast memory were identified by analyzing temporal changes in longitudinal level irregularities before and after tamping. Data extraction targeted long rail sections, excluding areas prone to longitudinal level irregularities such as turnout zones, expansion joint (EJ) sections, insulated joint (IJ) sections, zones within four meters before and after ballast replacement, zones within ten meters before and after structural boundaries, and zones within two meters before and after rail welds. To eliminate the influence of ballast fouling, only sections within five years of ballast replacement were considered.

A location was defined as exhibiting ballast memory if the point of maximum vertical displacement prior to tamping showed a recurrence of longitudinal level irregularities of three millimeters or more after tamping, and this cycle was repeated at least twice (Fig. 2).

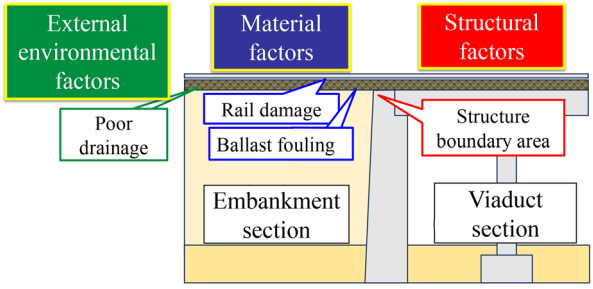

Fig. 1 Factors influencing ballast settlement

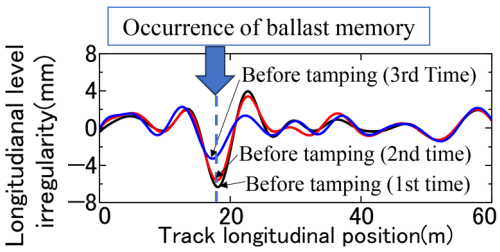

Fig. 2 Example of ballast memory occurrence

2.2 Analysis results

Of the 980 km of track surveyed, 96.3 km met the above criteria, with 388 instances of ballast memory identified within this section. Figure 3 shows the number of ballast memory occurrences per kilometer for the five types of track structures: embankments, cuttings, bridges, viaducts, and tunnels. Compared to the overall average of 4.0 occurrences/km, embankments and cuttings showed higher frequencies at 5.5 and 7.6 occurrences/km, respectively, indicating a tendency for ballast memory to occur more frequently in earth structure sections. This is likely due to the lower support stiffness in earth structures, which accelerates track settlement following ballast replacement.

Further analysis was conducted on tamping operations and post-maintenance track conditions at ballast memory locations. Two types of tamping method were considered: the Multiple Tie Tamper (MTT), which is used periodically, and the Handy Tie Tamper (HTT), which is used as needed. To examine recurrence trends, 153 locations were randomly selected from the 388 identified, where the tamping frequency was two times or fewer per year. Longitudinal level irregularity one year after tamping was classified as "recurrent settlement" if it exceeded 3 mm, and "suppressed settlement" if it was less than 3 mm.

The limitation on the frequency of annual tamping was imposed to ensure that individual tamping events could be analyzed independently. This prevents specific locations with frequent tamping and settlement cycles from having an excessive influence on the overall dataset.

Figure 4 shows the recurrence and suppression rates following MTT and HTT operations. One year after tamping, the recurrence rate was approximately 60% for MTT and over 80% for HTT, suggesting that tamping operations may influence the occurrence of ballast memory. The average longitudinal level irregularity prior to tamping was 4.1 mm for MTT and 5.2 mm for HTT, indicating that HTT was applied to locations with greater initial displacement.

The difference in recurrence rates between MTT and HTT can be explained by their respective application contexts. MTT is usually carried out once every one to two years on entire track sections, whereas HTT is often used at locations that require more frequent maintenance due to rapid settlement. Therefore, HTT is more likely to be used at locations prone to ballast memory, which may explain the higher recurrence rate observed under the given extraction conditions.

These findings suggest that the amount of rail lift during tamping may influence the occurrence of ballast memory.

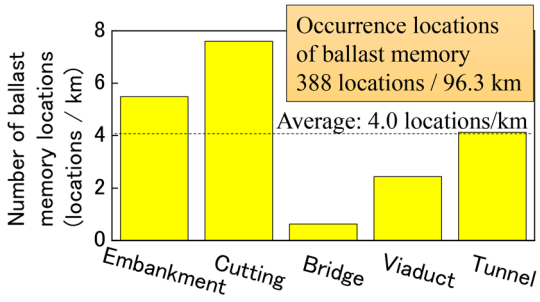

Fig. 3 Number of ballast memory locations per kilometer by structure type

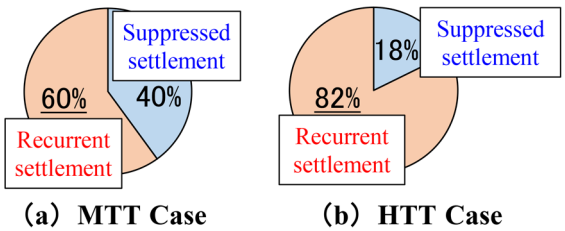

Fig. 4 Ratio of ballast memory recurrence after maintenance work

3. Reproduction testing of ballast memory using small-scale models

3.1 Model conditions

From the findings in Chapter 2, which revealed the occurrence of ballast memory even after tamping operations using a MTT, a reproduction test was conducted using a small-scale model. This test aimed to simulate ballast memory under conditions representative of earth structure sections—where settlement is more likely to occur and the quality of tamping tends to be more consistent. The test focused on the amount of rail lift during MTT works (Fig. 5).

1/5 scale model was constructed based on similar laws for dimensions and loading mass [7]. The model track was 4,000 mm long (equivalent to 20 meters at full scale), simulating a standard gauge ballasted track on an earth structure with a ballast layer thickness of 60 mm (equivalent to 300 mm at full scale). Crushed stone No. 6 was used as ballast, selected to meet the reference particle size distribution based on similarity laws (Fig. 6).

The track model consisted of 35 sleeper models made with mortar to simulate PC sleepers (type 3H), and two rectangular-section rails with a bending stiffness equivalent to that of 60 kg rails. The subgrade model was constructed using expanded polystyrene (EPS), with its thickness determined via finite element analysis (FEA) to match the stiffness of a uniform subgrade with a K_{30} value of 50 MN/m³. Specifically, the EPS thickness varied (100, 140, 200

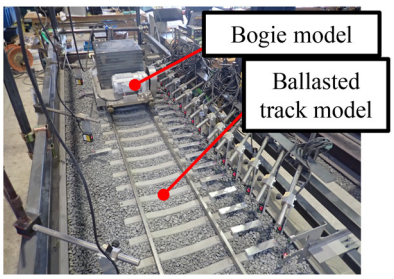

Fig. 5 Moving load test on small-scale model

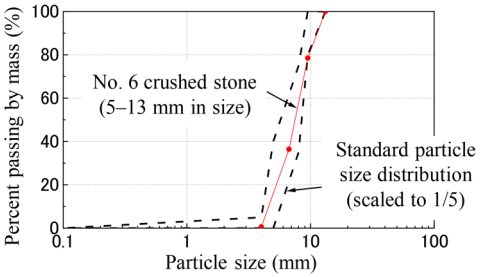

Fig. 6 Particle size distribution of No. 6 crushed stone

mm) in the small-scale model (hereinafter referred to as the model track) to match the subgrade displacement of the full-scale model (hereinafter referred to as the real track model) as shown in Fig. 7.

The applied load was determined by applying a dynamic impact factor of 1.35 for a Shinkansen train traveling at 285 km/h [8] and the similarity laws to a wheel load of 80 kN . This resulted in a wheel load of 864 N for the model track and 108 kN for the real track model. Two axles were applied at a spacing equivalent to one bogie. Load and material properties are shown in Fig. 7.

Figure 8 shows the subgrade displacement obtained from the FEM analysis. The displacement and longitudinal position are shown at full-scale. The EPS thickness that produced a subgrade displacement similar to that of the real track model (K_{30} = 50 MN/m³) was 140 mm.

To reproduce MTT tamping operations, a 1/5 scale MTT model was fabricated on the basis of a Plasser & Theurer 09-16D MTT tamping unit, considering the dimensions, mass, displacement amplitude, and squeeze amount of tamping tools (Fig. 9) [9].

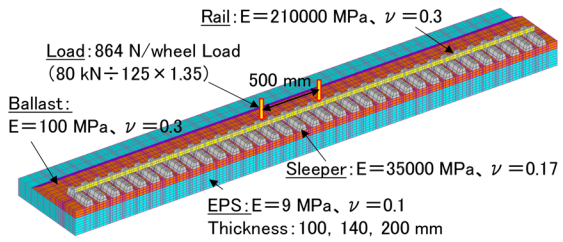

（a） Small-scale model

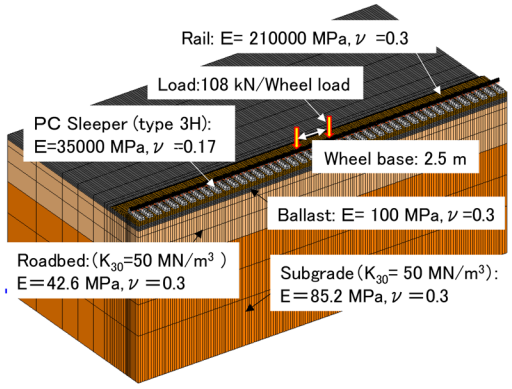

（b） Actual track model (K_{30} = 50 MN/m³)

Fig. 7 Analytical model used for examining subgrade layer configuration

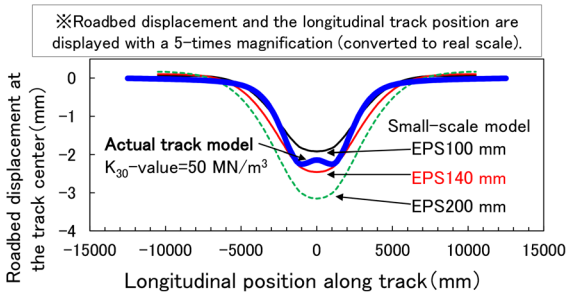

Fig. 8 Roadbed displacement obtained from FE analysis

3.2 Test conditions

To apply a wheel load of 864 N to the model rails, the bogie model was set to a total weight of 350 kgf (3430 N across four wheels), with an axle spacing of 500 mm. The load test using the bogie was performed by self-propelled movement at a constant speed of 500 mm/s over the central 2.0 m section (17 sleepers) of the 4,000 mm track (35 sleepers in total). The central sleeper was designated as Sleeper No. 9, and the 17 sleepers in the test section were numbered Sleeper No. 1 to No. 17. The test procedure is illustrated in Table 1. First, a preliminary loading test was carried out to apply tamping and loading works in advance to the ballast track. Tamping was performed using the MTT model by inserting the tamping tools beneath the sleepers, squeezing them laterally (hereinafter referred to as squeeze), and then withdrawing them—this sequence was defined as one tamping set. All sleepers were tamped under identical conditions.

To reproduce localized settlement, the tamping process during the preliminary loading was modified: for Sleepers No. 7 to No. 11 (central section),: only tool insertion was performed without squeezing. The preliminary loading involved 40,000 passes (20,000 round trips, equivalent to 80,000 axle loads) using the bogie model.

Subsequently, two loading cases were conducted. Each case involved one tamping set followed by 40,000 passes of loading. Prior to tamping, the track was levelled by lifting the entire track to a height of +1 mm above the least-settled sleeper (equivalent to +5 mm at full scale), meaning that sleepers with greater settlement were lifted by a greater amount (Fig. 10). The average vertical displacement in the 96.3 km of real track extracted in Chapter 2 before tamping was approximately 5 mm, and the lift amount in this test was set accordingly.

3.3 Test results

Figure 11 shows the distribution of sleeper settlement after 40,000 passes in the constant-speed test section (Sleepers No. 1 to No. 17). Preliminary loading caused significant localized settlement

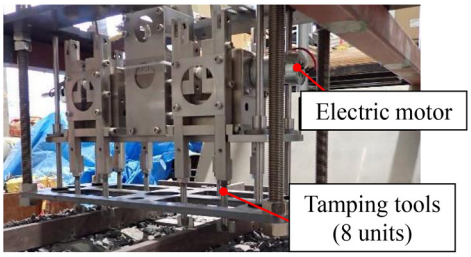

Fig. 9 MTT model

Table 1 Test procedure

Test procedure	Case	Implementation details	Number of passes
1	Preliminary loading	Compaction work using MTT model (*Sleepers No. 7-11 without squeeze*)	
2		Loading test	40,000
3	Case 1	Tamping work using MTT model	
4		Loading test	40,000
5	Case 2	Tamping work using MTT model	
6		Loading test	40,000

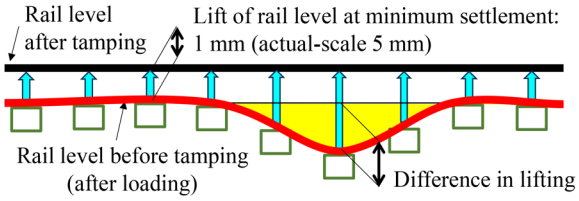

Fig. 10 Conceptual illustration of rail level before and after tamping

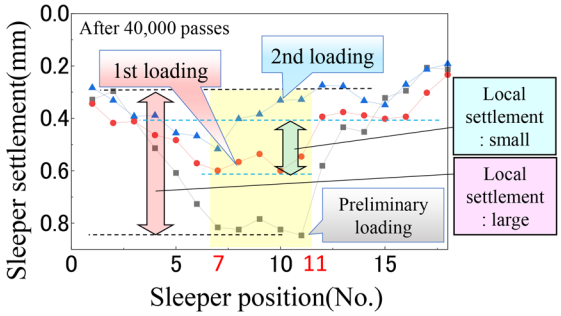

Fig. 11 Distribution of sleeper settlement after 40,000 passes (loading test)

in Sleepers No. 7 to No. 11. In the first loading case, localized settlement reoccurred in the same sleeper range, albeit to a lesser extent. In the second loading case, settlement at Sleeper No. 7 increased slightly, but the overall settlement was comparable to that of the adjacent sleepers.

These results suggest that localized settlement is more likely to reoccur under sleepers with larger lift, whereas recurrence is less likely under sleepers with smaller lift. In this test, unlike on real tracks, tamping was performed uniformly across all sleepers, regardless of lift. Therefore, it is inferred that lower ballast density after tamping sleepers with a larger lift led to greater settlement.

In actual MTT tamping, field workers determine the number of tamping sets per sleeper on the basis of site conditions and lift amount. In contrast, this test applied a single tamping set to each sleeper regardless of settlement, which may have influenced the observed results.

4. Evaluation of ballast density after tamping using discrete element method

The results of the small-scale model tests in Chapter 3 confirmed that the amount of settlement prior to tamping may influence the occurrence of ballast memory. To investigate this mechanism, a discontinuous analysis was conducted using the Discrete Element Method (DEM). DEM is a numerical technique that simulates the motion of numerous solid particles by solving translational and rotational equations of motion over time. The DEMCS-track program was used for the analysis [10].

Previous studies have examined the relationship between rail lift during tamping and the arrangement and deformation behavior of ballast particles using DEM [11]. However, the influence of rail lift on post-tamping settlement has not been fully explored. Therefore, this study evaluates how rail lift affects changes in ballast density during tamping and how ballast density influences initial settlement after tamping.

4.1 Conditions of the analysis model

To observe the three-dimensional behavior of ballast during tamping, a DEM model representing one sleeper's worth of ballasted track was constructed (Fig. 12). The sleeper was modeled as a type 3H sleeper with similar dimensions. The ballast elements were created as clusters of 10–16 particles per element [12] based on 3D shape measurements of andesite ballast. Nine different shapes were produced to reproduce the particle size distribution of new ballast. The subgrade was not modeled, as the analysis focused on relative comparisons of the behavior of the ballast before and after tamping.

Three cases were considered with rail lifting of 5 mm, 10 mm, and 20 mm. The modeling procedure was as follows: ballast was placed to achieve subgrade thicknesses of 295 mm, 290 mm, and 280 mm, respectively, and was then compacted to a density of 1.60 t/m³. Sleepers were then placed, and ballast was added up to the top surface of the sleepers. The total ballast volume was kept constant across all cases.

Table 2 summarizes the number of elements and particles used in the analysis model. The material properties were set according to previous studies [11] and are shown in Table 3. Due to the large scale of the analysis model (over 600,000 particles), the simulations were performed using a supercomputer with 36 parallel processes.

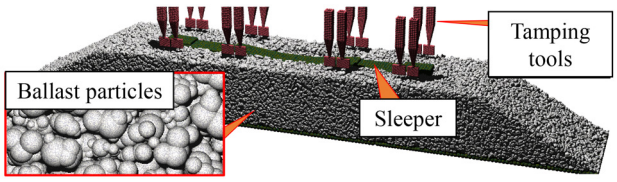

Fig. 12 Overview of analytical model

Table 2 Number of elements and particles in the analytical model

	Number of elements			Number of solid particles		
Ballast	Lift			Lift		
	5 mm	10 mm	20 mm	5 mm	10 mm	20 mm
	48,920	48,810	48,700	587,160	585,756	584,335
Sleeper	1			5,662		
Roadbed	3			7,402		
Tool	16			7,488		

Table 3 Material properties of each element

			Ballast	Sleeper	Roadbed	Tool
Spring constant	Normal direction	N/m	9.09×10^{6}	9.09×10^{6}	3.75×10^{4}	5.50×10^{8}
	Tangential direction	N/m	2.27×10^{6}	2.27×10^{6}	9.38×10^{3}	2.16×10^{8}
Damping coefficient	Normal direction	N/m	7.88×10^{2}	7.88×10^{2}	73.9	8.28×10^{3}
	Tangential direction	N/m	3.94×10^{2}	3.94×10^{2}	37	5.20×10^{3}
Friction coefficient		deg.	43	20	20	10

4.2 Relationship between rail lift and ballast density

4.2.1 Analysis conditions

In each model, the sleeper was lifted to a position where the ballast layer thickness reached 300 mm to simulate rail lifts. Tamping was reproduced by one set of operations: tool descent, 1-second squeeze, and tool ascent. The horizontal displacement amplitude of the tamping tool was ±2 mm at a vibration frequency of 35 Hz, consistent with actual MTT conditions. Vertical movement times during descent and ascent were set to 0.53 seconds, based on video analysis of real MTT operations. The tool was inserted to a depth of 100 mm below the bottom of the sleeper.

During the squeeze phase, the tool vibrated and moved horizontally to simulate gripping the sleeper (Fig. 13). The horizontal movement was controlled to stop when the force perpendicular to the sleeper reached 50 kN; thereafter, only vibration continued.

For the 5 mm lift case, one tamping set was performed. For the 10 mm and 20 mm lift cases, tamping was repeated until the average ballast density matched that of the 5 mm case after one set. This resulted in two sets for the 10 mm case and four sets for the 20 mm case. This enables us to examine the relationship between the ballast density and the settlement under both varying tamping repetitions and constant density conditions.

4.2.2 Analysis results

Figure 14 shows the change in ballast density per tamping set. Figure 14(a) presents shows the average density over the full 300 mm depth, while Fig. 14(b) shows the average density of the upper 100 mm-layer beneath the sleeper.

From Fig. 14(a), the 5 mm lift case yielded the highest density (1.64 t/m³) after one tamping set. The 10 mm and 20 mm cases reached densities of 1.65 t/m³ and 1.66 t/m³ after two and four sets, respectively. Thus, increasing the number of tamping repetitions improved the overall density.

However, Fig. 14(b) shows that the upper 100 mm layer had lower density than the full depth. Even after tamping, the 10 mm and 20 mm cases only reached 1.56 t/m³, compared to 1.58 t/m³ in the 5 mm case. This suggests that the narrow tool width and localized tamping near the rails limit the ability to fully compact the space beneath the sleeper.

In summary, while deeper ballast layers can achieve similar density through repeated tamping, the upper layer beneath the sleeper may remain less compacted in cases with a larger rail lift.

4.3 Relationship between ballast density and sleeper settlement

4.3.1 Analysis conditions

To evaluate the influence of rail lift and ballast density on sleeper settlement, repeated loading simulations were conducted after tamping. The loading condition involved applying a vertical sinusoidal load of at least 5 kN, with an amplitude of 110 kN, and a frequency of 10 Hz, for 50 cycles: equivalent to the axle load of one trainset.

4.3.2 Analysis results

The settlement amounts for the 10 mm and 20 mm lift cases were normalized against the 5 mm case (referred to as settlement ratio). Figure 15 shows the relationship between the settlement ratio

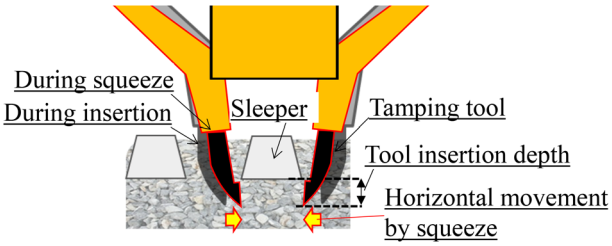

Fig. 13 Image of horizontal movement of tamping tools during squeeze process

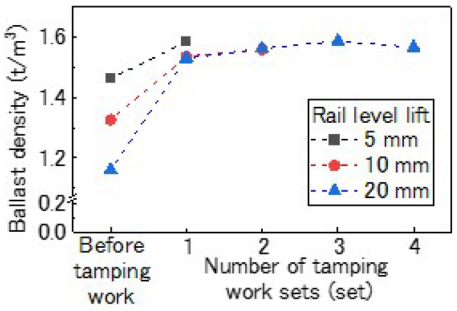

(a) Area from bottom of sleeper to depth of 300 mm

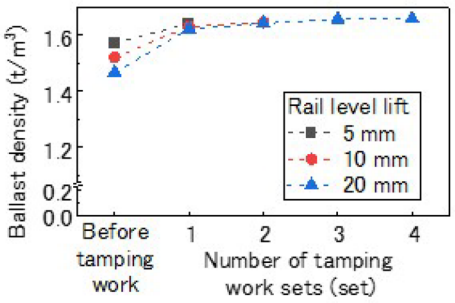

(b) Area from bottom of sleeper to depth of 100 mm

Fig. 14 Density change per set during compaction process

and ballast density (both full depth and upper layer). The regression equations and correlation coefficients are also shown.

A correlation was observed between the settlement ratio and ballast density, with the upper 100 mm layer showing a stronger correlation (R = 0.85) than the full 300 mm depth (R = 0.70). This suggests that the density of the ballast immediately beneath the sleeper has a greater influence on initial settlement.

Furthermore, the results indicate that larger rail lifts result in lower ballast density after one tamping set, leading to greater settlement. This supports the findings from the small-scale model tests, where localized settlement recurred at positions with larger rail lifts and lower ballast density.

5. Conclusion

This study investigated the influence of rail lift and ballast density on the occurrence of ballast memory through the analysis of field data, small-scale model testing, and discontinuous numerical

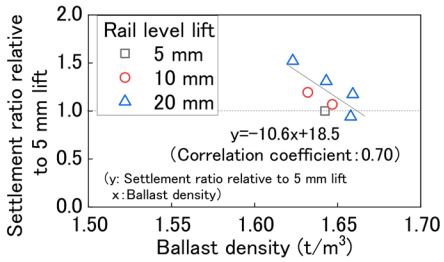

(a) Area from bottom of sleeper to depth of 300 mm

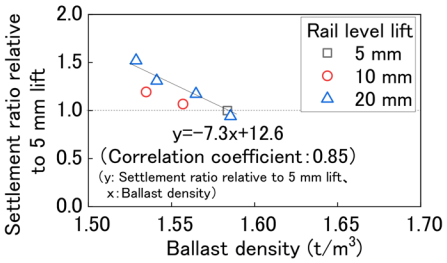

(b) Area from bottom of sleeper to depth of 100 mm

Fig. 15 Settlement ratio relative to 5 mm lift (50th loading)

analysis. The key findings are summarized below:

1. Field data from Shinkansen track monitoring revealed that ballast memory occurred in approximately 60% of locations after MTT tamping, and in over 80% of locations after HTT tamping. This suggests that tamping may influence the occurrence of ballast memory.
2. Reproduction tests using a 1/5 scale ballast track model demonstrated that ballast memory tends to occur at locations with larger rail lifts. Conversely, locations with smaller rail lifts showed less localized settlement and were less prone to ballast memory.
3. A Discrete Element Method analysis was conducted to examine the relationship between ballast density after MTT tamping and initial settlement under repeated train loading. The results indicated that insufficient compaction of the top 100 mm layer beneath the sleeper, particularly in cases with larger rail lift, could lead to increased settlement.

References

[1] Nakamura, T., Momoya, Y., Takahashi, T., Watanabe, A., Saeki, K., Nakade, C., "Method for Reinforcing Roadbed Using Prepacked Concrete with Ballast," *Proceedings of the 15th Joint Railway Technology Symposium*, pp. 119-122, 2008 (in Japanese).

[2] Sekine, E., Muramoto, K., "Study on Bearing Capacity Characteristics of Operating Track Roadbed," *RTRI Report*, Vol. 9, No. 7, pp. 19-24, 1995 (in Japanese).

[3] Kageyama, T., Nakamura, T., "Low-Strength Stabilization Method to Suppress Settlement of Deteriorated Ballast," *Journal of Japan Railway Civil Engineering Association*, Vol. 60, No. 8, pp. 619-622, August 2022.

[4] Hosoda, M., Konoya, Y., Mizutani, J., Terashita, Y., "Preventing Rail Breakage Increasing in Winter," *RRR*, Vol. 80, No. 6, pp. 38-43, 2023 (in Japanese).

[5] Muramoto, K., Nakamura, T., Sakurai, Y., "Countermeasure for Floating Sleepers at Rail Joints Using Automatic Settlement Correction Auxiliary Sleepers," *RTRI Report*, Vol. 27, No. 4, pp. 6-17, 2013 (in Japanese).

[6] Earnest T. Selig and John M. Waters, *Track Geotechnology and Substructure Management*, 1994.

[7] Kagawa, T., "Similarity Law in Model Vibration Tests of Soil Structures," *Journal of JSCE*, No. 275, pp. 69-77, 1978 (in Japanese).

[8] Ito, I., Momoya, Y., Kageyama, T., Nakamura, T., "Evaluation of Plastic Settlement of Shinkansen Embankment Considering Train Speed Based on Cumulative Damage Theory," *Journal of JSCE*, Vol. 79, No. 7, pp. 1-19, 2023 (in Japanese).

[9] Nakamura, T., Takaura, M., Kageyama, T., Hayakawa, Y., "Recovery Mechanism of Lateral Resistance of Ballast Bed by Ballast Track Stabilization Work," *RTRI Report*, Vol. 37, No. 3, pp. 9-15, 2023 (in Japanese).

[10] Matsushima, T., Saomoto, H., "Discrete Element Modelling for Irregularly-shaped Sand Grains," Proc. NUMGE2002: *Numerical Methods in Geotechnical Engineering*, pp. 239-246, 2002.

[11] Kono, A., Ferellec, J. F., Nhu, V. H., Saussine, G., "Ballasted Tracks Tamping Analysis and Optimization Using DEM," *Proceedings of WCRR 2019*, 2019.

[12] Kono, A., Matsushima, W., "Verification of Quantitative Accuracy in Predicting Residual Displacement of Single-Graded Crushed Stone Layer Using DEM," *Journal of JSCE A2 (Applied Mechanics)*, Vol. 77, No. 2, pp. 339-348, 2021 (in Japanese).

Authors

Takahisa NAKAMURA, Ph.D.
Senior Manager, Track Structures & Geotechnology Laboratory, Track Technology Division
Research Areas: Ballasted Track

Tomoaki HIROO
Researcher, Track Structures & Geotechnology Laboratory, Track Technology Division
Research Areas: Ballasted Track

Akiko KONO, Ph.D.
Senior Researcher, Track Dynamics Laboratory, Railway Dynamics Division
Research Areas: Ballasted Track

Application of Image Analysis 'Engine' to Night Vision Images of Railway Track Periphery

Atsushi SHIMIZU
Track Geometry and Maintenance Laboratory, Track Technology Division

Shintaro MINOURA
Track Dynamics Laboratory, Railway Dynamics Division

We developed a method for capturing and analyzing images captured at night and verified the feasibility for limit measurement and difference detection of the environment. The result confirmed that by combining infrared light projectors, it is possible to capture a clear image of the rail periphery. We also developed a method for measuring the distances around the platform and examined the measurement accuracy. The average error was less than 20 mm. Furthermore, we confirmed that the difference detection can be properly performed even for night vision images.

Key words**:** *image analysis, dark location, 3D point cloud, difference detection*

1. Introduction

Railway operators conduct inspections of railway track and other equipment based on the inspection cycle, timing, and items stipulated by each company's regulations. However, a majority of these inspections are conducted on-site by humans, which has increased demand for a system that is less labor intensive while ensuring railway vehicle operation safety. Given this background, research is currently being conducted on the development of a system that utilizes image analysis technology to support work currently undertaken by on-board inspectors who visually inspect the railway track periphery. Remarkable progress has been made in recent years to automate railway inspection tasks [1]. Previous research has involved the development of system for facilitating train patrols that uses image analysis technology. Research has also been conducted on an 'engine' for analyzing images around railway tracks (referred to as "the engine" in this paper), which is the core of this system. This engine consists of two functions: first, a structure gauge obstacle detection. This involves the analysis of images of the railway track periphery taken with a stereo camera mounted on the front of a commercial train (hereinafter referred to as "train frontal image") to detect objects fouling the structure gauge. The second is difference detection, which involves the detection of differences between images taken at two different times in order to extract environmental changes on the railway track periphery. Meanwhile, these image analysis technologies have been developed for their application to images taken during the day in lighted sections. Therefore, they are not applicable to images taken at night or in tunnels (night vision images), and restrictions apply on the time periods and sections that can be photographed. Enabling image analysis with night vision images is thought to expand the scope of operation of the train patrol support system, as well as further improve the practicality of this system.

Therefore, in this report, we describe the results of verifying the potential of platform limit measurement and difference detection using newly developed photography and image analysis methods. These methods will enable the detection of structure gauge obstacles and environmental changes in the railway track periphery by conducting night vision photography using a stereo camera that is installed at the front of the train.

2. Overview of image analysis engine around railway track

This engine uses images taken with a stereo camera that is installed at the front of a commercial train, which enables "structure gauge obstacle detection" and "difference detection of images at two times." In this section, we provide an overview of each function.

2.1 Structure gauge obstacle detection using multi-view stereo

This engine's obstacle detection uses a method called multi-view stereo, which uses multiple images to reconstruct high-density, highly accurate 3D spatial information (3D point cloud). The 3D point cloud reconstructed by this method is used to set a frame equivalent to a structure gauge within the point cloud, with objects within that frame being detected as obstacles.

The multi-view stereo calculates the change in the camera's position and attitude over time, which is directly linked to the accuracy of the reconstruction of the 3D point cloud, using a method called self-location estimation technology. This technology estimates changes over time from image data alone, with high accuracy.

2.2 Difference detection of images taken at different times

Images taken at different times and at the same position need to be matched in order to be subject to the difference detection in this engine. Therefore, each frame of an image taken at a certain time undergoes a search for the frame with the closest photography position from all frames of the reference image taken at a different time. Even so, the images are taken from a moving train, so the shutter timing is different for each run, obtaining image frames taken at exactly the same position is not possible. Therefore, the appearance of the object changes slightly between the two image frames to be compared. Furthermore, the lighting conditions change depending on the photography time, so these differences are corrected using a method which align the geometric arrangement and brightness of the two images to be compared (brightness normalization).

Differences that are not necessary for management, such as cars and pedestrians around railway track and swaying trees, can also be excluded from detection by identifying the type of subject in the image on a pixel-by-pixel basis using a deep learning model.

3. Development of night vision photography method and image sharpening method

We developed a photography method and image sharpening method to apply the image analysis technology, developed in previous research and described in Section 2, to images taken at night or in tunnels using a stereo camera at the front of the train. In this section, we describe the details of these developed methods.

3.1 Night vision photography method using near-infrared projectors

We adopted a night vision photography method using near-infrared projectors. This method irradiates near-infrared light, which is invisible to the human eye, and takes photographs by removing the infrared cut filter that is normally used in digital cameras. This is known as a method that can capture highly visible images at night in residential areas and facilities where visible light illumination is avoided. Infrared light is irradiated and photographs are taken, so images that include color information cannot be captured, but clear images that are close to black and white images can be obtained.

The digital cameras used in the train patrol support system that were developed for daytime photography are sensitive to infrared light so that they can capture the entire visible light wavelength band. Furthermore, the infrared cut filter can be removed. Therefore, we decided to use the same stereo camera as for daytime photography.

Next, we examined the near-infrared light projector arrangement method at the front of the train. Figure 1 shows the light projectors installed in a suitable arrangement, and Table 1 shows the specifications of the near-infrared light projectors.

The aim of the arrangement is to obtain images with higher visibility of the rails and tunnel walls by using diffuse light projectors to capture the overall outline of field of view while using the spot light projectors to irradiate in the center of the area being photographed.

3.2 Night vision image sharpening method

Using the photography method described in Section 3.1 is thought to enable the acquisition of images with good visibility even at night or in tunnels. Nevertheless, these images have low contrast and poor visibility compared to images taken during the day. In addition, the manner in which the light from the light projector hits an image is not uniform, and the lighting on the subject is uneven. Such characteristics of night vision images are a cause of accuracy deterioration in image analysis processing, and ultimately a cause of detection errors when image analysis processing is applied. Therefore, we developed an image analysis method that sharpens stereo images taken in dark locations so that they are in a format that is suitable for image analysis that has been developed for daytime images.

This method consists of two processes. The first is "illumination uniformization processing." We sought to solve problems seen in images taken in dark locations, such as low contrast and uneven contrast within the same image due to a limited lighting range, by estimating lighting from the pixel values of specific positions in the image and normalizing the overall lighting. This processing can improve the visibility of unclear areas as long as the image is not overexposed or underexposed.

The second is "denoising processing." A darker location with minimal light during photography results in greater noise caused by the sensor relative to the signal, which in turn emphasizes the noise in the image. Furthermore, applying the above-mentioned "illumination uniformization processing" further emphasizes the noise, which makes the noise even more likely to be erroneously restored during 3D reconstruction processing. We prevent this by smoothing the image to remove noise while preserving information such as the edges (contours of objects) in the image.

Figure 2 shows the results of applying the developed night vision image sharpening. We can see that the application of this processing eliminated the low contrast and non-uniformity in the image, and improved visibility of the shape of the object in the image.

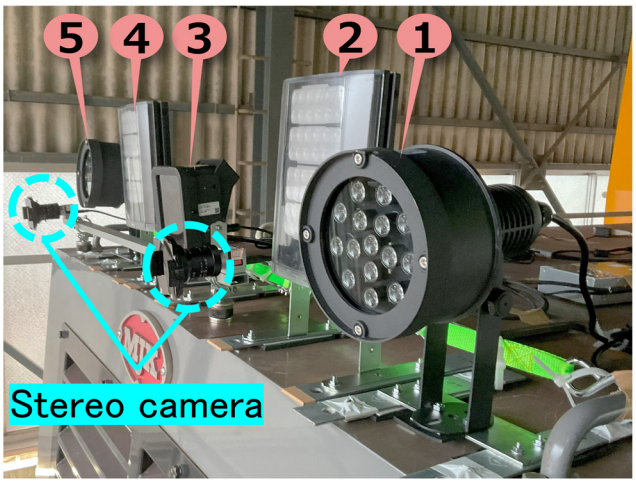

Fig. 1 Installation of near-infrared light

Table 1 Specifications of near-infrared light projector

Number in Fig. 1	②④	③	①	⑤
Features	Diffuse	Spot	Intermediate:A	Intermediate:B
Beam angle	120°	30°	60°	40°
Beam distance	65 m	200 m	120 m	180 m
Dimensions	W180 ×H280 ×D80 [mm]	W130 ×H170 ×D100 [mm]	Φ157 ×D228[mm]	Φ157 ×D228[mm]

4. Examination of applicability to platform limit measurement

Platform limit obstacles cannot be confirmed by patrol or visual inspection, so many operators use dedicated machines for their measurement. Previous research [1] examined the measurement accuracy of platform limits in a 3D point cloud space generated from daytime images, where they found that the average error was approximately 15 mm. The ability to use point clouds that are generated by train front stereo photography for the even night vision platform limit measurements is expected to further increase the efficiency of track inspections. Therefore, we examined a platform limit measurement method based on night vision images [2].

4.1 Study method

Here, we compared night vision images with daytime images. The frame rate during photography was 30 fps both at night and during the day. The running speed of the maintenance train that was

(a) Pre-application (original image)

(b) Post-application

Fig. 2 Night vision image sharpening method

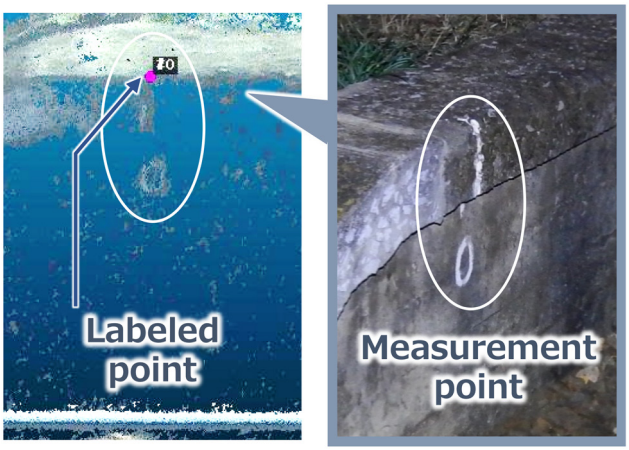

Fig. 3 Labeling of measurement points

equipped with the device was 10–20 km/h during night vision photography. Daytime photography was performed at the normal running speed of a commercial train (approximately 10–40 km/h due to station stops).

Next, we developed a method to calculate 2D cross-sectional data of the railway track using the 3D point cloud generated from the captured images. We then compared the results of calculating the platform separation and height distances with actual values measured on the same day using on-site dedicated equipment in order to examine the measurement accuracy using the 3D point cloud.

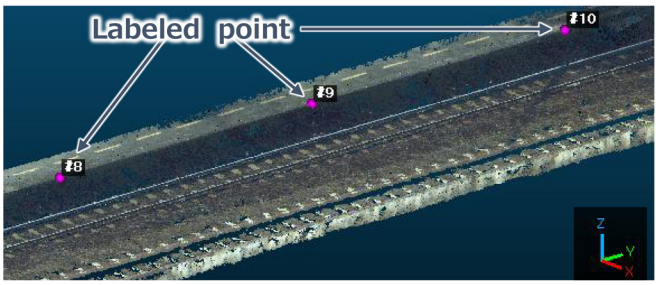

(a) Pre-extraction

(b) Post-extraction

Fig. 4 Extraction of railway track cross section point cloud

4.1.1 Labeling of measurement points

As shown in Fig. 3, the measurement points of platform separation and height marked on the site are identified on the generated 3D point cloud, and the point cloud is labeled. Locations where color information was lost due to generation conditions and where measurement points could not be identified on the 3D point cloud, had their labels added according to the distance from the confirmed measurement points.

4.1.2 Extraction of railway track cross-section point cloud

The 3D point cloud does not exist at the same density in 3D space. Therefore, for example, part of a platform may be between points in a certain cross section (approximately 1 kilometer), and the correct shape may be unobtainable. Therefore, as shown in Fig. 4, a point cloud equivalent to the railway track cross section is extracted from the coordinates of each labeled measurement point in the rail longitudinal direction. Here, we set the thickness of the cross section to 1.0 m (0.5 m forward or backward from the coordinate of the measurement point in the rail longitudinal direction). We also visually confirmed the railway track cross section point cloud that was extracted by the point cloud processing software, and we selected and deleted points that were not necessary for measurement or were clearly incorrectly reconstructed.

4.1.3 Creation of 2D cross-sectional data

The railway track cross-sectional point cloud extracted in Section 4.1.2 is a collection of points with vertical variation within the thickness of the cross-section. Therefore, as shown in Fig. 5, we divided the point cloud into equal intervals in the horizontal direction, the same as the rail head surface and the sleeper surface, and created 2D cross-sectional data that represents the representative value of the vertical coordinate within each range. Here, we divided

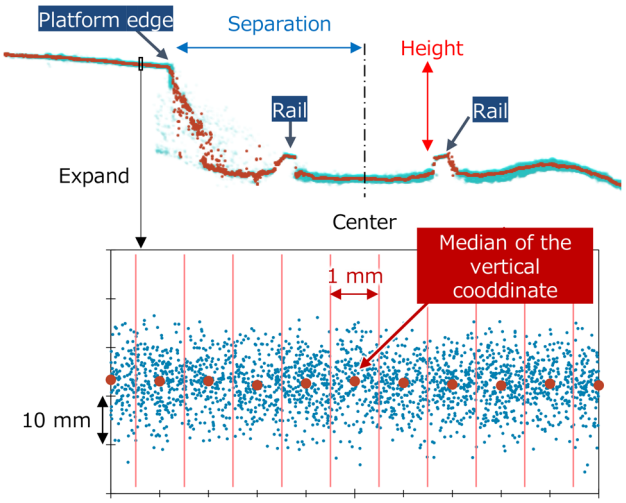

Fig. 5 2D plot of railway track cross section point cloud (light blue) and 2D cross section data (red)

the data into 1 mm intervals, and used the median value as the representative value.

4.1.4 Platform limit (separation, height) distance measurement

We selected points corresponding to the platform edge and the rail on the opposite side of the platform from the 2D cross-sectional data created in Section 4.1.3, and we calculated the platform separation and height from their vertical and horizontal coordinates. The platform separation was converted to a value based on the track centerline. Therefore, in this study, half the design gauge value (1,067 mm) was subtracted from the separation distance measured from the coordinates of the platform end and the rail.

Note that Figs. 4 and 5 show the processing results using the 3D point cloud created from daytime images ("daytime point cloud"), but the same processing was also performed on the 3D point cloud created from night vision images ("night vision point cloud"). We also examined two patterns of night vision point clouds. Namely, these were the point cloud created from images taken with only near-infrared light projectors illuminating the area (night vision point cloud A), and the point cloud created from images taken with normal illumination using both near-infrared light projectors and motor car headlights (night vision point cloud B).

4.2 Study results

Figure 6 shows the actually measured values of platform separation and height at each cross section and the measured values from the point cloud. Table 2 shows the error of the measured values from the point cloud with respect to the actual measured values. Note that the railway track cross section is extracted from a 3D point cloud by extracting a certain thickness (1.0 m in this case), so the calculated value is thought to include the actual change in the platform within the extracted thickness as an error.

These results suggest that the measured values from the point cloud roughly capture the actual measured values of platform separation and height in both daytime and night vision images A and B, and Table 2 shows that the average error was approximately 10 mm for the daytime point cloud and less than 20 mm for both night vision point clouds A and B. The maximum error was 18 mm for the daytime point cloud and 49 mm for both night vision point clouds A

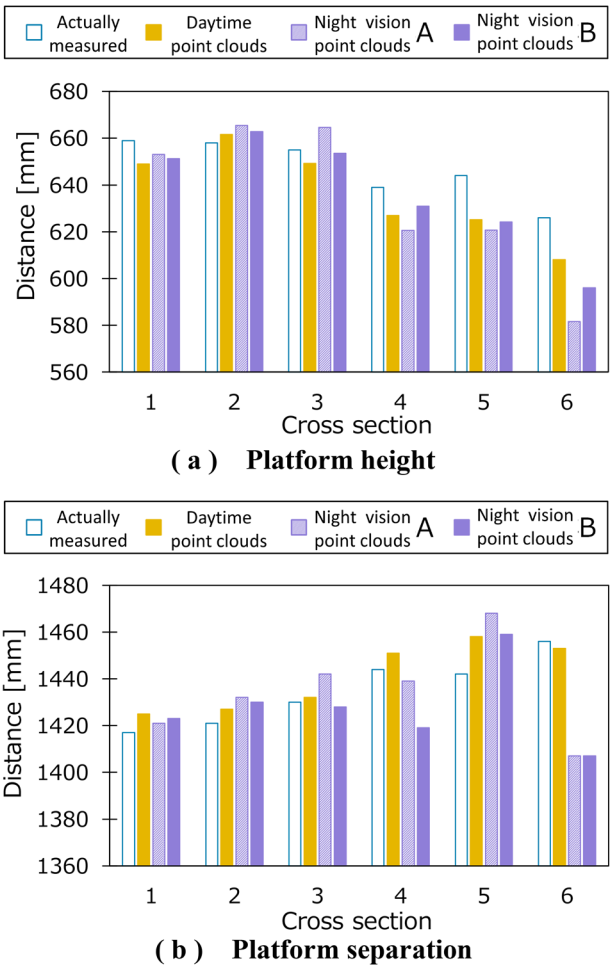

Fig. 6 Comparison of actual measured values and point cloud measured values

Table 2 Error from actual measured values (unit: mm)

Cross section	Height			Separation		
	Daytime	Night A	Night B	Daytime	Night A	Night B
1	-10	-6	-8	8	4	6
2	4	7	5	6	11	9
3	-6	10	-1	2	12	-2
4	-12	-18	-8	7	-5	-25
5	-19	-23	-20	16	26	17
6	-18	-44	-30	-3	-49	-49
Ave.	11	18	12	7	18	18

and B. Figure 7 shows the 2D cross section data and railway track cross section point cloud for cross section 6 of night vision point cloud A, where the maximum error was observed. This figure shows that the reconstruction of the cross-sectional shape of the platform end in the 3D point cloud contains a large amount of noise. This is thought to be due to the erroneous reconstruction of the point cloud to fill the space on the flat surface above the platform and in the corners below the platform, where there are few feature points and where brightness values on the image are similar. The reason for the particularly large error in cross section 6 of the night vision point

cloud is thought to be that cross section 6 is near the end of the platform, and the image feature points corresponding to the platform are reduced compared to other cross sections, which deteriorates the accuracy of the 3D restoration around the edge of the platform.

The above results indicate that distance measurements using 3D point clouds created from night vision images may have larger errors from actual measurements compared to daytime images, but that the trends of the actual measurements can be captured. Therefore, the results suggest that the inspection of platform clearance and height measurements conducted in this study can be used to screen areas requiring further attention.

5. Examination of applicability of difference detection

The ability to apply image analysis technology for difference detection of images taken at two different times to images taken at night and in tunnels, as well as at stations, bases, and subways where sunlight is blocked by structures, using near-infrared light, is thought to expand the scope of operation of the train patrol support system and further improve the practicality of this system. Therefore, we investigated a method for difference detection using "train frontal images" taken at night using a near-infrared spotlight [3].

5.1 Study method

Figure 8 shows the images taken in this study. The frame rate during photography was 30 fps, and the running speed of the maintenance train equipped with the device during night vision photography was 20–30 km/h. As described in Section 2, difference detection is a method of comparing an input image (test image) with an image taken at a different time on the same route (reference image). Here, we set the image taken with an obstacle installed (Fig. 8) as the test image, and the image taken without the obstacle installed as the reference image.

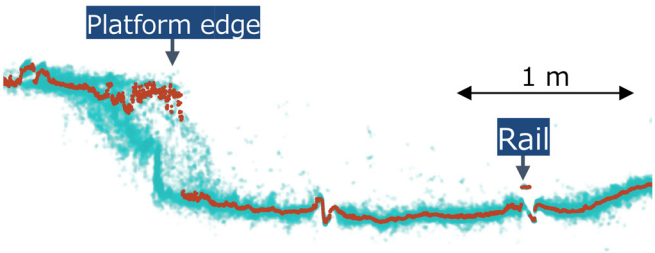

Fig. 7 2D cross sectional data of cross section 6 of night vision point cloud A

In this study, we varied two program parameters of the difference detection that have a large effect on the results, and investigated the appropriate settings for use with night vision images. The first parameter was the presence or absence of brightness normalization, as described in Section 2.2. The second parameter was the threshold for determining the sensitivity of difference detection. In this engine, the degree of mismatch is given as 0 to 255 for each coordinate on the image, and in this study, we used the three thresholds of 4, 12, and 20 as the sensitivity parameters for strong, medium, and weak sensitivity, respectively. Previous research using daytime images [4] used the settings "brightness normalization present" and "medium sensitivity."

5.2 Study results

Figure 9 shows the results of applying difference detection to images from inside the tunnel at point ① according to parameter condition. When"brightness normalization"was applied, results showed that the presence or absence of obstacles could not be detected regardless of the sensitivity parameter used. In contrast, when "brightness normalization" was not applied results show that "high sensitivity," conditions yielded false detection (over detection) of most images, including the presence or absence of obstacles; whereas "medium sensitivity" and "low sensitivity" conditions resulted in the detection of presence or absence of obstacles without any prominent over detection. Images taken in dark locations contain less color information than daytime images, and the contribution of brightness in the image is relatively high. Therefore, the application of brightness normalization processing that is designed for daytime images to night vision images is thought to exaggerate the process leading to an inability to detect the difference between images taken at the two different times.

Table 3 shows the results of the difference detection for each lighting condition and location in this study. This shows the results of applying the difference detection program to pairs of night vision images acquired at each location with varying parameters. This table shows that application of "brightness normalization" parameters usually used for daytime images to night vision images, yields neither non-detection or over detection of obstacles in most cases regardless of how the sensitivity parameters were set. Meanwhile, cases with no "brightness normalization" yielded good results, particularly at "weak sensitivity."

These results show that appropriate setting of parameters enabled difference detection even for night vision images. These results suggest that difference detection could be effectively used for determining the railway track periphery environment by using near-infrared light to take pictures in dark locations, such as at night or inside a tunnel.

(a) Point ①: Inside tunnel **(b) Point ②: Tunnel exit** **(c) Point ③: Lighting section**

Fig. 8 Images taken with obstacles installed

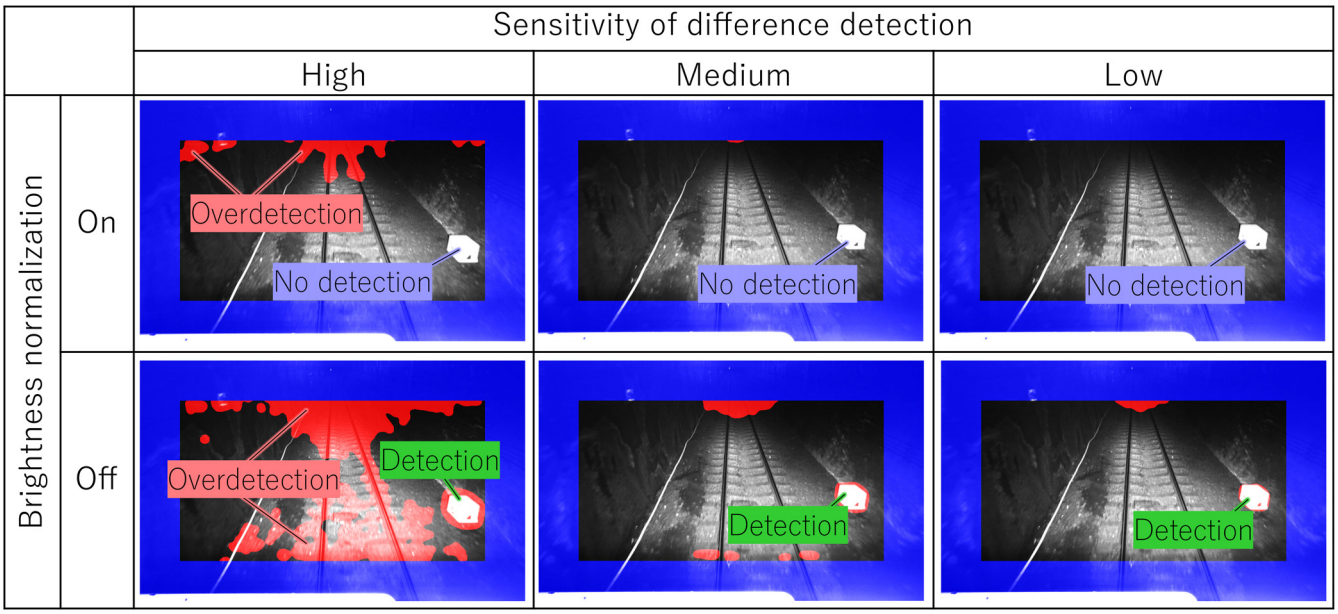

Fig. 9 Difference detection results at point ① inside tunnel (red areas indicate difference detection locations, blue areas indicate non-detection areas)

Table 3 Difference detection result judgment list

Parameters		Detection status		
Brightness normalization	Sensitivity	Point①	Point②	Point③
On	High	No detection	Detection	Overdetection
	Medium	No detection	No detection	No detection
	Low	No detection	No detection	No detection
Off	High	Overdetection	Overdetection	Overdetection
	Medium	Detection	Slight over detection	Slight over detection
	Low	Detection	Detection	Detection

6. Conclusion

We developed a photography method and image analysis method to enable detection of obstacles fouling the structure gauge and environmental changes around railway track by taking pictures at night using a stereo camera at the front of the train. We also verified the feasibility of using the developed method for platform limit measurements and difference detection. The findings were as follows:

(1)We found a way to analyze images taken even in dark locations. This was achieved by developing a method to clearly take pictures of the rail periphery. These pictures serve as the basis for dimensional measurement by image analysis, while capturing the overall outline of the image of the tunnel wall or other structures. The method combines near-infrared projectors with different irradiation angles and distances.

(2)We developed a method to calculate the 2D cross section of the railway track from the 3D point cloud data obtained by the developed night vision photography method, and to measure the distance from the platform and the height. We investigated the measurement accuracy of the distance from the platform and the height from the 3D point cloud generated by the night vision "train frontal image," and the average error was less than 20 mm.

(3)We input the captured night vision images to a difference detection program in order to investigate whether the program could detect the presence or absence of obstacles installed on the periphery of railway tracks. Results confirmed that this was possible by not applying the brightness normalization process, which gives good results when used for daytime images, and by weakening the detection sensitivity compared to daytime images.

Acknowledgment

Part of this research was conducted with the support of a Railway Technology Development Subsidy from the Ministry of Land, Infrastructure, Transport and Tourism.

References

[1] Konno, S., Kawasaki, K. et al., "Image Analysis Engine for

Supporting Onboard Track Patrol," *RTRI Report*, Vol. 36, No. 3, pp. 5-10, 2022 (in Japanese).
[2] Konno, S., Minoura, S. et al., "A Study on Application of 3D Point Cloud Reconstructed from Night-vision Images Taken by Railway Dashboard Camera," *J-RAIL2022* , Vol. 29, No. S-2-8-2, 2022 (in Japanese).
[3] Konno, S., Minoura, S., Nakajima, N., "Study of Applying Difference Detection Program for Track Patrol to Night Vision Image," *Journal of Railway Engineering, JSCE* , No. 26, pp. 121-128,2022 (in Japanese).
[4] Mishima, K., Kawasaki, et al., "Track Condition Monitoring by Using Forward View Image for Work Saving of Track Maintenance," *Journal of Railway Engineering, JSCE*, No. 25, pp. 123-130, 2021 (in Japanese).

Authors

Atsushi SHIMIZU
Senior Researcher, Track Geometry and Maintenance Laboratory, Track Technology Division
Research Areas: Track Geometry Management, Carbody Vibration Control, Ride Comfort Evaluation

Shintaro MINOURA, Dr.Eng.
Senior Researcher, Track Dynamics Laboratory, Railway Dynamics Division
Research Areas: Concrete Sleeper, Numerical Simulation

Evaluation for Running Safety of Railway Vehicles against Localized Strong Winds

Hiroyuki KANEMOTO
Vehicle Mechanics Laboratory, Railway Dynamics Division

Yu HIBINO
Research and Development Promotion Division (Former)

High-rise buildings can create localized strong winds, a phenomenon known as "building-induced winds." However, safety assessment methods for trains running in the vicinity of such winds have not yet been established. Therefore, this study proposes a method to evaluate the running safety of vehicles against overturning by localized strong winds. Specifically, wind tunnel experiments, computational fluid dynamics analyses, and vehicle dynamics simulations were conducted to investigate the effects of localized strong wind caused by buildings on the behavior of railway vehicles. The results showed that when the rise time of the aerodynamic force acting on the vehicle is less than approximately 2 seconds, the ratio of wheel load reduction increases compared to static analysis conditions.

Key words**:** *crosswind, critical wind speed of overturning, vehicle dynamics simulation, building-induced winds, wind tunnel test, CFD analysis*

1. Introduction

The critical wind speed at which overturning occurs is one of the indices used to evaluate the safety of railway vehicles against crosswinds. It is defined as the wind speed at which wheel loads on the windward side become zero. In Japan, this evaluation is often made using the "RTRI detailed equation [1]" based on "Kunieda's equation [2]" [3, 4]. The RTRI detailed equation can be used to solve the relationship between external forces and windward wheel loads analytically, based on the static equilibrium of forces acting on a vehicle under conditions of spatially uniform, steady wind. On the other hand, it is well known that localized strong winds, known as "building-induced winds," occur in the vicinity of high-rise buildings. Additionally, localized strong winds exist due to the influence of surrounding topography, such as tunnel exits. In recent years, as railway operators have become increasingly aware of the risks posed by strong winds, there has been a growing demand to evaluate the safety of train operations in areas prone to localized strong winds. To assess the safety of vehicles running in these localized strong wind conditions, it is necessary to conduct a dynamic analysis of vehicle motion. Research on dynamic analysis of vehicles in strong winds includes studies examining the influence of crosswind fluctuation frequency on vehicle behavior [5, 6], and analyses of vehicle dynamics using general-purpose multibody dynamics simulation software [7, 8]. Additionally, studies on vehicle behavior in localized strong wind conditions have included running tests using vehicle models and performing parametric studies through simulations, assuming scenarios in which vehicles exit tunnel openings in strong wind [9]. Furthermore, research has been carried out that numerically investigated the dynamic response of railway vehicles in windy conditions at tunnel exits [10].

This study aims to provide insights that contribute to the development of operational regulations to enhance transport stability and ensure running safety. To achieve this, a detailed dynamic analysis was conducted of vehicle behavior in response to building-induced winds. Specifically, we focused on the effects of wind caused by two adjacent buildings on dynamics of vehicles. We conducted wind tunnel tests and computational fluid dynamics (CFD) analysis to estimate the aerodynamic forces acting on the vehicle. Then, we analyzed the vehicle behavior using a multi-body dynamics analysis software, "Simpack." Furthermore, using this model for analyzing vehicle behavior, we calculated the wheel load while varying the rise time and the rise range of the aerodynamic forces. This enabled us to identify the spatial conditions of aerodynamic force changes that require attention from an operational safety perspective.

2. Distribution of wind speed induced by flow between two adjacent buildings

2.1 Conditions for consideration

This study focuses on the wind speed distribution of building-induced winds caused by two adjacent buildings as a target of localized strong winds. To understand the wind speed distribution on a double-track viaduct located downwind of two adjacent buildings, we conducted wind tunnel tests using scaled models and CFD analysis using a numerical wind tunnel developed by the Railway Technical Research Institute [11].

First, the following insights are generally known regarding the effects of building-induced winds:

- The rate of wind speed increases with building height.
- The larger the windward face (width of the building) is, the larger the area where the wind speed increases.
- In addition to an increase in wind speed on both sides of the building, there is also an increase in wind speed between adjacent buildings.
- Wind speed tends to be highest when the distance between adjacent buildings is about 1/2 to 1 times the width of the building.

On the other hand:

- The influence of the vertical distribution of average wind speed is relatively small.
- The influence of building depth is smaller compared to the effects of height and width.

Based on these insights, two types of building model are examined in this report, both described in full-scale dimensions: one measuring 10 m (width) × 10 m (depth) × 50 m (height), and the other 20 m (width) × 10 m (depth) × 50 m (height). In determining

these sizes, the following points were taken into account, referencing the aforementioned conditions that intensify the effects of building-induced wind. First, regarding the width, two variations of 10 m and 20 m were selected to compare the impact of the windward surface area, using the typical length of a commuter train car (20 m) as a reference. As for the depth, since its influence on wind speed increase rate is relatively small, it was uniformly set at 10 m, considering the convenience of model construction for wind tunnel tests. Furthermore, the height was set at 50 m. Although taller buildings generally result in higher wind speed increase rates, this height was chosen to allow for ease of handling during wind tunnel tests, while taking into account the blockage ratio relative to cross-section area of the wind tunnel outlet. It is worth noting that in Japan, due to the relationship between the Building Standards Act and the Fire Service Act, many apartment buildings are constructed at or below the 45 m height limit. Therefore, using a 50 m-tall building in wind tunnel tests can be considered generally appropriate as a "severe but realistic condition" that might be encountered along railway lines.

2.2 Wind tunnel tests

Wind tunnel tests were carried out in the open test section of the Large Low-noise Wind Tunnel of the Railway Technical Research Institute. In the tests, a turbulent boundary layer was generated by installing nine spires with a height of 1000 mm at 500 mm intervals in the upstream section of the open test section, 3600 mm ahead of the center of the turntable. When organizing the wind tunnel test results in this chapter, the reference wind speed was adopted from the wind speed measured at a height of 364 mm above the open test section floor. This height corresponds to the center height of the vehicle model when installed. Specifically, when the wind tunnel test speed U_0 was 30 m/s, the reference wind speed was 26.71 m/s, and the average wind speed ratio at the reference wind speed position was 0.8905.

The models of buildings and double-track viaducts were constructed at a 1/40 scale. Note that in order to make it easier to understand, the sizes and arrangements of the buildings will be described using full-scale dimensions. Figure 1 shows these models placed on an open test section floor. As previously mentioned, two types of building models were used. The first type measures 10 m wide, 10 m deep, and 50 m high. The second type is 20 m wide and is formed by connecting two of the aforementioned models. Henceforth, the former will be referred to as the "S model" and the latter as the "W model." In the tests, two building models (either S or W) were placed adjacent to each other. The spacing between adjacent buildings was set at 5 m for S models and 20 m for W models. Two wind direction angles were tested for both the buildings and the double-track viaducts: 90-degree and 70-degree. These angles were set by rotating the turntable. The distance from the center of the windward track of the double-track viaduct to the leeward wall of the building was set at 10 m. The girder height of the double-track viaduct was 2.8 m, and it was installed so that the rail surface was at a height equivalent to 12 m from the ground.

Wind speed on the double-track viaduct was measured using a small hot-wire anemometer (Model 0962-00 (directional), manufactured by Japan Kanomax) installed at the reference wind speed measurement height. The wind speed data was recorded at a sampling frequency of 100 Hz for 40 seconds. The installation angle of the anemometer was adjusted when the turntable was rotated to change the wind direction angle relative to the model. This ensured that the wind speed was measured in the main flow direction of the wind tunnel airflow. Figure 2 shows an example of wind speed measurement positions, specifically for the W model at a 90-degree wind direction angle. Wind speed measurements were performed at the center of the windward track on the double-track viaduct when the test wind speed was U_0 = 30 m/s. As shown in Fig. 2, coordinates were defined along the rail direction on the double-track viaduct. Then, we set the midpoint of the spacing between the two buildings as 0, with the right side of the figure as the positive direction and the left side as the negative direction. For the 90-degree wind direction angle, measurements were taken at 2.5 m intervals, while for the 70-degree angle, measurements were taken at 10 m intervals. The wind speed measurement ranges for the S model were 0 m to 67.5 m at a 90-degree angle, and from −30.0 m to 60.0 m at a 70-degree angle. For the W model, at a 90-degree angle, the measurements ranged from 0 m to 97.5 m, and at a 70-degree angle, from −40.0 m to 70.0 m.

2.3 CFD analysis

CFD analysis was conducted to reproduce the wind tunnel tests described in the previous section. The numerical wind tunnel presented in reference 11 was used for the CFD analysis. Figure 3 shows the shape of the created model. Specifically, the turbulence generation devices (spires), building models, and double-track viaduct models were set up with the same dimensions and positions as in the actual wind tunnel test. CAD data was used for modeling these elements. The inflow wind conditions were set at a wind speed of 30 m/s and an air density of 1.2 kg/m^3. The computational grid was set to the standard of the numerical wind tunnel with dx = 20 mm, $dy = dz$ = 10 mm. The height at which wind speed was evaluated was set to be the same as the height at which wind speed was measured in the wind tunnel test. When only the spire was installed, the reference wind speed of the numerical wind tunnel (at the same position as the wind tunnel test) was 27.56 m/s, and the average wind speed ratio at the reference wind speed position was 0.9187. Figure 4 shows an example of wind speed distribution visualization at the wind speed evaluation height. CFD analysis was conducted

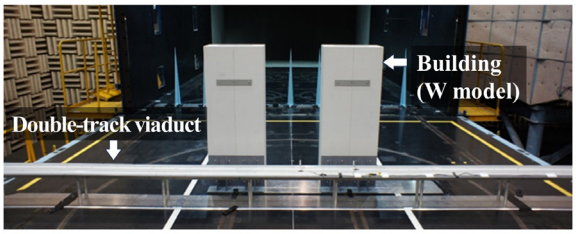

Fig. 1 View of two buildings (W model) and double-track viaduct models placed on the open test section floor

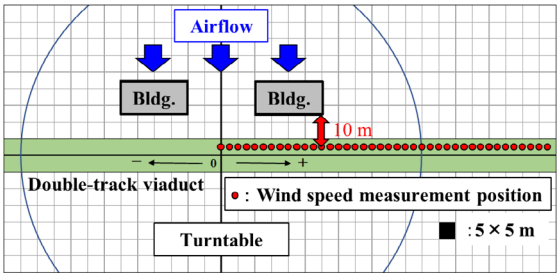

Fig. 2 Example of wind speed measurement position (W model, 90-degree angle)

for four cases tested in the wind tunnel (two types of S and W models, each with two wind direction angles of 90-degree and 70-degree). For wind speed evaluation, the average value over 3.3 seconds after the flow field reached a steady state was used.

2.4 Results of wind tunnel tests and CFD analysis

Wind speed increase rates on a double-track viaduct located downwind of a building were calculated using wind speed results obtained from wind tunnel tests and CFD analysis. For the wind tunnel test results, the wind speed increase rates were calculated by dividing the wind speeds obtained at each measurement position by the reference wind speed (26.71 m/s). For the CFD analysis results, the wind speed increase rates were calculated by dividing by the reference wind speed (27.56 m/s) in the numerical wind tunnel. The wind speed in the CFD analysis used the *x*-axis component (main flow direction component) shown in Fig. 3. The results are presented in Fig. 5. In Fig. 5, the red dots represent the wind tunnel test results, while the blue line shows the wind speed increase rate from the CFD analysis. From these results, we confirmed the tendency of wind speed to increase on the outside of the buildings and between the buildings. However, while the CFD analysis generally reproduced the increase in wind speed around the buildings, there was a discrepancy between the CFD results and the wind tunnel test results in the weak wind area downstream of the buildings. Specifically, the CFD analysis showed negative values (reverse flow) in this area, whereas the wind tunnel test results were positive. This difference is likely due to the hot-wire anemometer used to measure wind speed in the wind tunnel tests. The anemometer has directionality but cannot distinguish between forward and reverse flow. Therefore, we reanalyzed the CFD analysis results in Fig. 5(c) using the absolute wind speed values, similar to the wind speed sensor. The results are shown in Fig. 6. The black line in Fig. 6 shows the CFD analysis results reorganized with absolute wind speed values. The results are in good agreement with the wind tunnel test results, which are indicated by red circles. Additionally, references 12 and 13 suggest the presence of a reverse flow region in the wake of rectangular col-

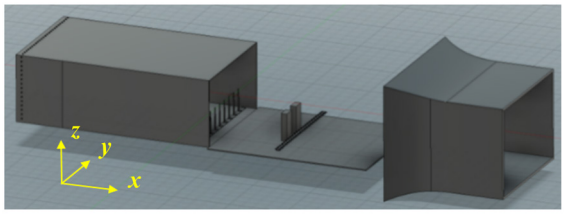

Fig. 3 Shape of created model

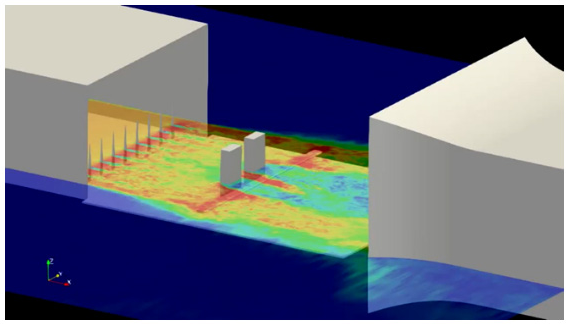

Fig. 4 Example of wind speed distribution visualization at the wind speed eva- luation height

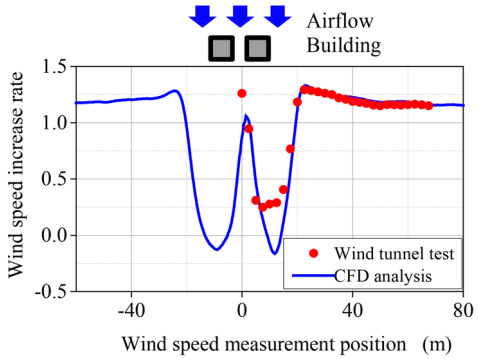

(a) S model, 90-degree angle

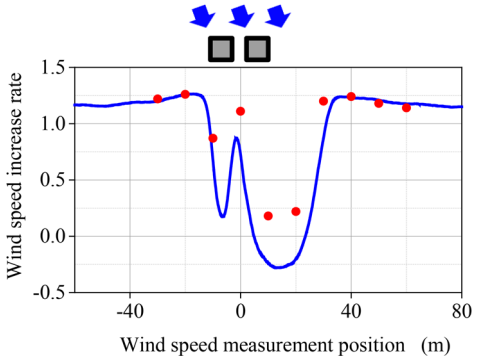

(b) S model, 70-degree angle

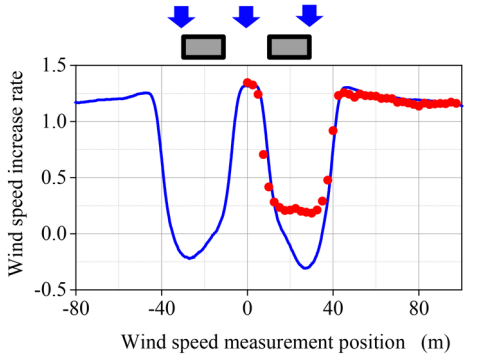

(c) W model, 90-degree angle

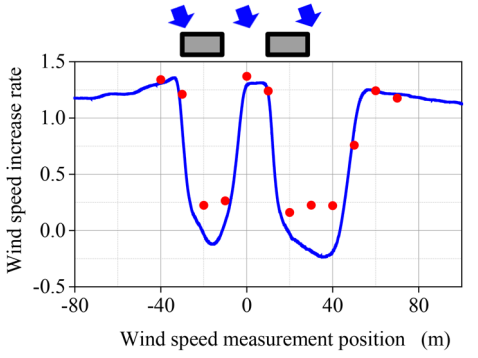

(d) W model, 70-degree angle

Fig. 5 Results of wind speed increase rates from wind tunnel tests and CFD analysis

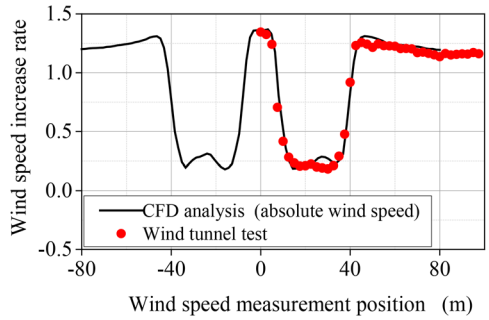

Fig. 6 Results of CFD analysis in Fig. 5(c) reprocessed with same absolute wind speed values as anemometer

umns. Based on these findings, it is highly likely that the CFD analysis more accurately represents the flow conditions in this weak wind area. On the other hand, there are also issues in the CFD analysis results. In the CFD analysis results for a wind direction angle of 90-degree, the wind speed increase rate is asymmetrical despite the building model and other conditions being symmetrical with respect to the wind tunnel center. This asymmetry may be due to errors resulting from insufficient averaging time in the analysis results. Furthermore, in the S model, there were instances where the CFD analysis could not accurately reproduce the increase in wind speed between buildings. This is presumed to be caused by the relatively coarse computational grid set for the building spacing in the S model. However, the range where these errors occurred is narrow, and their impact on the aerodynamic forces acting on vehicles is considered to be small. Therefore, the influence on vehicle behavior is expected to be limited. Detailed analysis of these errors and methods for improvement will be subjects for future research.

3. Evaluation of the impact of localized strong winds on vehicle running safety

3.1 Vehicle motion simulation model

We constructed a vehicle motion simulation model using Simpack, a multi-body dynamics analysis software. The vehicle model is shown in Fig. 7. The dimensions, masses, and spring constant of each element of the vehicle model were set to values of a typical commuter train. The bogie was modeled as a modern bolsterless type and included considerations for vertical and lateral stoppers to limit large displacements of the car body. The vehicle consists of rigid body elements with 6 degrees of freedom each for 1 car body, 2 bogie frames, 8 axle box supports, and 4 wheelsets, with each rigid body element connected by spring-damper systems. Additionally, lateral force and lift force due to crosswind were applied to the car body as external forces. To account for the distributed aerodynamic forces acting on the vehicle, points of force application on the car body were set at two locations along the rail in the longitudinal direction, and at two heights corresponding to the roof and floor levels. In this chapter, using this vehicle model, we calculate the wheel load reduction ratio on the windward side when spatially varying aerodynamic forces are applied to a vehicle running on a straight track. This allows us to evaluate the running safety of the vehicle under localized strong winds.

3.2 Effect of building-induced winds on the variation of windward wheel load

This section describes investigations into the impact of building-induced winds on vehicle running safety. We used the wind speed distribution of building-induced winds obtained in the previous chapter and the vehicle motion simulation model described in the previous section. Specifically, we calculated the variation in the windward wheel load when a typical commuter train runs on a straight track under the wind speed distribution (wind speed increase rate) for the W model with a wind direction of 90-degree angle, as shown in the previous chapter.

The estimated aerodynamic forces acting on the vehicle were determined as follows. First, based on the results of wind speed increase rate obtained from wind tunnel tests and CFD analysis shown in Fig. 5(c), the range of local wind speed increase and decrease due to the influence of the buildings was set to −80m to 80m at full-scale size. Next, to ensure that the rate of wind speed increase in areas unaffected by the building was 1, the results of CFD analysis were normalized using the wind tunnel test results from those areas. Figure 8 shows the wind speed increase rate. The blue line represents the results of the normalized CFD analysis. Based on these results, an approximation line (red line in Fig. 8) combining a linear

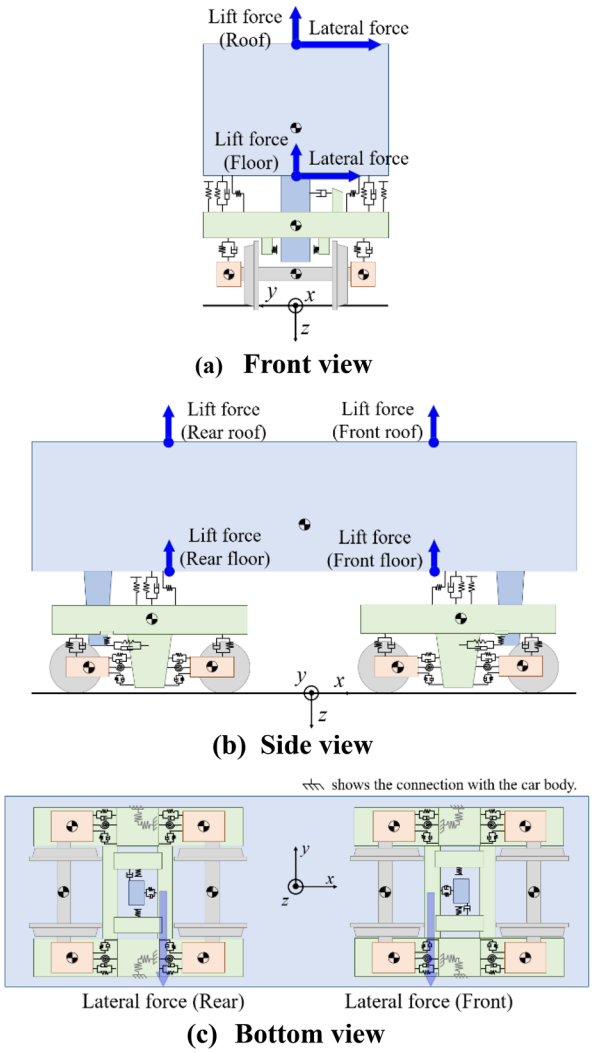

Fig. 7 Outline of vehicle model

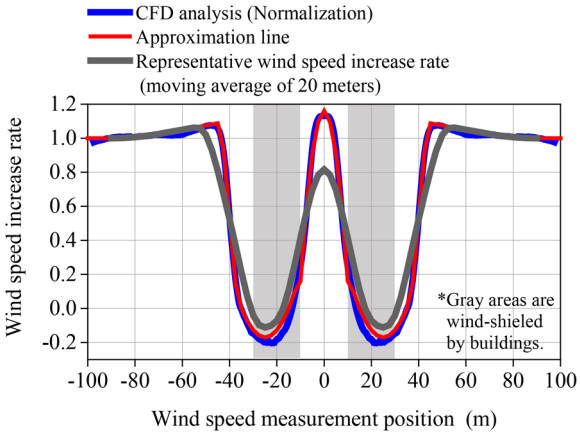

Fig. 8 Wind speed increase rate

Table 1 Aerodynamic coefficient used in the simulation

Commuter-type vehicle, Double-track viaduct Noise barrier: Height 1.28 m, Separation 2.48 m			
Wind angle	Lateral force coefficient	Lift force coefficient	Rolling moment coefficient
90°	1.19	0.35	−0.09
70°	1.04	0.50	−0.07
50°	0.77	0.54	−0.03
30°	0.41	0.29	−0.02

function and a quadratic function was determined as a format that can be easily incorporated into simulations. The approximation line was adjusted to be as close as possible to the normalized CFD analysis results. Finally, a moving average of 20 meters, which is the typical length of a commuter-type vehicle, was applied to this approximation line to obtain the representative wind speed increase rate (gray line in Fig. 8). For areas beyond the building's influence (areas exceeding ±80 m), we assumed a wind speed of 25 m/s. The representative wind speed at each measurement location was then determined by multiplying the assumed wind speed by the representative wind speed increase rate. From Fig. 8, it can be observed that the representative wind speed increase rate reaches a maximum of approximately 1.1 in this case, with higher values occurring on the outer sides of adjacent buildings. Next, regarding the aerodynamic force coefficients required to calculate the aerodynamic forces acting on vehicles, we considered that building-induced wind problems primarily occur in urban areas. Additionally, double-track viaducts commonly have noise barriers and other similar structures. Therefore, based on references 14 and 15, we assumed the values shown in Table 1 for the aerodynamic coefficients. The vehicle running speeds were set at 30 km/h, 60 km/h, 90 km/h, and 120 km/h. The aerodynamic coefficients were sequentially calculated from the relative wind angles obtained from each running speed and representative wind speed. The estimated aerodynamic forces were then calculated using the relative wind speed. As a reference, Fig. 9 shows the estimated aerodynamic forces calculated for vehicle running speeds of 30 km/h and 120 km/h. The lateral forces and lift forces acting on the roof and floor positions were distributed based on the rolling moment coefficient. Additionally, it was assumed that half of the estimated aerodynamic force acted simultaneously and equally on the front and rear positions of the vehicle.

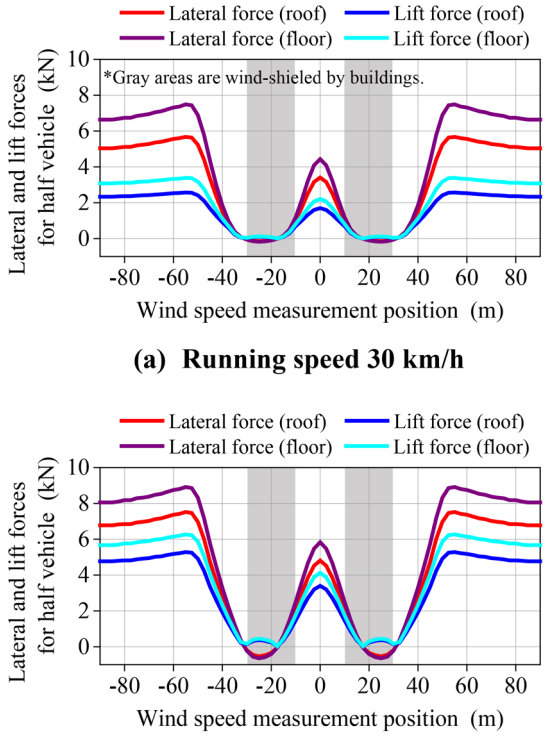

Fig. 9 Estimated aerodynamic forces

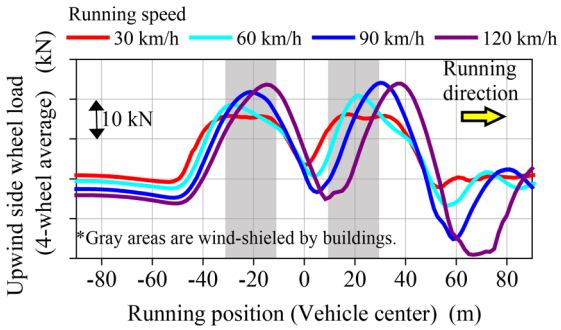

Fig. 10 Variation of windward side wheel load

Using the estimated aerodynamic forces and the vehicle motion simulation model described above, we calculated the fluctuation of the windward wheel load (average load of 4 wheels) for a commuter-type vehicle running at various speeds (30 km/h, 60 km/h, 90 km/h, and 120 km/h). The results are shown in Fig. 10. From Fig. 10, it can be observed that the windward wheel load fluctuates due to the influence of building-induced wind. In particular, there is a tendency for the wheel load to decrease when the vehicle enters the strong wind area outside the building from the weak wind area downstream of the building (near the running position of 60 m). It was found that the wheel load decreases more significantly when the vehicle is running at high speed and suddenly encounters strong winds. Regarding the localized wind between buildings, the impact on wheel load reduction was small when the spacing between adjacent buildings was approximately one vehicle length (20 m).

3.3 Parameter study on aerodynamic force changes and wheel load reduction ratio

In the previous section, we confirmed that a significant decrease in wheel load occurs when a high-speed vehicle suddenly encounters strong winds. Therefore, in this section, we conducted a parametric study on the relationship between changes in aerodynamic forces and the wheel load reduction ratios. Specifically, using the vehicle motion simulation model to focus on a typical commuter-type vehicle, we examined the variation in the wheel load reduction ratio when the rise time and rise range of the aerodynamic force are changed. Figure 11 shows the set range in the aerodynamic forces (for half a vehicle). As can be seen in Fig. 11, the lateral force and lift force in the strong wind area were fixed at 15.0 kN and 10.0 kN respectively, while the lateral force and lift force in the weak wind area were varied. In the weak area, the combinations of lateral force and lift force were set as follows: (lateral force (kN), lift force (kN)) = (0, 0), (0.6, 0.4), (2.4, 1.6), (5.4, 3.6), (9.6, 6.4). These values were determined based on the estimated aerodynamic forces from the previous section, assuming wind speeds of 25 m/s for the strong wind area and 0 m/s, 5 m/s, 10 m/s, 15 m/s, and 20 m/s for the weak wind area. The forces acting on the roof and floor positions were distributed assuming a wind pressure center height of 2.2 m. Considering severe localized strong winds conditions, it was assumed that the wind force would increase over a range of 10 m for the rise time. With a 20 m long vehicle running at speeds between 10 km/h and 120 km/h through this range, the rise times were set between 10.8 seconds and 0.9 seconds. It should be noted that shorter rise times correspond to situations in which the vehicle suddenly encounters strong winds.

Figure 12 shows an example of the variation in the wheel load reduction ratio on the windward side calculated under the above assumptions. In this section, we focus on the difference between the maximum wheel load reduction ratio observed when the vehicle enters a strong wind area from a weak wind area, and the wheel load reduction ratio after the vehicle's vibration has stabilized in the strong wind area (see Fig. 12). It should be noted that the wheel load reduction ratio, once the vehicle's vibration has stabilized, is almost equal to the value obtained from the RTRI detailed equation [1], which is used to evaluate the critical wind speed for overturning. Figure 13 summarizes the effects of changes in the rise time and rise range of aerodynamic forces on the variations in the wheel load reduction ratio. In Fig. 13, the horizontal axis represents the rise range, the vertical axis represents the rise time, and the color map shows the difference in wheel load reduction ratio variation in 2.0 % increments. As can be seen in Fig. 13, the wheel load reduction ratio was found to increase when the rise time of the aerodynamic forces acting on the vehicle was shorter than about 2 seconds. This tendency is particularly pronounced when the rise range of the aerodynamic force is large and the rise time is short. It should be noted that these results may vary depending on the vehicle body shape (aerodynamic characteristics) and vehicle specifications. Therefore, further studies are necessary to consider vehicles other than the general commuter train examined in this study.

Based on these results, it can be concluded that effective countermeasures against localized strong winds include implementing speed restrictions to ensure that the rise time of aerodynamic forces is at least 2 seconds and installing windbreak fences that gradually change in height or solidity. These measures are considered to be effective in mitigating the impact of localized strong winds on railway vehicles.

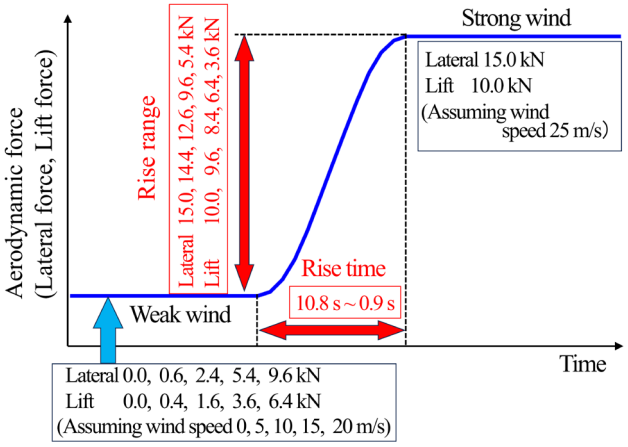

Fig. 11 Aerodynamic force variation

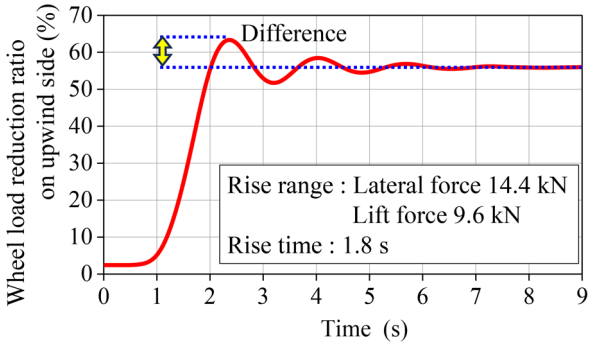

Fig. 12 Changes in the wheel load reduction ratio on windward side, and method for calculating difference

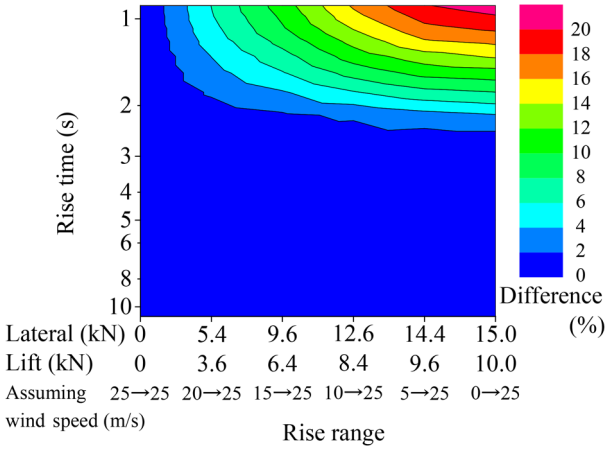

Fig. 13 Result of effects of aerodynamic force rise time and rise range on difference in wheel load reduction ratio

4. Conclusions

In this study, we aimed to provide insights that contribute to the development of operational regulations designed to enhance transport stability while ensuring running safety. We analyzed how vehicles behave in response to localized strong winds using numerical analysis. Specifically, we focused on building-induced winds resulting from the proximity of the two buildings. We conducted wind

tunnel tests and CFD analysis to investigate the effects of short-term fluctuations in aerodynamic forces on vehicle behavior. The results obtained are as follows:

1) Wind tunnel tests and CFD analysis using the numerical wind tunnel developed by the Railway Technical Research Institute were conducted to determine the wind speed increase rate on a double-track viaduct located downstream of buildings. The results confirmed an increase in wind speeds on the outer sides of buildings and between them. Furthermore, the results from both methods showed good quantitative agreement, demonstrating that CFD analysis can accurately reproduce the speed distribution of building-induced winds.
2) Using a vehicle motion simulation model that incorporates lateral force and lift force due to crosswinds acting on the vehicle body, we calculated the variation in wheel load on the windward side. Aerodynamic forces were estimated from the wind speed distribution obtained through CFD analysis and applied to a moving commuter-type vehicle. The results showed that the wheel load tended to decrease at the point where the vehicle enters a strong wind area outside the buildings from a weak wind area in the lee of the buildings. It was found that the wheel load decreased especially significantly when the vehicle was running at high speed and suddenly encountered strong winds.
3) We calculated the difference in wheel load reduction ratios using the model mentioned in the previous item 2) by varying the rise time and rise range of the aerodynamic forces. We then organized the conditions requiring attention from a running safety perspective due to spatial changes in aerodynamic forces. The results showed that the wheel load reduction ratio increases when the rise time of the aerodynamic forces acting on the vehicle is less than about 2 seconds. These findings suggest that effective countermeasures against localized strong winds include speed regulations and installing gradual windbreak fences, which ensure that the rise time of aerodynamic forces is 2 seconds or longer.

References

[1] Hibino, Y. and Ishida, H., "Static analysis on railway vehicle overturning under crosswind," *RTRI Report*, Vol. 17, No. 4, pp. 39-44, 2003 (in Japanese).
[2] Kunieda, M., "Theoretical study on the mechanics of overturn of railway rolling stock," *Railway Technical Research Report*, No. 793, 1972 (in Japanese).
[3] Aircraft and railway accidents investigation commission, East Japan Railway Company Uetsu Line train derailment accident between Sunagoe station and Kita-Amarume station, *Railway accident investigation report*, RA2008-4, 2008 (in Japanese).
[4] Nagumo, Y., Ichiki, M. and Misu, Y., "Safety assessment of train operation applying a new method for operation control under strong winds," *JR EAST Technical Review*, No. 66, pp. 25-33, 2021 (in Japanese).
[5] Hibino, Y., Kanemoto, H., Shimomura, T. and Tanifuji, K., "Construction and verification of dynamic analysis model for evaluating dynamic behavior of railway vehicle being subjected to crosswind," *Transactions of the Japan Society of Mechanical Engineers*, *Series C*, Vol. 76, No. 766, pp. 1396-1405, 2010 (in Japanese).
[6] Hibino, Y., Kanemoto, H., Shimomura, T. and Tanifuji, K., "Safety evaluation of railway vehicle against crosswind applying a full-vehicle simulation model," *Transactions of the Japan Society of Mechanical Engineers*, *Series C*, Vol. 76, No. 771, pp. 3066-3076, 2010 (in Japanese).
[7] Gautier, P. -E., "Strong wind risks in railways: the DEUFRAKO crosswind program," *Proceedings of the World Congress on Railway Research (WCRR2003)*, pp. 463-474, 2003.
[8] Kanemoto, H. and Hibino, Y., "Method for estimating lateral carbody vibration acceleration used for safety evaluation of railway vehicles against crosswind," *QR of RTRI*, Vol. 65, No. 2, pp. 89-96, 2024.
[9] Hibino, Y., Kanemoto, H. and Sakuma, Y., "Dynamic response of a moving vehicle to a sudden gust of wind," *RTRI Report*, Vol. 27, No. 12, pp. 23-28, 2013 (in Japanese).
[10] Ishihara, T., Zhang, D. and Nagumo, Y., "Numerical study of dynamic response of railway vehicles under tunnel exit winds using multibody dynamic simulations," *Journal of Wind Engineering & Industrial Aerodynamics*, 211, 104556, 2021.
[11] Nakade, K., Ido, A., Abe, T. and Inoue, T., "Development of a numerical wind tunnel that simulates a large-scale low-noise wind tunnel," *Proceedings of the TRANSLOG2022*, PS2-12, 2022 (in Japanese).
[12] Tamura, T., "Flow past a square and a rectangular cylinder – Turbulence effects on its aerodynamics," *Journal of Japan Society of Fluid Mechanics*, 22, pp. 7-13, 2003 (in Japanese).
[13] Nagahisa, T., Okajima, A. and Shibata, R., "Unsteady aerodynamic forces on a vehicle model passing in a wake (experiments)," *Transactions of the Japan Society of Mechanical Engineers*, *Series B*, Vol. 53, No. 485, pp. 40-48, 1987 (in Japanese).
[14] Tanemoto, K., Suzuki, M., Saitou, H. and Ido, A., "Results of wind tunnel tests for aerodynamic coefficients of railway vehicle," *RTRI Report*, Vol. 27, No. 1, pp. 47-50, 2013 (in Japanese).
[15] Otobe, T., Suzuki, M. and Noguchi, Y., "Wind protection effect by the wall for a vehicle with strong wind," *RTRI Report*, Vol. 31, No. 9, pp. 5-10, 2017 (in Japanese).

Authors

Hiroyuki KANEMOTO, Ph.D.
Senior Researcher, Vehicle Mechanics Laboratory, Railway Dynamics Division
Research Areas: Vehicle Dynamics, Cross Wind Safety

Yu HIBINO, Ph.D.
Principal Researcher, Research and Development Promotion Division (Former)
Research Areas: Vehicle Dynamics, Cross Wind Safety

Immediacy and Accuracy of the Earthquake Early Warning Method Based on the P-wave Threshold Exceedance: Application to the 2016 Kumamoto Earthquake Sequence

Misa MORIWAKI
Seismic Data Analysis Laboratory, Center for Railway Earthquake Engineering Research

Seiji TSUNO
Institute of Science Tokyo

Masahiro KORENAGA
Seismic Data Analysis Laboratory, Center for Railway Earthquake Engineering Research

Katsutomo NIWA
JR Central Consultants Co., Ltd

Earthquake Early Warning (EEW) systems are essential for ensuring the safety of trains in Japanese railways during earthquakes. The conventional warning method takes over one second to issue alerts, which is often too long for events near the fault plane. We propose an on-site EEW method using the amplitude ratios of S-waves to P-waves, reflecting local ground characteristics. This method enables real-time prediction of S-waves through simple arithmetic, which does not depend on estimating epicentral distance. When applied to the main shock of the 2016 Kumamoto Earthquake, the method issued alerts within one second and accurate S-wave amplitude predictions, with a logarithmic standard deviation of 0.308. This demonstrates its effectiveness in ensuring railway safety.

***Key words*:** *earthquake early warnings, amplitude ratios of S-wave to P-wave, real-time, the 2016 Kumamoto Earthquake*

1. Introduction

In Japanese railways, Earthquake Early Warning (EEW) systems are operated to stop trains and ensure safety during earthquakes. The systems issue warnings prior to strong shaking based on seismic motion data recorded at seismic stations installed along the railway at 5-40 km intervals, as well as at densely distributed observation points across Japan. In the current EEW systems, the on-site P-wave warning method is employed. This method predicts the intensity of shaking along the railway and determines the need to issue a warning or not using magnitude [1] and epicentral distance estimates [2] derived from seismic data recorded for at least one second immediately after the P-wave arrival. The on-site S-wave warning method is also employed and is issued when the intensity of the S-wave exceeds a specified threshold. Therefore, it takes at least one second from P-wave detection for the system to issue a warning. As a result, especially near the fault, it is often impossible to alert running trains before strong shaking reaches the tracks.

Recently, a new on-site P-wave method using site-specific ratios of S-wave to P-wave has been developed [3]. This new method improves warning speed because it predicts the S-wave directly from the P-wave, without estimating magnitude or epicentral distance. Furthermore, since it can incorporate site-specific ground amplification characteristics into S-wave predictions, it is also expected to improve warning accuracy. This method is known as the "P-wave threshold exceedance method." Tsuno et al. (2024) applied this method to the 2016 Kumamoto earthquake sequence and quantitatively examined its applicability to ground motions near the fault using spectral ratios and peak ground acceleration (PGA) [4]. In this study, we evaluated the immediacy and accuracy of warnings when applying this method to the 2016 Kumamoto earthquake sequence, with a view toward its practical implementation for railways.

2. Data

Strong motion data of the foreshock, main shock, and aftershocks of the 2016 Kumamoto earthquake were used. These data were obtained from the K-NET and KiK-net strong-motion networks operated by the National Research Institute for Earth Science and Disaster Resilience (NIED) [5]. The hypocenter locations and magnitudes used in this study are shown in Fig. 1.

3. P-wave threshold exceedance method

Figure 2 illustrates a schematic of the P-wave threshold exceedance method. In this method, the S-wave is predicted by multiplying the P-wave observed at a seismic station by the site-specific ratio of S-wave to P-wave. This approach allows warnings to be issued more quickly than conventional methods.

This method is formulated as described in Ref. [3].

$$\log O_s^S(\omega) = \log O_s^P(\omega) + b(\omega) \quad (1)$$

$$b(\omega) = a_1(\omega) - a_2(\omega) + a_3(\omega) \quad (2)$$

Here, ω is the angular frequency. $O_s^S(\omega)$ represents the Fourier spectrum of the S-wave at the ground, and $O_s^P(\omega)$ represents the Fourier spectrum of the P-wave at the ground surface. In addition, $a_1(\omega)$ incorporates the source and path effects, while $a_2(\omega)$ and $a_3(\omega)$ include the site effects of P-wave and S-wave, respectively. Miyakoshi and Tsuno (2015) demonstrated that the effects of the source

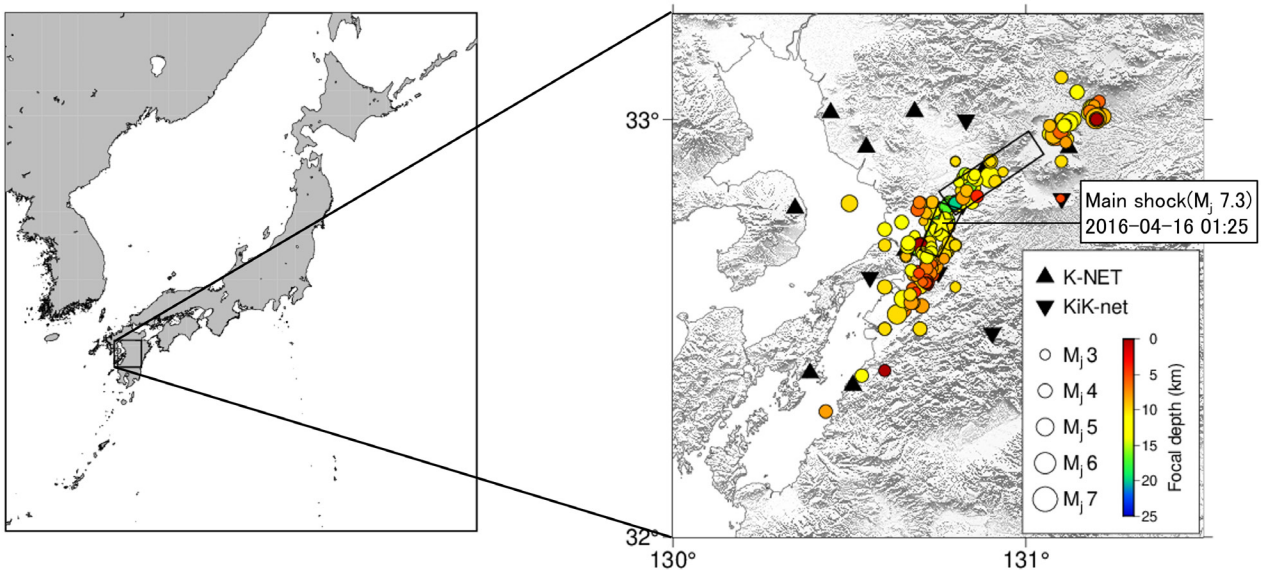

Fig. 1 Locations of seismic stations and the hypocenters with magnitudes used in this study.

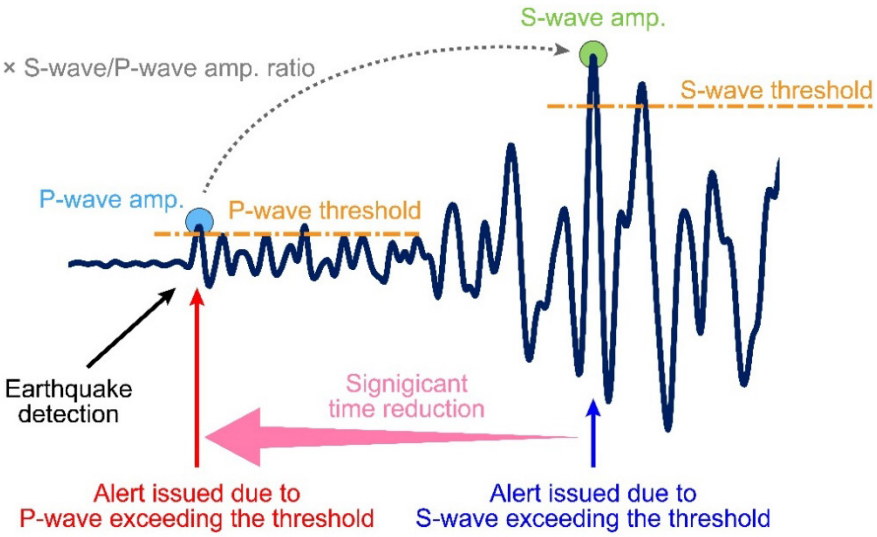

Fig. 2 Schematic of the P-wave threshold exceedance method

and propagation path on the Fourier spectrum ratio of S-wave to P-wave are sufficiently small by investigating the relationship between bedrock P-waves and surface S-waves [6]. In this study, equations (1) and (2) are applied in the time domain, and the analysis is conducted using the PGA.

4. Amplitude ratio of S-wave to P-wave

The site-specific amplitude ratios of S-wave to P-wave were calculated using the strong motion data of the 2016 Kumamoto earthquake sequence. The procedure is as follows.

Step1: The arrival times of the P-wave and S-wave were visually identified for the strong motion data.

Step2: Time windows of 10.24 seconds were extracted based on the P-wave arrival on the UD component and the S-wave arrivals on the NS and EW components. If the interval between the P- and S-wave arrivals was shorter than 10.24 seconds, the window was truncated just before the S-wave arrival to avoid contamination of the P-wave portion by the S-wave.

Step3: PGA of the P-wave was calculated using the data extracted from the UD component.

Step4: PGAs of the S-wave were calculated using the data extracted from the NS and EW components. The S-wave PGA was then obtained as the average of the PGAs from the two components.

Step5: The amplitude ratios of S-wave to P-wave were calculated by dividing the PGA of the S-wave by that of the P-wave.

Step6: At each site, the amplitude of the S-wave to P-wave were calculated for all data following steps 1-5. The logarithmic mean of these ratios was then taken as the final amplitude ratio of S-wave to P-wave for the site.

Figure 3 shows the amplitude ratios of S-wave to P-wave at each seismic station. In this area, the amplitude ratios of S-wave to P-wave in the PGAs differ by a factor of several across different sites. This result shows the importance of evaluating the site-specif-

ic amplification characteristics.

5. Application to the 2016 Kumamoto earthquake

5.1 Immediacy

The proposed method was applied to the main shock data of the 2016 Kumamoto earthquake to evaluate the immediacy of warnings. Figure 4 illustrates the processing procedure of the method using the KMMH16 station as an example. After the detection of the P-wave, the method continuously multiplies the PGA of the UD component of the P-wave by the S-wave to P-wave amplitude ratio (1.87 at KMMH16) in real time to predict the PGA of the upcoming S-wave—horizontal components. Here, assuming that a warning is issued when the predicted S-wave PGA exceeds 80 cm/s^2, the warning would be issued 0.64 seconds after the detection of the P-wave. Namely, the warning can be issued within less than one second after the detection of the P-wave, which is considerably faster than conventional S-wave or P-wave warnings. This result demonstrates the immediacy of warnings achieved with the proposed method.

5.2 Accuracy

The proposed method was applied to the mainshock data of the 2016 Kumamoto earthquake at each seismic station to predict the PGA of the S-wave from the detection of the P-wave up to just before the arrival of the S-wave. Figure 5 shows the comparison between the predicted S-wave PGA obtained by the proposed method and the observed S-wave PGA. The logarithmic standard deviation (LSD) of the residuals between observed and predicted S-wave PGA was 0.308, indicating that the method can accurately estimate the intensity of the S-wave prior to its arrival. Table 1 shows the warning issuance results. Assuming that a warning is issued when the predicted S-wave PGA exceeds 80 cm/s^2, out of the 16 sites, warnings were correctly issued at 12 sites, overestimation occurred at 0 sites, and underestimation occurred at 4 sites. In contrast, the LSD for the conventional P-wave warning (C-Δ method) was 0.433, with warnings correctly issued at 13 sites, overestimation at 1 site, and underestimation at 2 sites. These results indicate that the high accuracy of warnings using the P-wave threshold exceedance method is comparable to that of the C-Δ method.

6. Discussion

The proposed method, as well as the conventional P-wave and S-wave warning methods, were applied to the main shock data of the 2016 Kumamoto earthquake to compare the time from P-wave detection to warning issuance. The results are shown in Fig. 6. The circles shown next to each observation site, when filled with blue, red, or green, indicate that a warning has been issued by the P-wave

Table 1 Warning issuance results for the main shock of the 2016 Kumamoto earthquake.

Method	Correct (issued)	Correct (not issued)	Over est.	Under est.
Proposed	11	1	0	4
C-Δ	13	0	1	2

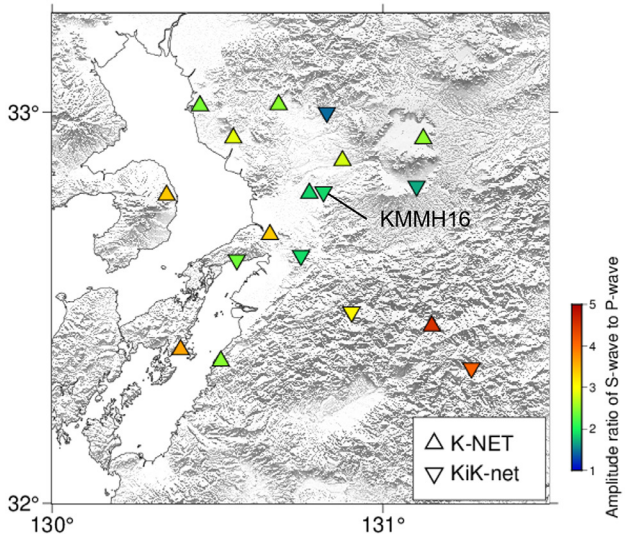

Fig. 3 The amplitude ratio of S-wave to P-wave at each site

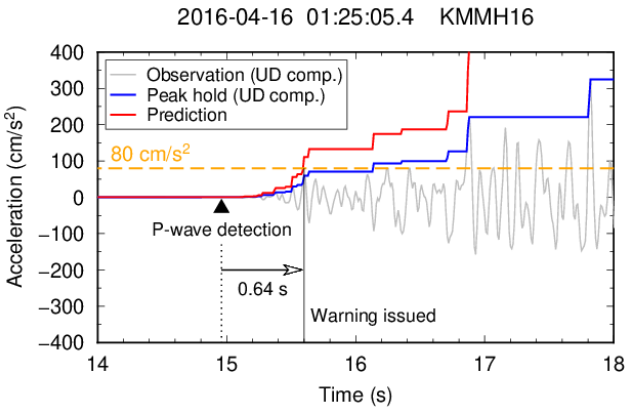

Fig. 4 Application of the proposed method to the main shock of the 2016 Kumamoto earthquake at the KMMH16 station

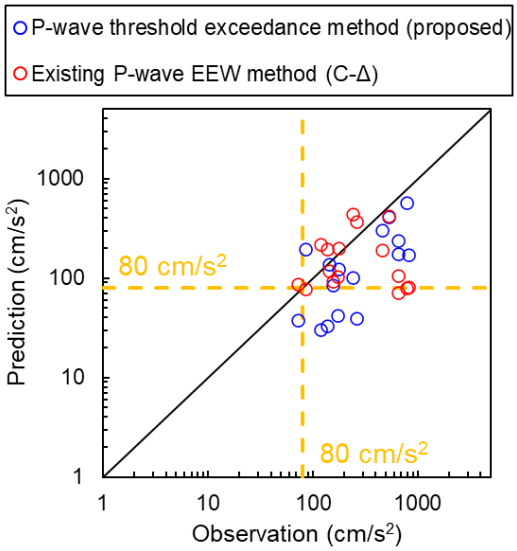

Fig. 5 Relationship between observed and predicted S-wave PGA for the main shock of the 2016 Kumamoto earthquake

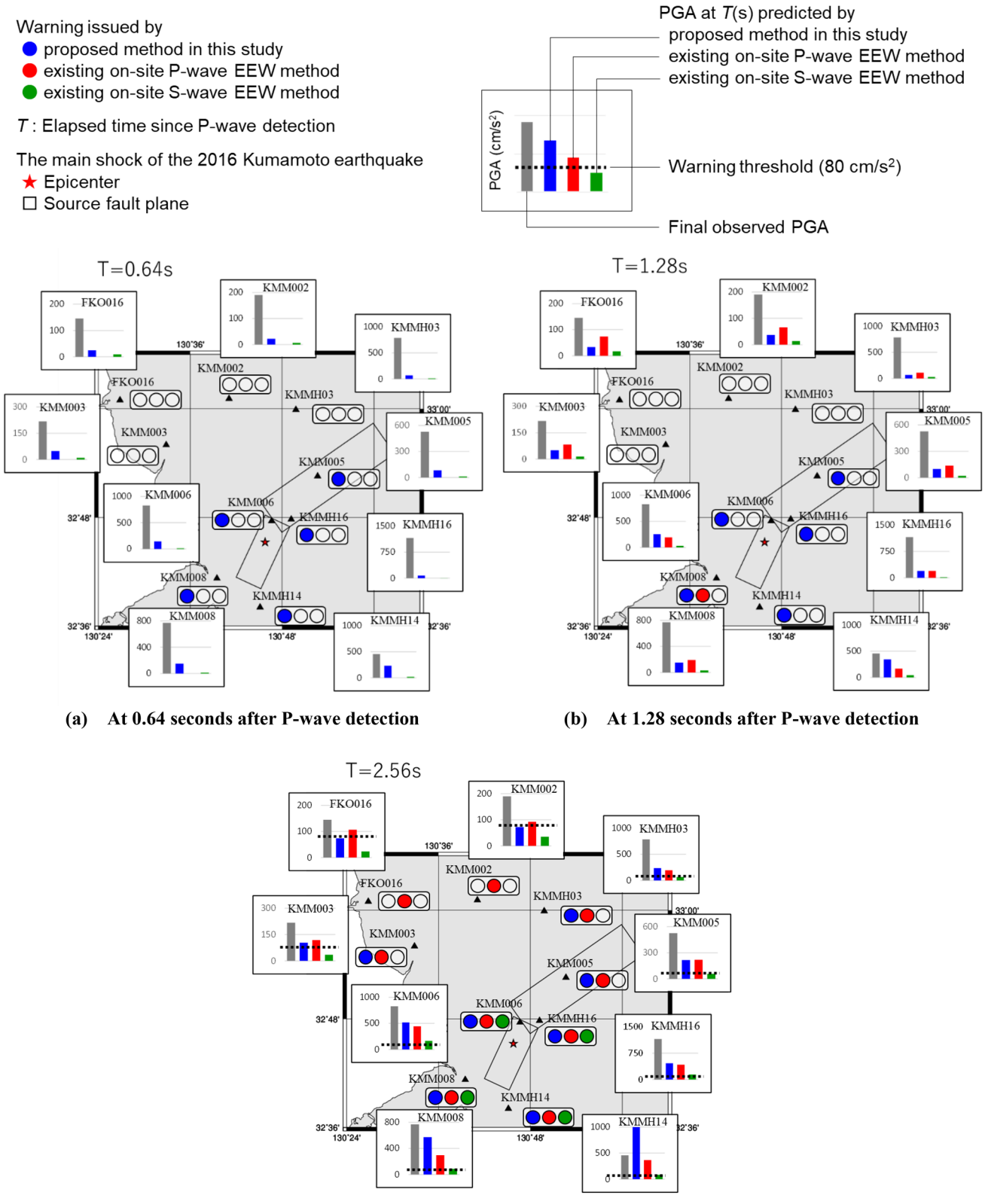

(a) At 0.64 seconds after P-wave detection

(b) At 1.28 seconds after P-wave detection

(c) At 2.56 seconds after P-wave detection

Fig. 6 Comparison of warning issuance for the main shock of the 2016 Kumamoto earthquake

threshold exceedance (proposed) method, the conventional P-wave warning (C-Δ) method, or the conventional S-wave warning method, respectively. At 0.64 and 1.28 seconds after P-wave detection, warnings issued by the P-wave threshold exceedance method are observed mainly near the source fault. On the other hand, at 2.56 seconds after P-wave detection, both the proposed warning and the

conventional P-wave warning have been issued near the source fault, while only the conventional P-wave warning issued at locations farther from the fault. These results confirm that the proposed method is capable of issuing warnings at the earliest near the source faults. Furthermore, it was verified that combining the proposed method with conventional warning methods enables stable warning issuance over a wide area.

7. Conclusions

In this study, the proposed on-site P-wave warning method was applied to the 2016 Kumamoto earthquake data to evaluate the promptness and accuracy of warning issuance for inland earthquakes occurring near railway lines. Site-specific amplitude ratios of S-wave to P-wave at each seismic station were calculated and applied to predict S-wave PGA immediately after P-wave detection. The results demonstrated that the proposed method could issue warnings earliest near the source faults, and when combined with conventional P- and S-wave warning methods, enable stable warning issuance over a wide area. Furthermore, the accuracy of predicted S-wave PGA was generally comparable to that of existing methods. These findings indicate that the proposed method is effective for practical implementation in railway EEW systems.

Acknowledgment

In this study, strong motion data from the K-NET and KiK-net operated by the National Research Institute for Earth Science and Disaster Resilience (NIED) were used. The hypocenter locations and magnitudes of the 2016 Kumamoto earthquake sequence were obtained from data publicly released by the Japan Meteorological Agency. The location of the source fault for the main shock of the 2016 Kumamoto earthquake was taken from Asano and Iwata (2016) [7]. Some of the figures were created using GMT [8].

References

[1] Nakamura, Y., "On the Urgent Earthquake Detection and Alarm System (UrEDAS)," *proceedings of Ninth World Conference on Earthquake Engineering,* Vol. 7, pp. 673-678, August 1988.

[2] Odaka, T., Ashiya, K., Tsukada, S., Sato, S., Ohtake, K. and Nozaka, D., "A New Method of Quickly Estimating Epicentral Distance and Magnitude from a Single Seismic Record," *Bulletin of the Seismological Society of America*, Vol. 93, No. 1, pp. 526-532, February 2003.
DOI: https://doi.org/10.1785/0120020008

[3] Tsuno, S., "Applicability of On-Site P-Wave Earthquake Early Warning to Seismic Data Observed During the 2011 Off the Pacific Coast of Tohoku Earthquake, Japan," Frontiers in Earth Science, Vol. 9, 681199, November 2021.
DOI: https://doi.org/10.3389/feart.2021.681199

[4] Tsuno, S., Niwa, K., Korenaga, M., Yamanaka, H., Chimoto, K., Miyake, H. and Yamada, N., "Application of the On-site P-wave Earthquake Early Warning Method Based on Site-specific Ratios of S-waves to P-waves to the 2016 Kumamoto Earthquake Sequence, Japan," *Earth, Planets and Space,* Vol. 76, No. 1, 32, February 2024.
DOI: https://doi.org/10.1186/s40623-024-01968-y

[5] National Research Institute for Earth Science and Disaster Resilience, NIED K-NET, KiK-net, 2019.
DOI: https://doi.org/10.17598/nied.0004

[6] Miyakoshi, H. and Tsuno, S., "Influence of the Source, Path, and Site Effects on the Relationship between P-Waves at the Seismic Bedrock and S-Waves on the Ground Surface," Journal of the Seismological Society of Japan, 2nd ser., Vol. 68, No. 4, pp. 91-105, April 2015 (in Japanese).
DOI: https://doi.org/10.4294/zisin.68.91

[7] Asano, K. and Iwata, T., "Source Rupture Processes of the foreshock and main shock in the 2016 Kumamoto earthquake sequence estimated from the kinematic waveform inversion of strong motion data," *Earth, Planets and Space,* Vol. 68, No. 1, 147, August 2016.
DOI: https://doi.org/10.1186/s40623-016-0519-9

[8] Wessel, P., Luis, J. F., Uieda, L., Scharroo, R., Wobbe, F., Smith, W. H. F. and Tian, D. "The Generic Mapping Tools Version 6," *Geochemistry, Geophysics, Geosystems,* Vol. 20, No. 11, pp. 5556-5564, September 2019.
DOI: https://doi.org/10.1029/2019GC008515

Authors

Misa MORIWAKI
Senior Researcher, Seismic Data Analysis Laboratory, Center for Railway Earthquake Engineering Research
Research Areas: Earthquake Early Warning, Historical Earthquake

Seiji TSUNO, Ph.D.
Associate Professor, School of Environment and Society, Institute of Science Tokyo
Research Areas: Earthquake Engineering

Masahiro KORENAGA
Senior Chief Researcher, Head of Seismic Data Analysis Laboratory, Center for Railway Earthquake Engineering Research
Research Areas: Earthquake Early Warning, Earthquake Engineering

Katsutomo NIWA
Technical Manager, JR Central Consultants Co., Ltd
Research Areas: Earthquake Early Warning, Earthquake Engineering

Derailment Detection for Wagons Using Mechanical Contact Sensors

Shogo MAMADA **Tatsuya OTA**
Vibration-Isolating Materials Laboratory, Materials Technology Division

Kohei MIYAHARA
Vehicle Dynamics Laboratory, Vehicle Technology Division

Kazuto KOSUGI
Vehicle Dynamics Laboratory, Vehicle Technology Division (Former)

In long freight trains, if a wagon far from the locomotive derails, detection of the derailment may be delayed, potentially allowing the train to continue running with the derailed wagon. We investigated a derailment detection method using mechanical contact sensors to enable early detection of wagon derailments. In this study, the installation position of the contact sensors was selected based on results from past derailment investigations and simulation results. Derailment detection tests were then conducted derailing a bogie equipped with contact sensors on an actual track. These tests confirmed that the contact sensors can detect derailment immediately after it occurs.

***Key words*:** *freight wagon, derailment, mechanical contact sensors, derailment detection test, actual track*

1. Introduction

On freight trains operating as long formations, detection of a derailed wagon far from the locomotive may be delayed [1]. There is then a risk of further damage to ground facilities such as sleepers and rail fastening devices, if the train continues to run with the derailed wagon. Methods for early detection of derailed wagons are thus essential [1]. Many studies have examined the application of condition monitoring systems that use vibration acceleration sensors and angular velocity sensors mounted on passenger cars to detect derailments. Some of these systems are already in service [2, 3, 4]. These methods set thresholds for vibration acceleration and angular velocity. Condition monitoring devices installed on vehicles detect breaches of these thresholds. This distinguishes normal operation from derailment. The application of similar methods to wagons is also being considered [5, 6], but faces the following challenges:

- Wagons exhibit high stiffness in both primary and secondary springs, making them susceptible to changes in track input caused by variations in running speed. Furthermore, the operating conditions of wagons vary significantly due to differences in load weight and the variety of track sections. Setting threshold values for vibration acceleration and angular velocity is thus a problem.
- Vibration acceleration in wagons is greater than in passenger cars. This makes it difficult to distinguish between loading/unloading operations and low-speed derailments.
- Stable power supply to wagons is problematic, so sensors and detection devices that can operate using small batteries or similar power sources are required.
- Due to the large number of wagons, it is impractical to apply expensive sensors and detection devices to each vehicle.

Therefore, we investigated a method for detecting derailments of wagons by installing mechanical contact sensors, such as switches, on the bogies. Details of the contact sensors are explained Section 3 of this paper. Typically, the sensor changes from an electrically conductive state or non-conductive state to the opposite state upon contact with an object. The reasons for considering the application of contact sensors are as follows:

- Previous findings suggest that in the event of a derailment, certain bogie parts come into contact with other components within the bogie or with ground-level equipment, such as rails [1, 7].
- In the event of derailment, electrically reversed states (conductive and non-conductive) can be detected and determined without the complex threshold calculations required when using vibration acceleration sensors or angular velocity sensors. This simplifies the process of detecting and configuring the detection device, making it more cost-effective.

This report describes the process of selecting locations to install contact sensors, as well as how to apply them. It also presents the results of tests conducted on wagons equipped with contact sensors and assess their derailment detection performance (hereinafter, referred to as 'derailment detection test').

2. Selection of locations to install contact sensors

2.1 Derailment patterns assuming detection by contact sensors

In order to apply contact sensors to derailment detection, the vehicle behavior during derailment must be examined and modeled. This enables the selection of locations where contact may only occur during derailment, allowing contact sensors to be installed at these specific points. However, patterns observed in past wagon derailment accidents include wheel-climbing derailments in curves, gauge expansion-induced derailments within the track gauge, and wheel-climbing derailments onto turnout leads or ice/snow. It is difficult to identify installation locations capable of detecting all possible derailment patterns when considering these scenarios.

Therefore, this study focuses on the detection of "flange climb derailments in curved sections." This type of derailment occurs on main lines where it is unlikely outsider observers would be able to see it. Furthermore, these derailments do not involve factors that complicate modeling of wheel-rail contact conditions, such as turnouts or ice/snow.

2.2 Study on the falling behavior of wheels due to derailment

During a derailment caused by climbing onto the rail during curved running, the lateral pressure on the outer side wheel of the first axle, which generally has the largest attack angle, increases. This causes the wheel to climb onto the rail, resulting in derailment [2, 8, 9]. Therefore, to identify locations where contact sensors could be installed to immediately detect derailment, it is necessary to examine how the vehicle behaves when the first axle derails. Consequently, we examined how the vehicle behaved using a mechanical model from the moment the first axle derailed and fell off the rail, to the moment it made contact with the ground surface. We identified potential contact points based on the proximity of various components within the bogie.

Firstly, we calculated the geometric contact positions between the wheel and rail when the outer-side wheel climbs, to specifically define derailment conditions for the first axle in the mechanical model. This was done using the wheel-rail contact characteristic calculation method developed by Adachi et al [10]. This allowed us to examine how the wheel-axle assembly derails. The results showed that the wheels on the inner-track derail and fall before the wheels on the outer-track climb onto the rail. Therefore, when analyzing vehicle behavior during wheel fall using the mechanical model, we assume that only the wheels on one side of the axle fall.

2.3 Mechanical model

Figure 1 shows the exterior of the bogie and the names of its component examined in the theoretical study. Figure 2 shows the mechanical model of the half-car body used in the study. In the mechanical model, it was assumed that during curved running on a right curve, the outer wheel of the first axle would climb onto the rail, causing the inner wheel to derail first. Therefore, the rail directly below the 1st-Right side wheel in Fig. 2, which corresponds to the inner wheel, was removed immediately after the calculation began. This allowed the displacement of each vehicle component during wheel fall to be determined.

2.4 Results of theoretical analysis

2.4.1 Drop distance of the 1st-Right side wheel

As an example of theoretical analysis results, Fig. 3 shows the relationship between the drop distance of the first 1st-Right side wheel and the elapsed time since the drop began.

Figure 3 shows that the 1st-Right side wheel drops by 126 mm, which is the difference between the rail height of 50 kgN and the height of the wheel flange. It takes approximately 0.13 seconds to reach the ground. Therefore, the installation location of the contact sensor was identified as areas where there is significant displacement during the first 0.13 seconds of wheel descent, and where contact is possible due to the proximity of various bogie components. The details of the identified locations are shown below.

2.4.2 Extracted installation locations for contact sensors

Theoretical analysis has identified the axle box guide, which is near the wheel axle, as the optimal location to install contact sensors. The axle rubber and the axle box support rubber are released vertically at this location, having been compressed by the wheel load. This enables the axle to descend more quickly than the bogie frame, thereby bringing the axle box guide and axle bearing closer

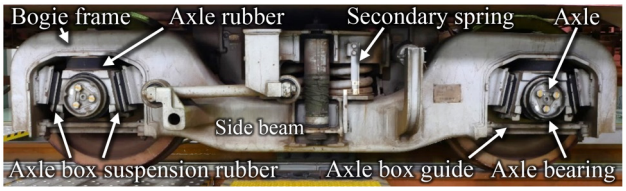

Fig. 1 Appearance of bogie used for numerical simulation

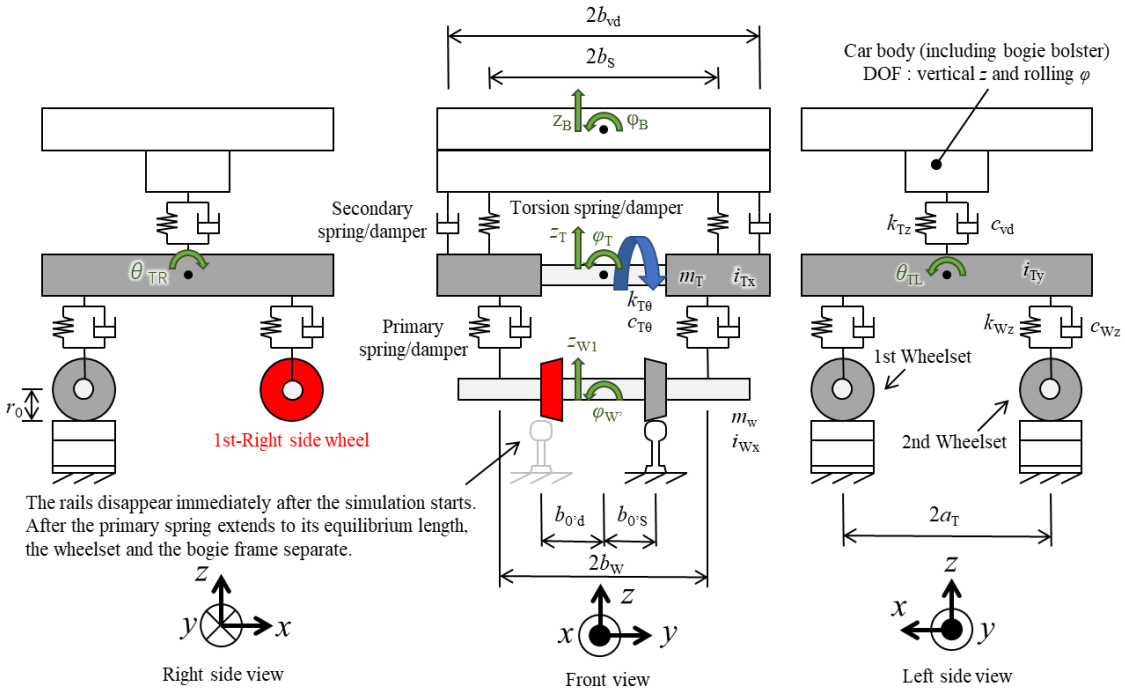

Fig. 2 Mechanical model of the half-car body used in theoretical study

together. Theoretical analysis showed this proximity exceeds that at other locations. Furthermore, a large number of contact marks have been found on the top surface of the axle box guide in the past derailment investigations [7].

For the reasons stated above, the top surface of the axle box guide, as shown in Fig. 4, was selected as the location for installing the contact sensor.

3. Application methods for contact sensors

3.1 Selection of contact sensors

As shown in Fig. 5, there are two types of contact sensor: an Arbeit contact sensor (hereinafter, referred to as the A-contact), which changes from an electrically non-conductive state to a conductive state upon contact with the detection target; and a Break contact sensor (hereinafter, referred to as the B-contact), which changes from a conductive state to a non-conductive state. For this study, considering factors such as size and cost, the T05GY1 (manufactured by IDEC Corporation) was selected for the A-contact, and the Touch-Off Sensor N (manufactured by Idel Corporation) was selected for the B-contact. Figure 6 shows the appearance of the selected contact sensors. As can be seen in Fig. 6, both sensors are approximately 10 mm wide. The thickness for the A-contact is approximately 5 mm thick, while the B-contact is approximately 11 mm thick. The length was adjusted according to the specific usage conditions.

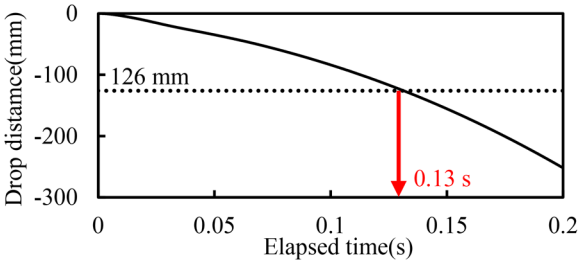

Fig. 3 Drop distance of the 1st-Right side wheel

Fig. 4 Installation locations for contact sensors

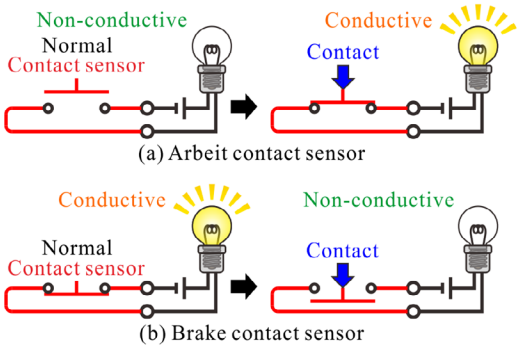

Fig. 5 Operating mechanism of contact sensors (a) Based on the operation instruction; contact changes from "open state" to "closed state." (b) Based on the operation instruction; contact changes from "closed state" to "open state"

The two selected contact sensors, both A-contact and B-contact, can detect contact with a slight load of 10 N to 15 N. However, if the contact sensors are mounted directly on the bogie, there is a possibility of false detection when flying objects, such as snow clumps, strike the sensor during operation. Therefore, we created a derailment detection sensor by combining the contact sensor with a protective rubber cover as shown in Fig. 7. This sensor only detects only when it comes into contact with an object which applies a load exceeding a certain threshold.

3.2 Derailment detection sensor

As shown in Fig. 7, the derailment detection sensor has a rubber cover consisting of rubber sandwiched between an upper steel plate and a lower steel plate. Furthermore, the rubber cover enables contact pins to be attached to the inner side of the upper steel plate, where they will make contact with the contact sensor. The shape and material of both the rubber cover and contact pin vary depending on the type of contact sensor. However, when using the rubber cover, the contact pin can only press the sensor when sufficient pressure is applied to deform the rubber.

There are two types of derailment detection sensor, each combining a differently shaped rubber cover with either an A-contact or a B-contact. Hereafter, the derailment detection sensor using the

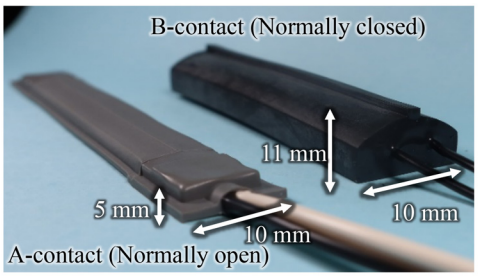

Fig. 6 Appearance of selected contact sensors

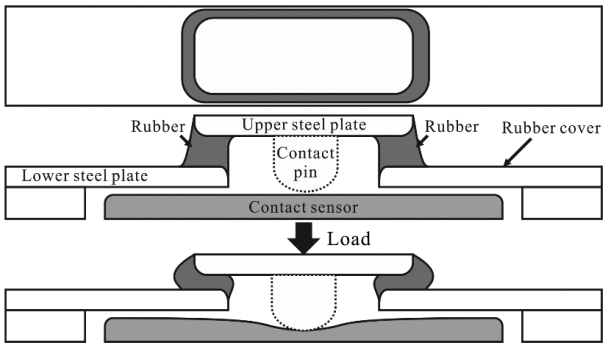

Fig. 7 Schematic of rubber cover

A-contact is referred to as Type A; the one for the B-contact as Type B. The appearance of Type A and Type B is respectively shown in Fig. 8. Note that the figure shows the rubber cover turned inside out to show the internal structure. The characteristics of each derailment detection sensor are described as follows:

- Both type A and type B have a structure in which the contact sensor is covered by a rubber cover casing.
- For type A, it is installed on the top surface of the axle box guide, for type B, it is installed in a groove machined into a metal piece that matches the shape of the axle box guide.
- The contact pin for Type A was made of rubber. This prevented the thin A-contact from being severed upon contact. On the other hand, the contact pin for Type B was made of metal. This was because of the greater distance to the contact sensor, which made installing a rubber contact pin difficult. The shape of the contact pin was modified according to the thickness and shape of the contact sensor. Both were adjusted to detect deformation of the rubber cover by approximately 1 mm.
- The length of the rubber cover was set to 200 mm for Type A and 75 mm for Type B. This eliminated the need to machine a long groove in a jig with the same shape as the axle box guide during manufacture of Type B.

3.3 Detection performance of derailment detection sensors

A test was conducted to evaluate the detection performance of the manufactured derailment detection sensor, hereinafter referred to as 'the detection sensitivity test.' Figure 9 shows an example of the test setup for Type A.

As shown in Fig. 9, the derailment detection sensor was installed on a material testing machine for the detection sensitivity test and loaded from above. During loading, the load was applied using an axle bearing simulation fixture, considering the actual contact conditions of the derailment detection sensor. The test measured both the load and the displacement of the rubber cover. Additionally, an ohmmeter was connected to the derailment detection sensor. Changes in electrical conductivity (contact open/closed status) were evaluated based on the measured resistance values.

Figure 10 shows an example of the relationship between load and rubber cover displacement in the detection sensitivity test, along with the waveform of the conductive state measured by the ohmmeter (hereafter, detection waveform). Since detection is defined as occurring when the detection waveform changes, the displacement at this point is referred to as the detection displacement, and the load is referred to as the detection load in this paper.

As shown in the detection waveform of Fig. 10, Type A changed from non-conductive to conductive during detection, while Type B changed from conductive to non-conductive. The detection displacement was approximately 1 mm for Type A and approximately 0.9 mm for Type B. The detection load was approximately 1 kN for Type A and approximately 2 kN for Type B. Detection sensitivity tests were conducted on three units for both Type A and Type B. Some variation was observed, but the detection displacement ranged from 1.0 mm ± 0.3 mm, and the detection load ranged from 2 kN ± 1 kN. It is thought that this variation is due to differences in the contact sensors and the shape of the contact pins.

The results of the detection sensitivity test confirmed that the developed derailment detection sensor can only detect when a certain load is applied. Furthermore, it is anticipated that the weight of the wheelset will be applied to the derailment detection sensor during derailment. Considering the wheelset's own weight and accelerations that exceed the expected gravitational acceleration during derailment, it is anticipated that a load of over 10 kN will be applied during derailment. Therefore, the detection performance of the manufactured derailment detection sensor is considered to be satisfactory.

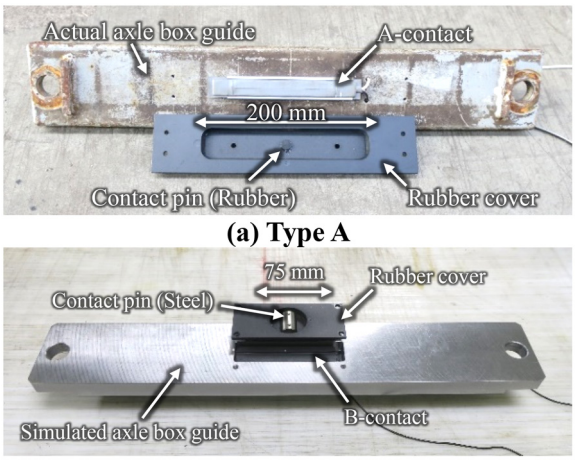

Fig. 8 Appearance of the derailment

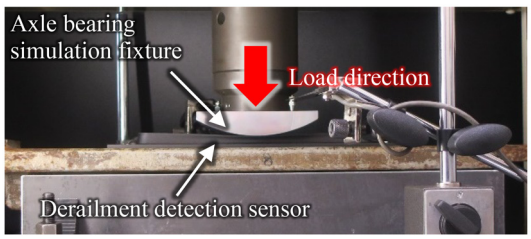

Fig. 9 Status of the detection sensitivity test

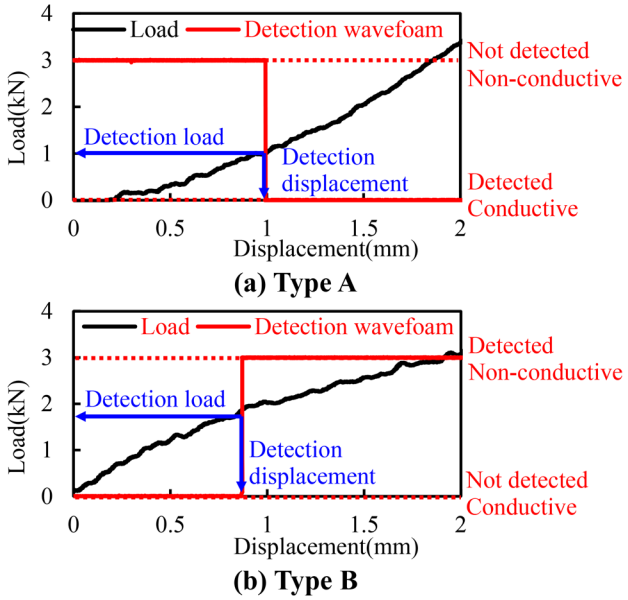

Fig. 10 Example of the detection sensitivity test results.

4. Derailment detection test

4.1 Derailment method

For the derailment detection test, derailment detection sensors were installed on the actual vehicle shown in Fig. 11. The method of derailing the vehicle during the derailment detection test is described below.

After the rail-road vehicle pushes the vehicle for a certain distance, when the rail-road vehicle is stopped, the vehicle then continues to coast under its own momentum. Subsequently, the wheels of the bogie equipped with the derailment detection sensor climb onto the derailer installed on the left rail relative to the direction of travel, as shown in Fig. 12. As a result, the flange of the left wheel climbs onto the rail along the derailer and derails by rolling off the outer rail. Here, the attack angle during derailment was set to 4º. This setting was determined by considering actual derailment, assuming the wheel climbs onto the rail and then travels approximately 1 meter before derailing.

4.2 Installation locations for derailment detection sensors

As shown in Fig. 13, derailment detection sensors were installed on all four axle box guides of the same bogie for the derailment detection test.

Fig. 11 Appearance of vehicle used for derailment detection test

Fig. 12 Appearance of installation of the derailer

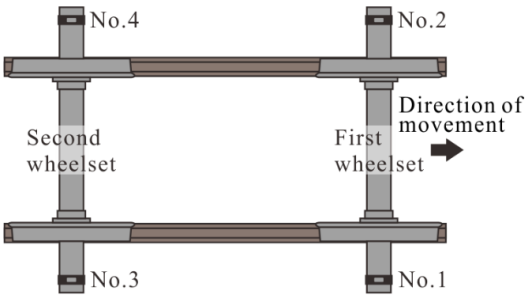

Fig. 13 Installation locations for derailment detection sensors

4.3 Measurement items

The derailment detection test measured the detection waveform of the derailment detection sensor and the relative displacement (approach amount of the gap) between the axle bearing and the derailment detection sensor. The detection waveform of the derailment detection sensor was obtained by measuring across the light bulb, as shown in Fig. 5, with 5 V DC battery and the contact sensor connected in series. Therefore, Type A was judged to have detected derailment when the voltage changed from 0 V to 5 V. Conversely, Type B was judged to have detected a derailment when the voltage changed from 5 V to 0 V. Furthermore, to measure the relative displacement between the axle bearing and the derailment detection sensor during derailment, a displacement sensor was installed at the location shown in Fig. 14. This measured the relative displacement between the bogie frame, to which the derailment detection sensor was fixed, and the axle box, to which the axle bearing was fixed.

4.4 Test conditions

Table 1 shows the test conditions for the derailment detection test. A total of six test runs were conducted. Three test runs (Test Nos.1 to 3) were conducted at the speeds of 10 km/h or less at point of derailment. Three test runs (Test Nos.4 to 6) were conducted at speeds exceeding 10 km/h at point of the derailment. Additionally, the distance between the axle bearing and the derailment detection sensor was set to approximately 10 mm and approximately 20 mm, to simulate empty and loaded bogie conditions, respectively.

4.5 Test results

During all test runs, the wheel on the left-hand of the first axle in the direction of travel first mounted the derailer. Then, the wheel on the right-hand derailed from the rail. This aligns with the as-

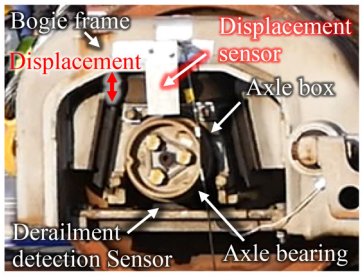

Fig. 14 Location of displacement sensor

Table 1 Test conditions of derailment detection test

Test No.	Speed (km/h)	Sensor type	Sensor No.*			
			1	2	3	4
1	5.6	B	19.0	19.5	19.5	19.5
2	7.5	B	20.0	20.0	19.5	19.5
3	7.2	B	19.5	20.0	21.0	19.5
4	14.0	A	20.0	20.0	19.5	20.0
5	14.8	A	11.0	12.0	12.0	11.0
6	15.6	A	11.0	12.0	11.0	10.0

*) Measurements in the Sensor No. column indicate distance (mm) between the derailment detection sensor and the axle bearing.

sumptions made in the theoretical analysis. We present two examples of the test results here. Test No.1, with derailment detection sensor of Type B and a speed of 5.6 km/h, was conducted at speeds below 10 km/h. Test No.6, with derailment detection sensor of Type A type and a speed of 15.6 km/h, was conducted at speeds above 10 km/h.

Figure 15 shows the condition of the bogie after derailment.

As shown in Fig. 15, Tests No.1 and 6, only both axles of the bogies equipped with sensors actually derailed. In Test No.1, the first axle traveled approximately 2 meters from the derailer before stopping. In Test No. 6, the first axle traveled approximately 8 meters from the derailer before stopping. The rubber cover of the derailment detection sensor was deformed due to contact with the axle bearing.

Figure 16 shows the detection waveform for Sensor No. 3, as well as the waveform of the relative displacement between the axle bearing and Sensor No. 3 at its installation location during Tests No.1 and 6. Fig. 17 shows the state of the bogie at times (I) and (II) in Fig. 16. The negative relative displacement shown in Fig. 17 indicates a decrease in the distance between the axle and the sensor.

As shown in Fig. 17, the detection waveform indicates that in both Tests No. 1 and 6, derailment detection occurs after the wheels of the first axle derail and land, but before the wheels of the second axle derail and land.

The detection conditions for the derailment detection sensor were examined based on the relative displacement waveform in

(a) Test No. 1 (b) Test No. 6

Fig. 15 Conditions of the bogie after derailment detection tests

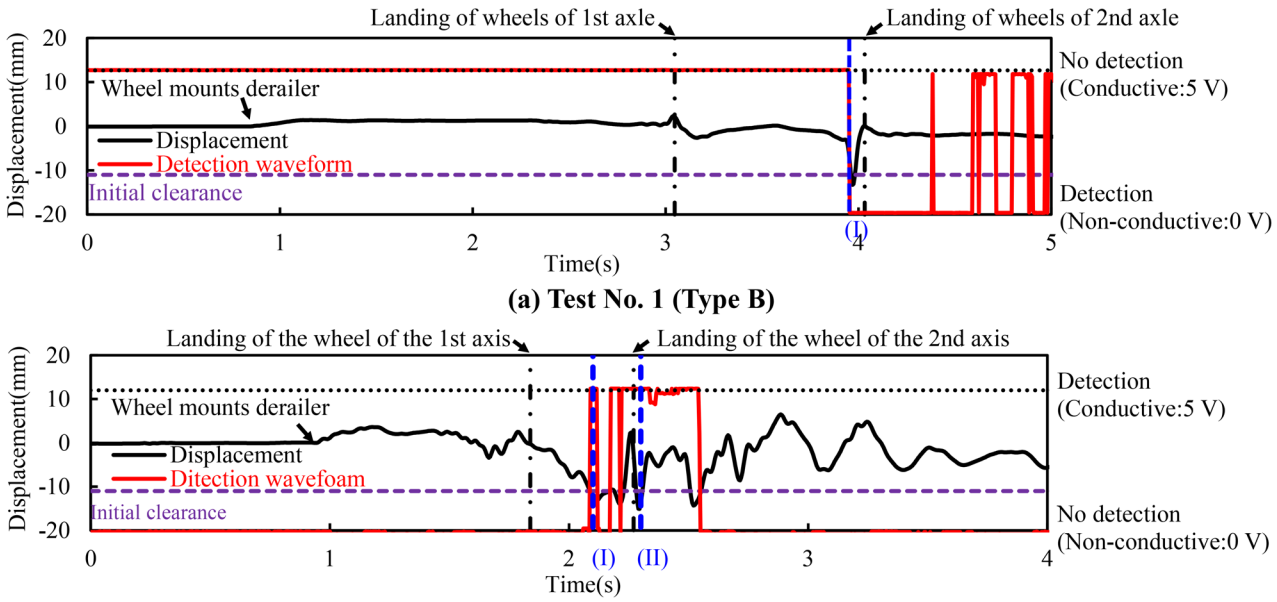

(a) Test No. 1 (Type B)

(b) Test No. 6 (Type A)

Fig. 16 Time wave of displacement gauge and derailment detection sensor.

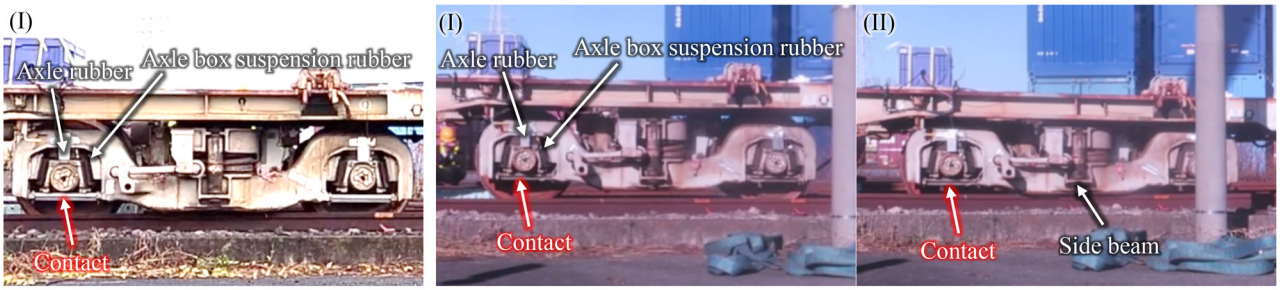

(a) Test No. 1 (b) Test No. 6

Fig. 17 Detection conditions by derailment detection sensors.

Fig. 16 and the sensor detection waveforms at time (I) in Fig. 17(a) and times (I) and (II) in Fig. 17(b). As a result, it is considered that detection can be achieved with the two following conditions:

The first condition, the derailment detection sensors detect that the wheels of the second axle derail and land during time (I) in Figs. 16 and 17, after the wheels of the first axle have landed. In this time, the wheels of the first axle landed and the wheels of the second axle derailed and landed. The detected factors are as follows: the bogie frame pitches forward due to the drop of the first axle, causing the distance between the axle box guide fixed to the bogie frame and the axle bearing to decrease. Furthermore, as the second axle's wheels leave the rails, the compressed axle rubber and axle box support rubber are released, generating a rebound force that causes them to drop faster than the bogie frame. It is considered that the combination of these factors enabled detection.

As another condition, the derailment detection sensors were detected at time (II) shown in Figs. 16(b) and 17(b). In this time, detection occurred after the wheels on the second axle landed, and when the side beam of the bogie climbed onto the rail. One factor is that the height position of the bogie frame is fixed when its side beams ride onto the rails. Meanwhile, the position of the axle bearings moves up and down as the bogie passes over the sleepers, and it is thought that the wheels passing over the gaps between the sleepers causes the axle bearings to approach the sensors, enabling detection. In the case of Test No.1, the bogie stopped immediately after the second axle dropped, preventing the wheels from passing over the gap between the sleepers. Consequently, neither the first nor the second axle brought the axle bearing and sensor close enough for detection under these conditions.

4.6 Summary of test results and identification of issues

Table 2 summarizes the results of all the test runs. The descriptions used in the table are explained below.

- The number in the Sensor No. column indicates the distance (in mm) between the axle bearing and the derailment detection sensor.
- ○: indicates that the axle bearing contacted the derailment detection sensor, so that a change in the detection waveform voltage value occurred.
- ×: indicates that the derailment detection sensor did not contact, so that the detection waveform voltage value did not change.
- △: indicates that the derailment detection sensor did not contact, but the detection waveform voltage value changed.

Table 2 shows that sensor No. 3 exhibited traces of contact with the derailment detection sensor in all test runs, regardless of speed or distance from the axle bearing. Furthermore, post-test inspection of the derailment detection sensors revealed that the rubber cover of sensor No. 3 was deformed by approximately 3.5 mm in all the cases, regardless of speed or distance from the axle bearing.

Additionally, regarding differences based on contact sensor type, Type A showed changes in the detection waveform voltage value whenever contact occurred. However, Type B exhibited changes in the detection waveform voltage value even when no contact was made, as indicated by the symbol "△" in the table. Regarding this factor, the B-contact is normally in the state as shown in Fig. 18(a). In this state, one of the two conductors (A) is in electrical contact with the other conductor (B) via a spring element, which maintains electrical conduction. However, as shown in Fig. 18(b), when a load is applied the contact between the conductors, supported by the spring element, is broken, interrupting electrical conduction. During the derailment detection test, the significant vibration

Table 2 Summary of Derailment Detection Test Results

Test No.	Speed (km/h)	Sensor type	Sensor No.			
			1	2	3	4
1	5.6	B	19.0	19.5	19.5	19.5
			×	×	○	×
2	7.2	B	19.5	20.0	21.0	19.5
			○	×	○	△
3	7.5	B	20.0	20.0	19.5	19.5
			×	×	○	△
4	14.0	A	20.0	20.0	19.5	20.0
			○	○	○	○
5	14.8	A	11.0	12.0	12.0	11.0
			○	○	○	○
6	15.6	A	11.0	12.0	11.0	10
			○	○	○	○

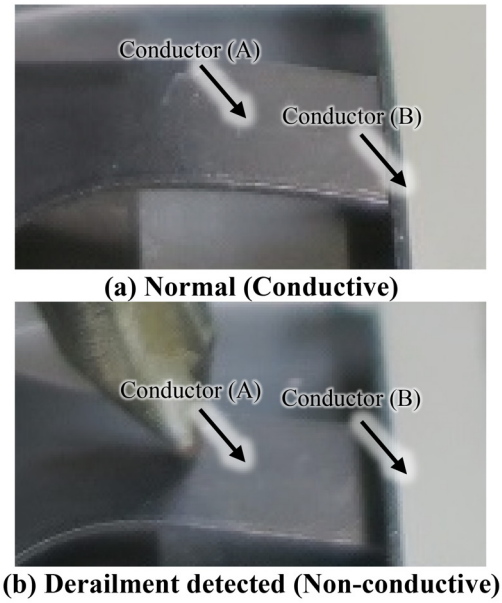

Fig. 18 Internal situation of the B-contact

generated by derailment may have momentarily caused the two conductors to lose contact and become non-conductive, even though the axle bearing was not in contact with the derailment detection sensor. As mentioned above, wagons have generally high support rigidity. Therefore, relatively large vibrations can occur on the bogie frame equipped with the derailment detection device when passing over joints and similar features during normal operation, which can potentially cause similar events. Consequently, the performance of B-contact must be evaluated by conducting tests on actual tracks and by other means in the future.

The results of the derailment detection test confirmed that the derailment detection sensor can detect a derailment immediately if both axles of the same bogie derail. On the other hand, the test results suggest that the derailment detection sensor may have difficulty immediately detecting the derailment if only the first axle derails. However, although this is not reproducible in this derailment detection test, significant vertical vibration of the axle is anticipated, if

the vehicle continues moving with only the first axle derailed and passes over structures like sleepers. When combined with an axle box guide, this phenomenon may enable derailment detection. Further investigation using simulations and other methods is necessary to understand such scenarios.

5. Conclusions

To reduce damage of ground facilities after wagon derailments, there is a need for new sensors that can detect derailments quickly and easily. Therefore, we proposed a method using mechanical contact sensors installed on the bogie to detect derailments, and evaluated their performance. The results yielded the following findings:

1) Based on theoretical analysis and past findings, the upper surface of the axle box guide was selected as the installation location for the contact sensor, as it is likely to come into contact with the axle bearing in the event of a derailment.
2) To prevent false detection, a derailment detection sensor was fabricated incorporating a rubber cover to protect the contact sensor. Evaluation of the derailment detection sensor's sensitivity revealed that it could detect contact when deformed by approximately 1 mm. The load at this point was 2 kN ± 1 kN.
3) Derailment detection tests were conducted to evaluate the performance of the derailment detection sensor. These tests involved derailing an actual vehicle equipped with a bogie fitted with the derailment detection sensor. The results showed that the sensor detected derailment when the second axle fell, and as it continued running.

In summary, the derailment detection test results confirmed that the derailment detection sensor can detect derailments at an early stage. However, issues were also identified, such as the potential for false detection when using a contact sensor with a B-contact. Therefore, future steps include conducting running tests for practical implementation to evaluate sensor reliability, as well as investigating methods to transmit derailment information obtained by the sensor to the driver's cab of locomotive.

References

[1] Japan Transport Safety Board, Train Derailment Accident between Kuzumi and Namegawa Stations of the Narita Line of the Japan Freight Railway Company, *Railway Accident Investigation Report*, RA2012-5 (2012) (in Japanese).
[2] Hung, C., Suda, Y., Aki, M., Tsuji, T., Morikawa, M., Yamashita, T., Kawanabe, T. and Kunimi, T., Study on detection of the early signs of derailment for railway vehicles, *Vehicle System Dynamics*, Vol. 48, Supplement (2010), pp. 451-466.
[3] Oyama, H., Nagamoto, M., Matsuoka, S., Yano, K. and Maeda, T., Development of derailment detector with twin sensor, *J-Rail 2018 Proceeding*, No. 18-83, (2018), (in Japanese).
[4] Saito, K., Misu, Y. and Yoshida, Y., Development of derailment detection device, *JR East Technical Review*, No. 2 (2003), pp. 69-72 (in Japanese).
[5] Diana, G., Sabbioni, E., Somaschini, C., Tarsitano, D., Cavicchi, P., Di Mario, M. and Labbadia, L., Full-scale derailment detection tests on freight wagons, *Vehicle System Dynamics*, Vol. 60, No. 6 (2022), pp. 1849-1866.
[6] Imai, K., Development of container freight wagon condition monitoring equipment, *R & M*, No. 6 (2014), pp. 20-24.
[7] Japan Transport Safety Board, Train Derailment Accident between Izumisawa and Satsukari Stations of the Esashi Line of the Japan Freight Railway Company, *Railway Accident Investigation Report III*, RA2015-9 (2015) (in Japanese).
[8] Iijima, H., Yoshida, H., Suzuki K. and Yasuda, Y., A study of prevent the wheel-climb derailment on the low speed ranges, *JR East Technical Review*, No. 49 (2014), pp. 25-28.
[9] Tanaka, K. and Sugiyama, H., Prediction of railway wheel load unbalance induced by air suspension leveling values using quasi-steady curve negotiation analysis procedure, *Proceedings of Institution of Mechanical Engineers*, Park K, Vol. 20 (2020), pp. 19-37.
[10] Adachi, M., Shimomura, T., Sato, E., Development of evaluation system of geometrical characteristics of contact point between wheel and rail with consideration of wear, *RTRI Report*, Vol. 20, No. 6 (2006), pp. 17-2.

Authors

Shogo MAMADA, Ph.D. in Eng
Manager, Vibration-Isolating Materials Laboratory, Materials Technology Division
Research Areas: Isolating Rubber, Functional Rubber, Composite Materials

Tatsuya OTA
Senior Researcher, Vibration-Isolating Materials Laboratory, Materials Technology Division
Research Areas: Isolating Rubber, Composite Materials, Environment Materials

Kohei MIYAHARA
Senior Researcher, Vehicle Dynamics Laboratory, Vehicle Technology Division
Research Areas: Vehicle Dynamics, Multibody Dynamics, Vehicle Running Safety

Kazuto KOSUGI
Researcher, Vehicle Dynamics Laboratory, Vehicle Technology Division (Former)
Research Areas: Vehicle Dynamics, Multibody Dynamics, Vehicle Running Safety

Numerical Analysis of the Hydrogen Leakage from a Fuel Cell Railway Vehicle Stationed in a Tunnel

Takashi FUKUDA
Heat and Air Flow Analysis Laboratory, Environmental Engineering Division (Former)

Sanetoshi SAITO
Environmental Engineering Division

One of the initiatives to decarbonize railways is the development of fuel-cell vehicles. However, in order to put fuel-cell railway vehicles into practical use, it is necessary to confirm their safety. One particularly important issue in confirming safety is the evaluation of hydrogen concentration in the event of a hydrogen leak in a tunnel. In this study, a numerical analysis was performed to investigate the hydrogen leak flow from a stationary railway vehicle in a tunnel. The results showed that the leaked hydrogen rose toward the crown of the tunnel and flowed toward both tunnel portals. The hydrogen concentration was the highest immediately above the leakage point and decreased rapidly toward both tunnel portals. Additionally, the influence of the location of the leak on the hydrogen concentration distribution was also shown.

Key words**:** *tunnel, fuel cell, hydrogen, numerical analysis*

1. Introduction

Efforts to address global environmental issues have led to demands to reduce carbon dioxide and nitrogen oxide emissions. This applies even to railways, which are more energy-efficient than other modes of transportation. Although diesel-powered railway vehicles are currently the main form of transportation in non-electrified lines, there has recently been a shift toward motor-driven diesel hybrid vehicles [1] and battery-powered vehicles [2]. However, diesel hybrid vehicles still have carbon dioxide emission issues, and battery-powered vehicles have limited operating ranges and can only be used on certain lines [3].

One initiative addressing these issues is the development of vehicles equipped with fuel cells that generate electricity through a chemical reaction of hydrogen and oxygen. In Japan, Railway Technical Research Institute (RTRI) [4][5] and JR East [3][6] have developed test vehicles powered by fuel cells and batteries. RTRI has conducted running tests on its in-house test track, while JR East is conducting running tests on commercial lines. To put the fuel-cell operated vehicles into service however, it is necessary to verify their safety. This requires understanding the flow characteristics and hydrogen concentration distribution in enclosed environments, such as tunnels, in the event of a hydrogen leak.

Hydrogen has a low specific gravity of 0.0695 relative to air, and it is prone to diffusion. Its flammability limit in air is extremely wide, ranging from 4% to 75% (for example, the flammability limit of methane is 5% to 15%) [7]. Therefore, safety must be taken into account when handling hydrogen.

Several analyses and safety assessments of hydrogen leaks in tunnels involving automobiles equipped with fuel cells have been conducted [8][9]. Europe has conducted numerical calculations for safety assessments in the event of hydrogen leaks from railway vehicles [9]. However, railway vehicles have a larger cross-sectional area than automobiles. Additionally, railway tunnels in Japan have a smaller cross-sectional area than roads and European railway tunnels. Yet, there are no known studies on hydrogen leaks under such conditions.

This study assumes a hydrogen leakage from equipment on the roof of a stationary railway vehicle in a single-track tunnel on a conventional railway line in Japan. We investigated the flow characteristics and concentration distribution of hydrogen through numerical analysis [10].

2. Numerical analysis conditions

The vehicles assumed in this numerical analysis are shown in Fig. 1 and Table 1. Both the vehicle body and roof-mounted equipment were simulated as cuboids. The underfloor equipment and bogies were also simulated as a single cuboid. These dimensions were determined based on commuter vehicles in Japan [11]. The length of each vehicle's body was 19.5 m, and two vehicles were coupled together with a 0.5 m gap between them. Here, the height z_L of the equipment mounted on the roof was set to three values: 0.10 m, 0.45 m, and 0.60 m.

The cross-sectional shape of the tunnel assumed in this numerical analysis is shown in Fig. 2, and the specifications are shown in Table 1. The tunnel cross-section is that of a single-track mountain tunnel for conventional railways in Japan [12], with a total length of 400 m. As shown in Fig. 3, the vehicle is assumed to be stationary at the center of the tunnel along the longitudinal direction. As shown in Figs. 1 and 2, the coordinate system is set with the *x*-axis in the longitudinal direction of the tunnel, the *y*-axis in the track sleeper direction, and the *z*-axis in the vertical direction.

In this numerical analysis, the hydrogen leakage point was set at the top surface of the equipment mounted on the roof on the left vehicle (Car No. 2) shown in Figs. 1, 2 and 3. The offset of the hydrogen leakage point in the track sleeper direction (*y*-axis direction) was set as y_L, and the height of the equipment mounted on the roof was set as z_L. As shown in Table 2, the hydrogen leakage point was set in five cases, which are indicated with check marks.

The hydrogen leakage rate was set at 5 NL/min, based on a study of hydrogen leakage in the automotive field [13], which examined the leakage rate when a nut of pipe joints was loosened by quarter turn. Considering the capacity of the vehicle's pipes, the hydrogen leakage time was set at 3600 s.

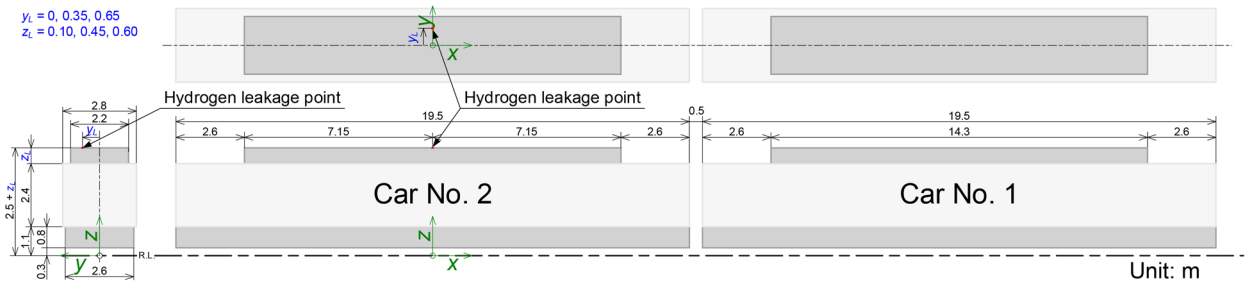

Fig. 1 Vehicle assumed in numerical analysis

Table 1 Vehicle and tunnel specifications

Vehicle	Cross-sectional area (m²)	9.02 (z_L = 0.10 m) 9.79 (z_L = 0.45 m) 10.12 (z_L = 0.60 m)
	Number of cars	2
	Length of train set (m)	39.5
Tunnel	Cross-sectional area (m²)	23.1
	Length (m)	400
Blockage Ratio		0.39 (z_L = 0.10 m) 0.42 (z_L = 0.45 m) 0.44 (z_L = 0.60 m)

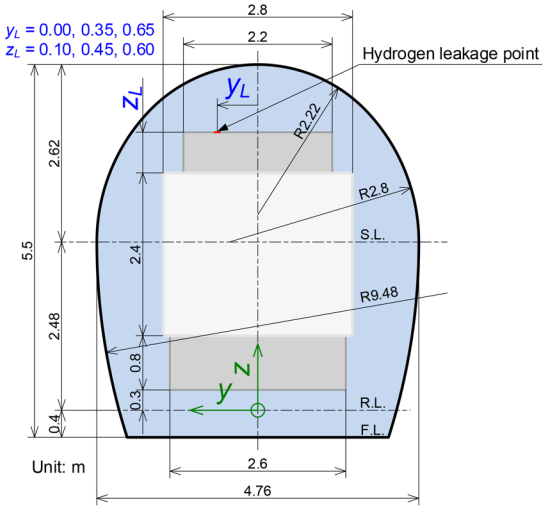

Fig. 2 Cross-section of vehicle and tunnel assumed in numerical analysis and hydrogen leakage point

Table 2 Cases of hydrogen leakage points

Offset in track sleeper direction y_L (m)	Height of roof mounted equipment z_L (m)		
	0.10	0.45	0.60
0.00	✓	✓	✓
0.35			✓
0.65			✓

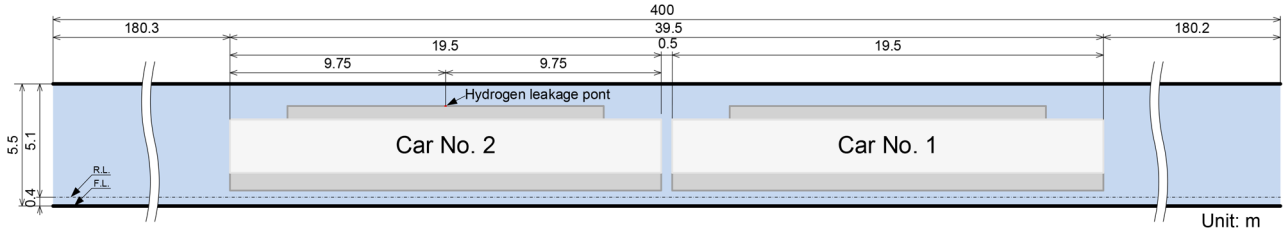

Fig. 3 Vehicle position inside the tunnel

3. Numerical analysis method

Numerical analysis was conducted using Fire Dynamics Simulator (FDS) Version 6.8.0 [14] developed by the National Institute of Standards and Technology (NIST), USA. FDS is a software tool for analyzing fire dynamics based on the assumption of low Mach number approximation. It uses the Large Eddy Simulation (LES) method to numerically analyze turbulence flow. It is also applicable for general thermal fluid analysis that does not involve fire phenomena. The cartesian grid is used for computational grids.

In this study, we first compared the numerical results with the experiments using a combustible gas wind tunnel at the National Institute of Advanced Industrial Science and Technology (AIST), as well as numerical analyses [15], in order to examine the subgrid

scale (SGS) model and the appropriate grid resolution for LES. Figure 4 shows an overview of the experiments and numerical analyses. Figure 5 shows examples of comparisons between the experiments and numerical analyses in the literature [15] and the numerical analysis results of this study. Based on these comparisons, the Smagorinsky model was used as the SGS model, with the Smagorinsky constant C_s set to 0.1 in this study. Additionally, the grid width was set to 10 cm in the x-direction and 5 cm in the y-direction and z-direction.

The hydrogen leakage rate of 5 NL/min set in Chapter 2 corresponds to a mass flow rate of 7.44×10^{-6} kg/s. In numerical analysis, this mass flow rate is set to flow out from 1 × 2 cells (0.1 m × 0.1 m) on the xy plane at a mass flux of 7.44×10^{-4} kg/m^{2}s.

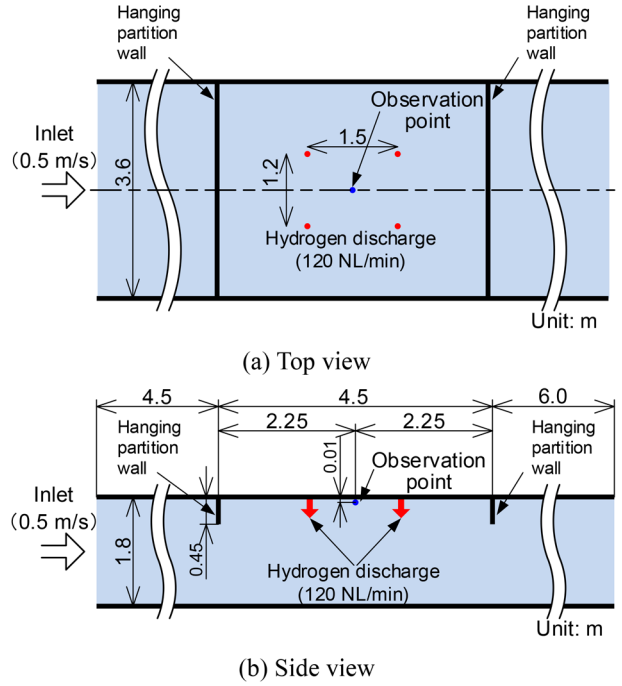

Fig. 4 Overview of experiments and numerical analysis on hydrogen retention using a combustible gas wind tunnel in AIST

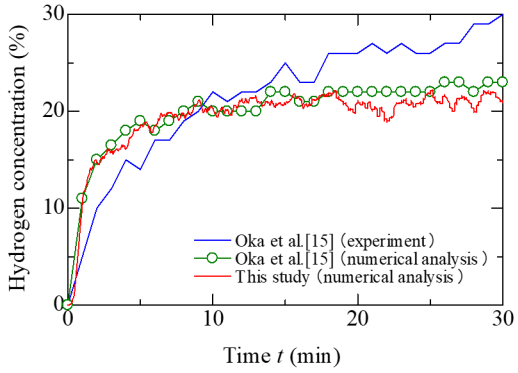

Fig. 5 Comparison results of the numerical analysis with the previous study

4. Numerical analysis results

Figure 6 shows the distribution of hydrogen concentration along the longitudinal section at the tunnel center axis (y = 0.00 m) when the roof-mounted equipment height z_L = 0.60 m and the hydrogen leakage point is not offset in the track sleeper direction (y_L = 0.00 m). Figure 7(a) shows the distribution of hydrogen concentration at the tunnel cross section at the hydrogen leakage point (x = 0.00 m). Hydrogen leaks from the leakage point on the upper surface of the roof-mounted equipment rises almost vertically to the crown of the tunnel. It then flows toward both tunnel portals along the crown of the tunnel. A similar phenomenon occurs in the case of buoyancy-driven flow caused by a tunnel fire. The temperature decreases due to heat absorption by the tunnel, causing the buoyancy to be lost, and the flow currents to gradually descend [16]. In contrast, in the case of hydrogen, buoyancy does not decrease even when it is flowing toward both tunnel portals. Therefore, it does not descend but flows along the tunnel crown toward both portals. Note that at the set leakage time of 3600 seconds, hydrogen has not reached both tunnel portals. Therefore, it is considered that the same situation as the results of this numerical analysis applies to tunnels longer than 400 meters.

Figures 7(b) and (c) show the hydrogen concentration distribution at the tunnel cross section at the hydrogen leakage point (x = 0.00 m) when the hydrogen leakage point is offset in the track sleeper direction (y-direction). Hydrogen rises almost vertically toward the tunnel arch. After that, hydrogen flows along the tunnel arch toward the tunnel crown, and then flows along the tunnel crown toward both tunnel portals.

Figure 8 shows, for example, the change in hydrogen concentration over time above the hydrogen leakage point (x = 0.00 m, y = 0.00 m) when the hydrogen leakage point is not offset in the track sleeper direction (y_L = 0.00 m). Here, the vertical coordinates z of the hydrogen concentration observation points was set to two

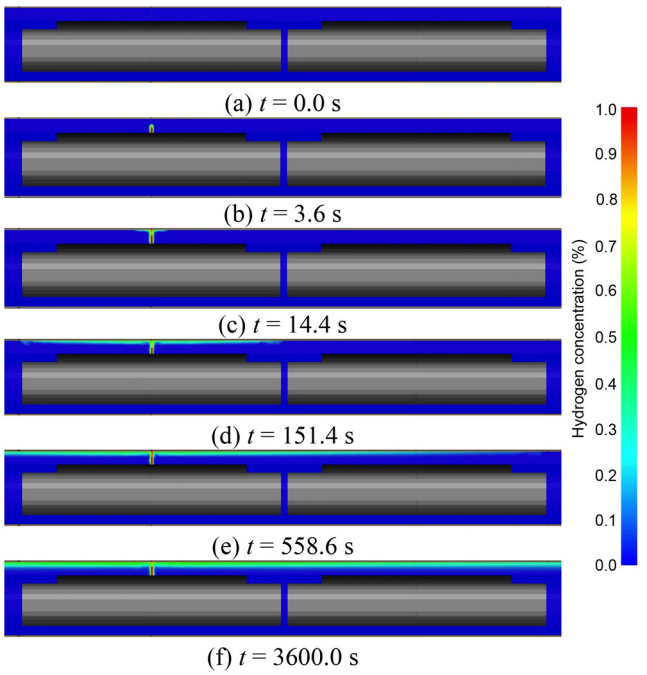

Fig. 6 Changes in hydrogen concentration distribution of longitudinal section at the tunnel center axis (y = 0.00 m, y_L = 0.00 m, z_L = 0.60 m)

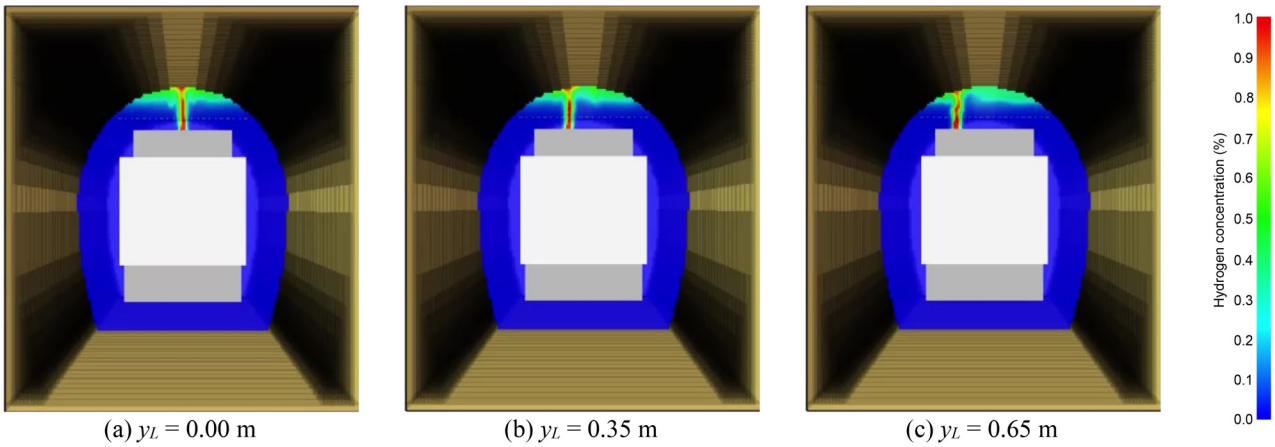

(a) y_L = 0.00 m (b) y_L = 0.35 m (c) y_L = 0.65 m

Fig. 7 Hydrogen concentration distribution in the tunnel cross section (x = 0.00 m, z_L = 0.60 m, t = 3600 s)

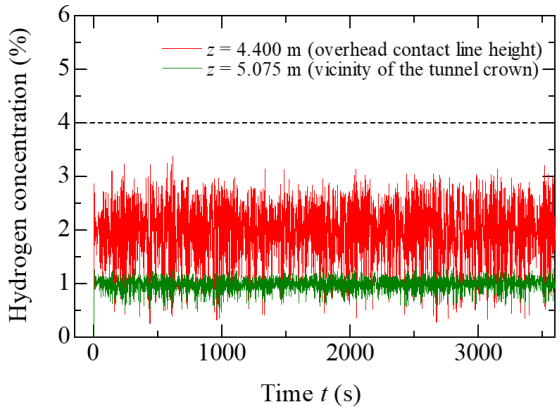

Fig. 8 Changes in hydrogen concentration directly above the leakage point (x = 0.00 m, y = 0.00 m, y_L = 0.00 m, z_L = 0.60 m) over time

values: 4.400 m (overhead contact line height) and 5.075 m (vicinity of the tunnel crown). The height of the overhead contact line was selected as one of the observation points because it was thought that the overhead contact line could ignite hydrogen when fuel cell railway vehicles enter electrified lines in the future. As can be seen from Fig. 8, the hydrogen concentration at the observation point directly above the leakage point becomes quasi-steady immediately after the leak.

The maximum hydrogen concentration at the observation point set on the x-axis was determined from the changes in hydrogen concentration over 3600 s shown in Fig. 8. Figure 9 shows the distribution of the maximum hydrogen concentration on the longitudinal direction when the roof equipment height z_L was changed, assuming that the hydrogen leakage point was not offset on the track sleeper direction (y_L = 0.00 m). From Fig. 9, the maximum value of the hydrogen concentration is the highest directly above the leakage point, decreasing rapidly toward both tunnel portals. Directly above the leakage point at x = 0.00 m, the maximum hydrogen concentration value at z = 4.400 m, which is closer to the leakage point, is greater than that at z = 5.075 m. However, if we exclude the vicinity around the leakage point, the maximum hydrogen concentration is greater at z = 5.075 m which is directly below the tunnel crown, than that at z = 4.400 m. This is because hydrogen is flowing along the upper part of the tunnel. Additionally, when comparing Figs. 9(a) to 9(c), as the roof-mounted equipment is lowered and the distance from the overhead contact line increases, the maximum hydrogen concentration at overhead contact line height z = 4.400 m decreases.

Figure 10 shows the vertical distribution of the maximum hydrogen concentration directly above the hydrogen leakage point (x = 0.00 m, y = 0.00 m) when the hydrogen leakage point is not offset in the track sleeper direction (y_L = 0.00 m). As can be seen from Fig. 10, the maximum hydrogen concentration decreases as the distance from the leakage point increases. At the overhead contact line height of z = 4.400 m, the hydrogen concentration decreases as the roof-mounted equipment is lower and the distance to the overhead contact line is greater. On the other hand, the hydrogen concentration near the tunnel crown varies little due to differences in the height on the roof-mounted equipment. Additionally, while hydrogen rises from the leakage point toward the tunnel crown, the concentration in the vicinity of the tunnel crown is the lowest. This is because hydrogen diffuses as it rises. After reaching the crown, it does not stagnate but flows toward both tunnel portals.

Figure 11 shows the distribution of the maximum hydrogen concentration in the track sleeper direction (y-axis direction) at the overhead contact line height z = 4.400 m when the hydrogen leakage point is offset in the track sleeper direction (y-axis direction) and the roof-mounted equipment height z_L = 0.60 m. In all cases where the hydrogen leakage point is offset in the track sleeper direction (y-axis direction), the maximum hydrogen concentration forms a chevron curve with a peak directly above the leakage point. It can also be seen that the concentration drops to nearly zero approximately 0.25 m from the leakage point. Therefore, when designing vehicles, it is possible to reduce the hydrogen concentration at the overhead contact line positions that could act as ignition sources by ensuring that equipment openings mounted on the roof are not placed within the range of overhead contact line offset.

Furthermore, Figs. 8 to 11 show that under the conditions assumed in this numerical analysis, such as the tunnel, vehicle, and hydrogen leakage rate, the maximum hydrogen concentration at the overhead contact line height is less than 4%, which is the flammability limit of hydrogen in air.

5. Conclusions

Numerical analysis was conducted on hydrogen leakage from roof-mounted equipment of a stationary railway vehicle inside a tunnel to investigate the flow characteristics and concentration distribution of hydrogen inside the tunnel. The results are summarized

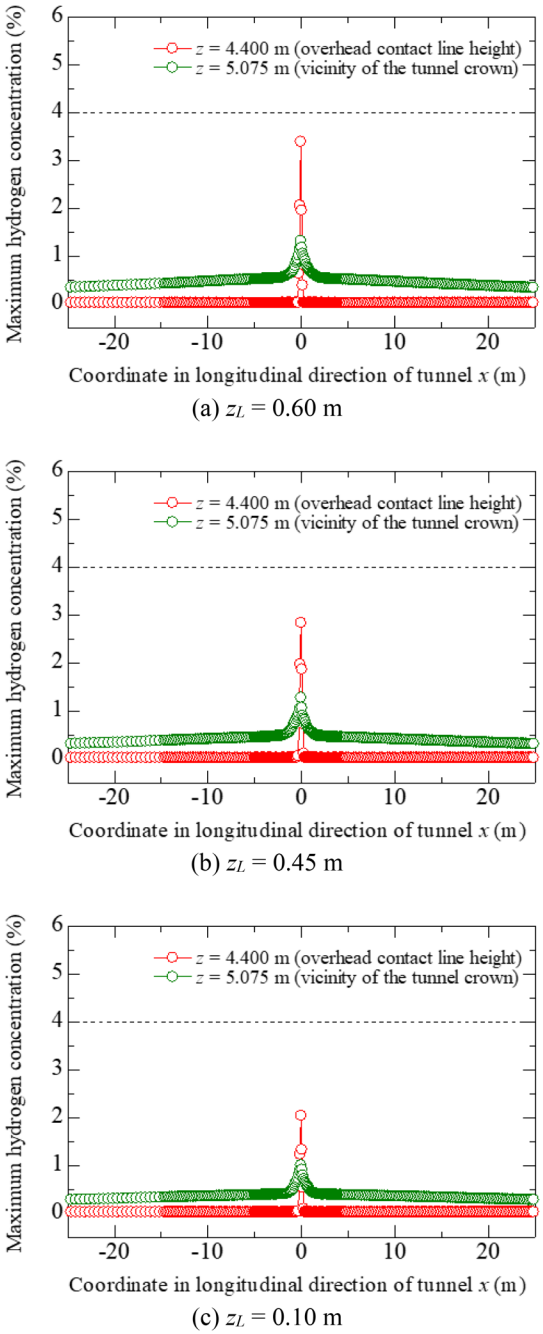

Fig. 9 Distribution of hydrogen concentration in longitudinal direction of the tunnel (y = 0.00 m)

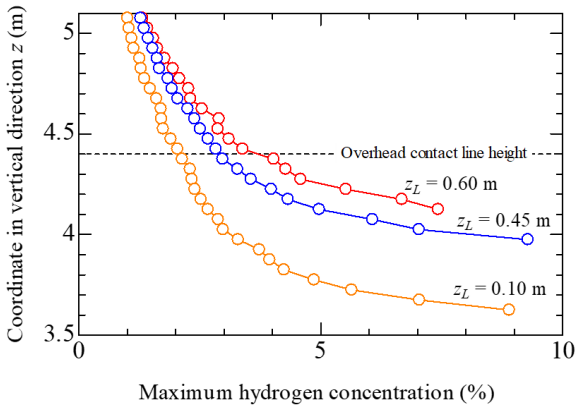

Fig. 10 Distribution of hydrogen concentration in vertical direction (x = 0.00 m, y = 0.00 m)

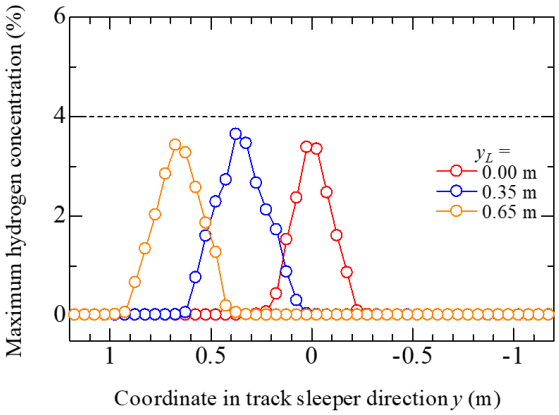

Fig. 11 Distribution of hydrogen concentration in the direction of track sleeper at overhead contact line height (x = 0.00 m, z = 4.40 m, z_L = 0.60 m)

below.

(1) It was found that the leaked hydrogen rose, reached the crown of the tunnel, and then flowed along the crown to both tunnel portals.
(2) Due to this fluidity, the highest concentration of hydrogen is found directly above the leakage point, at the height of the overhead contact line and in the vicinity of the tunnel crown. These concentrations decrease rapidly toward both tunnel portals.
(3) The hydrogen concentration value at the overhead contact line height decreases when the roof-mounted equipment is lowered, increasing the distance between the leakage point and the overhead contact line.
(4) As the hydrogen leakage point is offset toward the track sleeper direction, the peak position of the maximum hydrogen concentration is also offset.
(5) Under the conditions assumed in this numerical analysis, such as the tunnel, vehicle, and hydrogen leakage amount, the maximum hydrogen concentration at the overhead contact line height is less than 4%, which is the flammability limit of hydrogen in the air.

References

[1] Omura, T., "JR East Series kiha E200 diesel hybrid vehicle," *Rolling Stock & Machinery*, Vol. 15, No. 5, pp. 4–9, 2007 (in Japanese).
[2] Takiguchi, H., "Outline of JR East Series EV-E301 battery-powered vehicle," *Rolling Stock & Machinery*, Vol. 22, No. 5, pp. 4–7, 2014 (in Japanese).
[3] Ichigi, T., "Research and development of energy-saving technologies in the railway sector (Initiatives of the JR East Environmental Engineering Research Laboratory)," *Journal of the Japan Society of Mechanical Engineers*, Vol. 125, No. 1240, pp. 13–16, 2022 (in Japanese).
[4] Yamamoto, T., Hasegawa, H., Furuya, T. and Ogawa, K., "Energy Efficiency Evaluation of Fuel Cells and Battery Hybrid

Railway Test Vehicles," *Quarterly Report of RTRI*, Vol. 51, No. 3, pp. 115–121, 2010.
[5] Ogawa, K., Yoneyama, T., Sudo, T., Kashiwagi, T. and Yamamoto, T., "Performance Improvement of Fuel Cell Hybrid Powered Test Railway Vehicle," *Quarterly Report of RTRI*, Vol. 62, No. 1, 2021, pp. 16–21.
[6] East Japan Railway Company, Integrated Report, 2022, https://www.jreast.co.jp/e/environment/pdf_2022/all.pdf (Accessed: 9 January 2025).
[7] Sato, Y. "Hydrogen properties relating to safety," *Journal of Japan Society for Safety Engineering*, Vol. 44, No. 6, pp. 378–385, 2005 (in Japanese).
[8] Kawabata, N., Nakajima, M. and Tanaka, H, "Flow of hydrogen gas discharged by FCV at tunnel fire accidents (Discharge from FCV loaded into career car)," *Proceedings of the JSME Fluids Engineering Conference*, p. 180, 2005 (in Japanese).
[9] Hansen, O. R., Hansen, E. S., Kjellander, M. T. and Martini, R., "CFD study to assess safety aspects of TPRD releases from heavy-duty hydrogen vehicles and trains in tunnels," *Chemical Engineering Transactions*, Vol. 90, pp. 91–96, 2022.
[10] Fukuda, T. and Saito, S., "Numerical analysis on the hydrogen leakage from rooftop equipment of a stationary train in a tunnel," *Proceedings of the JSME Annual Conference*, 2024 (in Japanese).
[11] Japan Association of Rolling Stock Industries, "Railway vehicles - standard specifications for commuter and suburban trains," *JRIS R 1001*, 2003 (in Japanese).
[12] Railway Technical Research Institute ed., "*Design standards for railway structures and commentary (mountain tunnel)*," Maruzen, pp. 72–73, 2022 (in Japanese).
[13] Naruse, K., Matsushima, K., Itou, S., Matsumura, H. and Taniguchi, T., "Research on safety measures of fuel cell vehicles (survey for establishing technical standards in Japanese legislations)," *Report of National Traffic Safety and Environment Laboratory*, No. 14, pp. 1–59, 2009 (in Japanese).
[14] National Institute of Standards and Technology, "Fire dynamics simulator user's guide," *NIST Special Publication 1019*, Sixth Edition, 2020.
[15] Oka, H, Ogata, Y., Oka, Y. and Ota, S., "Numerical analysis of hydrogen dispersion in wind tunnel modeled on vehicles spaces of pure car carriers," *Journal of the Japan Institution of Marine Engineering*, Vol. 52, No. 4, pp. 123–131, 2017 (in Japanese).
[16] Ingason, H., Li, Y. Z. and Lönnermark A., "*Tunnel fire dynamics*," Springer, pp. 327–328, 2015.

Authors

Takashi FUKUDA, Ph.D.
Senior Chief Researcher, Heat and Air Flow Analysis Laboratory, Environmental Engineering Division (Former)
Research Area: Aerodynamics

Sanetoshi SAITO, Dr.Eng.
Manager, Environmental Engineering Division
Research Areas: Aerodynamics, Fire Dynamics

Analytical Model for Longitudinal Displacement of OCL and Method for Calculating the Equilibrium Point

Yoshitaka YAMASHITA
Current Collection Laboratory, Railway Dynamics Division

Koki SATO
Contact Line Structures Laboratory, Power Supply Technology Division.

Overhead contact lines (OCLs) are subject to longitudinal displacement due to factors such as temperature changes and external forces. Excessive OCL longitudinal displacement may prevent tensioning devices from performing their proper tension adjustment function. It is therefore important to develop a method for calculating and predicting OCL longitudinal displacement in response to changes in temperature and external forces. This paper presents a model for representing OCL longitudinal displacement on a curved track installing tensioning devices and hinged cantilevers at each support point and proposes a method for calculating the equilibrium points of this displacement.

***Key words*:** *hinged cantilever, tensioning device, overhead contact line, equilibrium point*

1. Introduction

Japanese electric railway overhead contact lines (OCLs) are typically anchored at intervals of 1,500 to 1,600 meters or less. To maintain uniform tension in the OCLs, tensioning devices are installed at both ends or on one side of the tensioning section. Hinged cantilevers are also installed on poles to support the OCLs within the tensioning section (Fig. 1). In addition to the function of absorbing longitudinal displacement of the OCL (hereinafter referred to as 'OCL longitudinal displacement') caused by thermal expansion and contraction due to ambient temperature changes via the tensioning device, the hinged cantilevers are designed to allow a certain degree of longitudinal displacement rather than fixing the support points of the OCL rigidly in place. This configuration ensures that the OCL tension remains uniform throughout the tensioning section. The movable components of the tensioning devices and the hinged cantilevers move in response to thermal expansion and contraction of the OCL. Consequently, OCL longitudinal displacement is observed in response to changes in ambient temperature and other factors.

However, OCL longitudinal displacement is sometimes observed due to factors other than ambient temperature. Specifically, these include 'temporary external forces such as pantograph sliding friction and wind pressure loads,' 'continuous external forces such as the self-weight of the OCL on gradient sections,' and 'imbalance of the counterweights in pulley-type tensioning devices on both sides.' In some cases, some of these factors result in the entire OCL within the tensioning section being biased towards one side. This is sometimes referred to as a 'creeping move,' but in this paper, it is referred to as 'biased OCL longitudinal displacement.' For example, in the case of 'the self-weight of the OCL on gradient sections' and 'an imbalance of the counterweights of the pulley-type tension device,' the mechanism causing biased OCL longitudinal displacement is obvious. Literature [1] mentions additional factors that cause biased OCL longitudinal displacement, such as 'curved section' and 'sequence of arrangement of multiple hinged cantilevers of the same type (pull-off- or push-off-type) in succession.' However, it remains unclear why these factors cause biased OCL longitudinal displacement.

Furthermore, our previous research [2] has found that differences in the characteristics of spring-type tensioning devices (e.g. spring constants and friction forces) at both ends of the tensioning section can cause the entire OCL within the tensioning section to become biased toward one side when the OCL expands or contracts due to changes in ambient temperature. When the OCL longitudinal displacement is significantly biased, the tensioning device may exceed its movable range limit, and lose its ability to perform normal tension adjustment functions. As mentioned earlier, elucidating the phenomenon of biased OCL longitudinal displacement is an important issue, but the causal relationship between this phenomenon and its contributing factors remains unclear in some cases. This paper

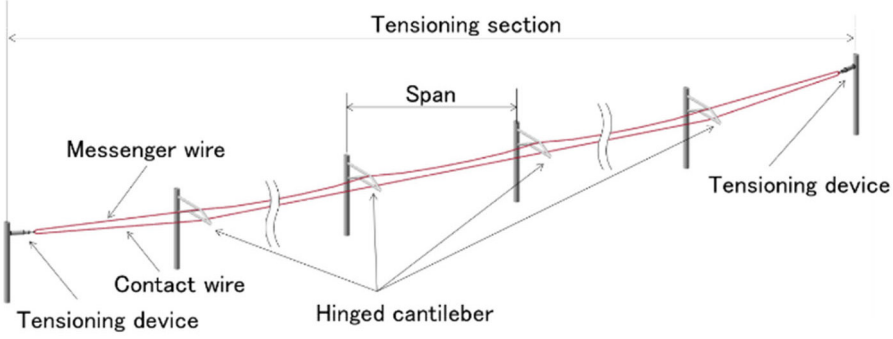

Fig. 1 An overview of overhead contact line within a tensioning section

aims to contribute to the clarification of the phenomenon of OCL longitudinal displacement by describing the calculation method for that. In particular, concerning the factors described in Reference [1] that cause the biased OCL longitudinal displacement, for which the causal relationship with the biased OCL longitudinal displacement has not been clear, we propose an analytical model to express the OCL longitudinal displacement and a calculation method to determine the equilibrium point of the OCL longitudinal displacement that can accommodate curved tracks including hinged cantilevers. In this paper, the equilibrium point is defined as the position (coordinates) of each part of the OCL when it is in a state of static equilibrium with respect to temperature changes and external forces within the tensioning section. Determining the equilibrium point makes it possible to calculate the stroke of the tensioning devices at both ends, as well as the rotation angles of all the hinged cantilevers within the tensioning section.

2. Tensioning device and hinged cantilever

In Japan, there are two main types of tensioning device: spring-type and pulley-type (Fig. 2). Spring- and pulley-type tensioning devices apply tension to OCLs by a spring force and counterweights' mass, respectively. Both pulley- and spring-type tensioning devices are subject to stroke (vertical displacement of the counterweights or expansion/contraction of the spring) due to temperature changes causing expansion/contraction of the OCL. This results in fluctuations of several to tens of percent in the tension of the OCL relative to the standard tension.

The hinged cantilever is designed to allow the cantilever to rotate by using the cantilever mounting point on the pole as a hinge support. The hinged cantilever rotates due to the expansion and contraction of the OCL, which facilitates smooth adjustment of the OCL tension. There are two types of hinged cantilever: pull-off- and push-off-type (Fig. 3). The former pulls the OCLs toward the pole in a direction perpendicular to the track, while the latter pulls the OCLs toward the opposite side of the pole. In the case of a pull-off-type hinged cantilever, the main components of the hinged cantilever located between the OCLs and the pole are subjected to tensile forces. On the other hand, they are subjected to compressive forces in the case of a push-off-type.

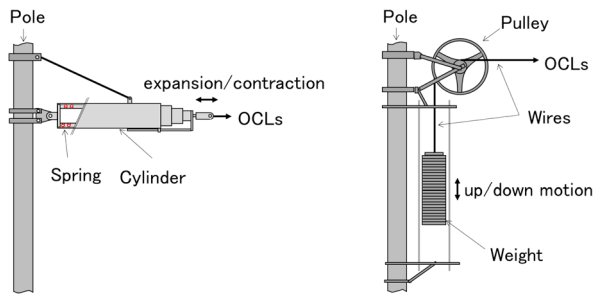

(a) Spring-type (b) Pulley-type

Fig. 2 Schematic diagram of tensioning devices

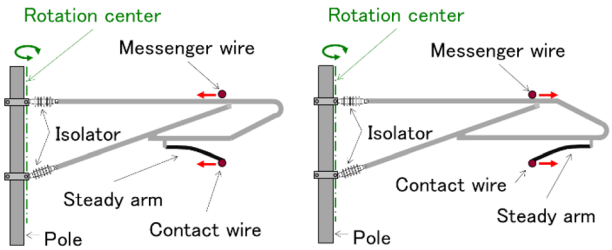

(a) Pull-off type (b) Push-off type

Fig. 3 Schematic diagram of hinged cantilevers (The red arrow indicates the direction in which the hinged cantilevers pulls the OCLs)

3. Analytical model

3.1 Overview

This paper focuses on cases where multiple wires are held at both ends by the same type of tensioning device via yokes. As shown in Fig. 4, the yoke is a metal fitting that holds two wires together, such as a messenger wire (upper wire in Fig. 1) and a contact wire (lower wire in Fig. 1). The tension distribution across the messenger wire and the contact wire can be adjusted by changing the distance from each attachment point to the tensioning device. For simplicity, this paper models the OCL in curved sections as follows (Fig. 5).

A) The messenger and the contact wires, which are held together via the yoke, are represented as a single wire.

B) The OCL represented by a single wire is modelled as a beam element, taking into account only axial thermal expansion and elastic deformation.

C) The OCL is divided into multiple elements with connection points to the tension devices and hinged cantilevers as nodes. These nodes are pinned to connect the OCL elements to each other, and to the tensioning devices and hinged cantilevers.

D) The tensioning devices are represented by linear springs.

E) The hinged cantilevers are represented by rigid bar elements.

F) The rotation centers of the bar elements of the hinged cantilevers are placed on the outside and inside of the curved track to represent the pull-off- and push-off-type.

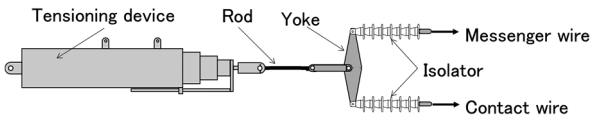

Fig. 4 Tensioning multiple wires together using a yoke

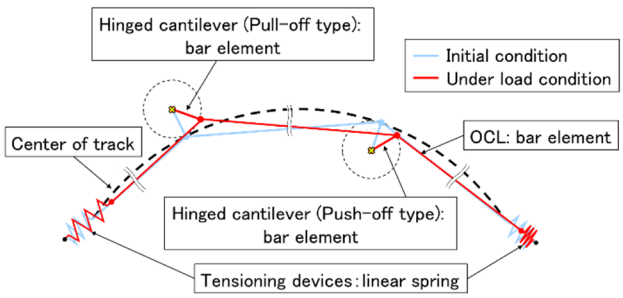

Fig. 5 An overview of simplified analytical model

Using Fig. 5, consider an OCL supported by N hinged cantilevers within the tensioning section. In this model, the types of hinged cantilevers (pull-off- and push-off-type) at the N points can be any combination. Furthermore, the center of the arc representing the curved track with radius R (indicated by the bold dotted line in Fig. 5) is set as **O**. The hinged cantilevers are numbered sequentially from the left side of the figure. The rotation center position of the i-th hinged cantilever is denoted as $\mathbf{O}_i$, the length of the hinged cantilever (called gauge length) is denoted as G_i, and the rotation angle is denoted as θ_i. The node corresponding to the connection point between the i-th hinged cantilever and the OCL is denoted as $\mathbf{P}_i$, and $\mathbf{P}_i$ for $\theta_i = 0$ is denoted as $\mathbf{P}i^{(0)}$. The point $\mathbf{P}_i$ is therefore constrained to move along a circular trajectory with a rotation center $\mathbf{O}_i$ and a rotation radius G_i. Note that the rotation angle θ_i is set to zero under the condition that the node is located at the point where the arc representing the curved track and the circle representing the rotation trajectory of the hinged cantilevers are tangent (the condition that the hinged cantilever is positioned perpendicular to the circular trajectory with radius R). The rotational direction in which the entire OCL shifts from left to right at the zero point is defined as positive. The tensioning devices on the left and right ends are assumed to have spring constants k_L and k_R, respectively. The direction of displacement of the entire OCL from left to right is defined as positive, and the extension of each spring is denoted as δ_L and δ_R, respectively. The nodes corresponding to the connection points between the tensioning devices and the OCL are denoted as $\mathbf{P}_0$ and $\mathbf{P}_{N+1}$ for the left and right sides, respectively. In particular, when $\theta_i = 0$ is satisfied for all hinged cantilever, δ_L and δ_R are defined as $\delta_L = 0$ and $\delta_R = 0$, and $\mathbf{P}_0$ and $\mathbf{P}_{N+1}$ under these conditions are denoted as $\mathbf{P}_0^{(0)}$ and $\mathbf{P}_{N+1}^{(0)}$. In this model, $\mathbf{P}_0$ and $\mathbf{P}_{N+1}$ are constrained in their motion by the straight lines $\mathbf{O}_L\mathbf{P}_1$ and $\mathbf{P}_N\mathbf{O}_R$, where $\mathbf{O}_L$ and $\mathbf{O}_R$ are the fixed points of the springs representing the tensioning devices.

The number of nodes is $N+2$ (i=0, 1, 2,…, N, $N+1$), and the line segment $\mathbf{P}_{i-1}\mathbf{P}_i$ is the length of the OCL between the i-th spans. Let this be L_i. This can be expressed by the following equation, which represents elastic deformation and thermal expansion.

$$L_i = L_i^{(0)}\left(1+\alpha\Delta t\right)\left(1+\frac{T_i}{EA}\right) \tag{1}$$

Here, $L_i^{(0)}$ is the length of the line segment $\mathbf{P}_{i-1}{}^{(0)}\mathbf{P}_i^{(0)}$. E, A, and α are the longitudinal elasticity coefficient, cross-sectional area, and linear expansion coefficient of the OCL, respectively. Δt and T_i are the temperature change from the reference temperature and the tension change from the reference tension T_0 in the i-th OCL element, respectively.

3.2 Geometric Constraints

Let the coordinates of $\mathbf{O}_i$, $\mathbf{P}_i^{(0)}$, $\mathbf{P}_i$, $\mathbf{O}_L$, and $\mathbf{O}_R$ be $(\bar{x}_i, \bar{y}_i)$, $(x_i^{(0)}, y_i^{(0)})$, (x_i, y_i), (x_L, y_L) and (x_R, y_R), respectively. The relationship between the coordinate values x_0, y_0, x_{N+1} and y_{N+1} of nodes $\mathbf{P}_0$ and $\mathbf{P}_{N+1}$ is expressed by the following equation based on the constraint conditions on the straight line connecting $\mathbf{P}_0$ and $\mathbf{P}_{N+1}$.

$$\begin{cases} y_0 = \dfrac{y_L - y_1}{x_L - x_1}x_0 - \dfrac{x_1 y_L - x_L y_1}{x_L - x_1} \\ y_{N+1} = \dfrac{y_N - y_R}{x_N - x_R}x_0 - \dfrac{x_R y_N - x_N y_R}{x_N - x_R} \end{cases} \tag{2}$$

The i-th (i=1, 2,…, N) node is constrained to move in a circular trajectory with rotation center $\mathbf{O}_i$ and rotation radius G_i, and is also constrained to move in a circular trajectory with radius L_i centered on the (i-1)-th node. These geometric constraints are expressed by the following equations.

$$\begin{gathered}(x_i - \bar{x}_i)^2 + (y_i - \bar{y}_i)^2 = G_i^2 \\ (i = 1, 2, \cdots, N)\end{gathered} \tag{3}$$

$$\begin{gathered}(x_i - x_{i-1})^2 + (y_i - y_{i-1})^2 = L_i^2 \\ (i = 1, 2, \cdots, N, N+1)\end{gathered} \tag{4}$$

Note that L_i in equation (4) are functions of T_i, and T_i are unknown variables.

3.3 Force balance condition

Let us then consider the equilibrium of forces at the nodes. From the equilibrium of forces at the nodes corresponding to the tensioning devices, we obtain the following equation.

$$\begin{cases} T_1 = -k_L\delta_L \\ T_{N+1} = k_R\delta_R \end{cases} \tag{5}$$

δ_R and δ_L are functions of the unknown variables x_0, y_0, x_{N+1}, and y_{N+1}, and are given by the following equations based on the constraint conditions of P_0 and P_{N+1} (eq. (2)).

$$\begin{aligned}\delta_L &= \sqrt{(x_0 - x_R)^2 + (y_0 - y_R)^2} \\ &\quad - \sqrt{(x_0^{(0)} - x_R)^2 + (y_0^{(0)} - y_R)^2} \\ \delta_R &= \sqrt{(x_{N+1} - x_L)^2 + (y_{N+1} - y_L)^2} \\ &\quad - \sqrt{(x_{N+1}^{(0)} - x_L)^2 + (y_{N+1}^{(0)} - y_L)^2}\end{aligned} \tag{6}$$

We then consider the equilibrium of forces in the tangential direction of the circle with center **O**i and radius G_i at the i-th node $\mathbf{P}_i$ (Fig. 6). Let ψ_i^L be the angle between the tangent at the i-th node $\mathbf{P}_i$ and the i-th OCL element, and let ψ_i^R be the angle between the tangent at the i-th node $\mathbf{P}_i$ and the (i+1)-th OCL element. The equilibrium condition of forces at the i-th node can be expressed by the following equation.

$$\begin{gathered}(T_i + T_0)\cos\psi_i^L = (T_{i+1} + T_0)\cos\psi_i^R \\ (i = 1, 2, \cdots, N)\end{gathered} \tag{7}$$

Here, ψ_i^L is a function of x_{i-1}, y_{i-1}, x_i, and y_i, and ψ_i^R is a function of x_i, y_i, x_{i+1}, and y_{i+1}, and are expressed by the following equation.

$$\begin{aligned}\cos\psi_i^L &= \frac{x_{i-1,i}\tilde{y}_i - \tilde{x}_i y_{i-1,i}}{\sqrt{x_{i-1,i}^2 + y_{i-1,i}^2}\sqrt{\tilde{x}_i^2 + \tilde{y}_i^2}} \\ \cos\psi_i^R &= \frac{-x_{i-1,i}\tilde{y}_i + \tilde{x}_i y_{i-1,i}}{\sqrt{x_{i-1,i}^2 + y_{i-1,i}^2}\sqrt{\tilde{x}_i^2 + \tilde{y}_i^2}} \\ x_{i-1,i} &= x_i - \bar{x}_i,\ y_{i-1,i} = y_i - \bar{y}_i \\ \tilde{x}_i &= x_i - \bar{x}_i,\ \tilde{y}_i = y_i - \bar{y}_i\end{aligned} \tag{8}$$

Note that x_{i-1}, y_{i-1}, x_i, and y_i are unknown variables.

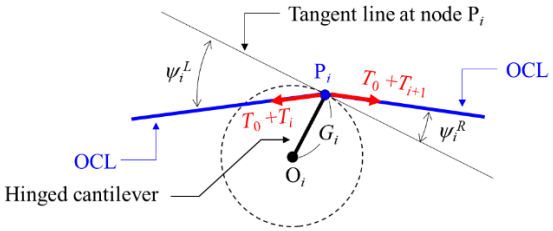

Fig. 6 Equilibrium of force at node P$_i$

4. Calculation method for equilibrium point

As shown in the previous chapter, the number of unknowns is $3N+5$, which is the sum of $2N+4$ (the x-coordinates and y-coordinates of each node) and $N+1$ (the tension change T_i of each OCL element). All of the unknowns can be obtained from the system of $3N+5$ simultaneous equations given by equations (2) to (5) and equation (7). From equations (2) to (5) and equation (7), function **H** and the unknown vector $\boldsymbol{\xi}$ are defined as follows.

$$\mathbf{H}=\begin{bmatrix} a_R x_0+b_R-y_0 \\ a_L x_{N+1}+b_L-y_{N+1} \\ (x_1-x_0)^2+(y_1-y_0)^2-L_1^2 \\ \vdots \\ (x_i-x_{i-1})^2+(y_i-y_{i-1})^2-L_i^2 \\ \vdots \\ (x_{N+1}-x_N)^2+(y_{N+1}-y_N)^2-L_{N+1}^2 \\ (x_1-\bar{x}_1)^2+(y_1-\bar{y}_1)^2-G_1^2 \\ \vdots \\ (x_j-\bar{x}_j)^2+(y_j-\bar{y}_j)^2-G_j^2 \\ \vdots \\ (x_N-\bar{x}_N)^2+(y_N-\bar{y}_N)^2-G_N^2 \\ T_1-k_R\delta_R \\ T_{N+1}+k_L\delta_L \\ (T_0+T_2)\cos\psi_1^L-(T_0+T_1)\cos\psi_1^R \\ \vdots \\ (T_0+T_{l+1})\cos\psi_l^L-(T_0+T_l)\cos\psi_l^R \\ \vdots \\ (T_0+T_{N+1})\cos\psi_N^L-(T_0+T_N)\cos\psi_N^R \end{bmatrix} \tag{9}$$

$$\boldsymbol{\xi}=[x_0 \ \cdots \ x_{N+1} \ y_0 \ \cdots \ y_{N+1} \ T_1 \ \cdots \ T_{N+1}]'$$

The prime (‘) represents transpose.

Finding the equilibrium point in this model is equivalent to finding $\boldsymbol{\xi}$ that satisfies the following equation.

$$\mathbf{H}(\boldsymbol{\xi})=0 \tag{10}$$

Equation (10) is a nonlinear system of equations, which is solved in this paper using iterative calculation based on the Newton method. First, an randomly set $\boldsymbol{\xi}^{(1)}$ is given as the initial value for iterative calculation, and the solution is corrected using eq. (11). The iterative calculation is performed until the error, as defined by eq. (12) becomes sufficiently small.

$$\boldsymbol{\xi}^{(k)}=\boldsymbol{\xi}^{(k-1)}-\left(\frac{\partial\mathbf{H}}{\partial\boldsymbol{\xi}}\right)^{-1}\mathbf{H}\left(\boldsymbol{\xi}^{(k-1)}\right) \tag{11}$$

$$e_1=\frac{1}{3N+5}\left\|\frac{\boldsymbol{\xi}^{(k)}-\boldsymbol{\xi}^{(k-1)}}{\boldsymbol{\xi}^{(k-1)}}\right\| \tag{12}$$

Here, the characters in the superscript (k) represent the k-th iterations, and $\|\bullet\|$ represents the squared norm. If the error fluctuates repeatedly during the iteration process and does not converge, refer to the reduced Newton method described in Reference [3], modify Equation (11) as follows to reduce the correction amount, and perform the next step of the iteration calculation.

$$\boldsymbol{\xi}^{(k)}=\boldsymbol{\xi}^{(k-1)}-\mu\left(\frac{\partial\mathbf{H}}{\partial\boldsymbol{\xi}}\right)^{-1}\mathbf{H}\left(\boldsymbol{\xi}^{(k-1)}\right)(\mu<1) \tag{13}$$

The derivative of function **H** in equations (11) and (13) are obtained by numerical differentiation. Note that the obtained solution may converge to either a stable or an unstable equilibrium point. To identify whether the obtained solution is a stable or an unstable equilibrium point, it can be distinguished by using the calculation method based on dynamic simulation shown in Reference [4].

5. Calculation example

Using the calculation method proposed in the previous chapter, we calculate the changes in the strokes of the tensioning devices at both ends due to temperature changes when multiple hinged cantilevers are installed in the tensioning section. First, we calculate the effects of arranging pull-off- and push-off-type hinged cantilevers in different sequences on the stroke of the tensioning device when the temperature increases by 20°C, for a tensioning section within a curved track with a radius of 4000 m (number of spans: 20, span length: 50 m for all spans, total OCL tension: 39200 N, gauge length 4 m for all hinged cantilevers). The effects of the sequence of arrangement of pull-off- and push-off-type hinged cantilevers on the strokes of the tensioning devices are shown in Fig. 7. Note that the OCL's linear expansion coefficient and the product of longitudinal elasticity coefficient and cross-sectional area were set to $\alpha = 1.7 \times 10^{-6}$ and $EA = 3.1 \times 10^7$, and the spring constant of the linear spring used as the tensioning device were set to $k_L = k_R = 6000$ (N/m). The calculation conditions were set to the following six conditions.

Condition 0: Straight tensioning section, with an alternating arrangement of pull-off- and push-off-type hinged cantilevers

Condition 1: Curved tensioning section, with an alternating arrangement of pull-off- and push-off-type hinged cantilevers

Condition 2: Curved tensioning section, with an arrangement of all push-off-type hinged cantilevers

Condition 3: Curved tensioning section, with an arrangement of all pull-off-type hinged cantilevers

Condition 4: Curved tensioning section, with an arrangement of push-off-type hinged cantilevers in the first half of the section and pull-off-type hinged cantilevers in the second half of the section

Condition 5: Curved tensioning section, with an arrangement of pull-off-type hinged cantilevers in the first half of the section and push-off-type hinged cantilevers in the second half of the section

In condition 1, where pull-off- and push-off-types are arranged alternately, no stroke difference is observed on either side of the tensioning devices, and the stroke amount is almost the same as that of the straight section. Conditions 2 to 5 correspond to the condi-

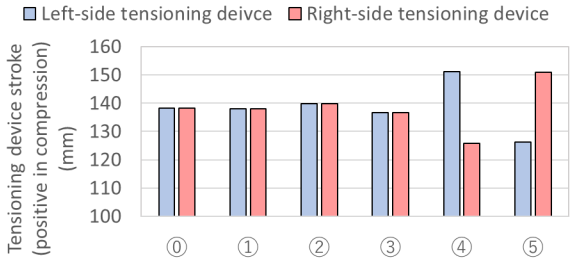

Fig.7 Calculation example of stroke variation in tensioning devices when temperature rises by 20°C above standard temperature (Influence of hinged cantilever arrangement)

tions for the occurrence of biased OCL longitudinal displacement described in Reference [1]. However, in cases 2 and 3, where push-off- or pull-off-type hinged cantilevers are arranged consecutively, no stroke difference is observed between the two sides, i.e., no biased OCL longitudinal displacement occurs. In conditions 4 and 5, where either pull-off- or push-off-type hinged cantilevers are continuously arranged on one half of the tensioning section, the stroke difference between the two sides is large, and it can be seen that the stroke amount is larger on the side where push-off-type hinged cantilevers are arranged consecutively.

Next, we considered cases where the curvature radius of the curve differs at the midpoint of the tensioning section for conditions 1 to 3 above. Specifically, we set the curvature radius of the first half of the tensioning section to 10,000 meters and varied that of the second half from 2,000 to 18,000 meters. The calculation results are shown in Fig. 8. As can be seen from Fig. 8, except when the pull-off- and push-off-type hinged cantilevers are arranged alternately, the greater the difference in curvature radius between the first and second halves, the greater the difference in stroke between the tensioning devices at both ends. It can also be seen that the smaller the curvature radius, the greater the difference in stroke between the tensioning devices at both ends.

The calculation results in Fig. 7 and 8 suggest that differences in the 'sequence of arrangement of hinged cantilevers (pull-off- and push-off-type)' and 'track conditions (curve radius)' within the tensioning section affect the difference in the stroke of the tensioning devices when they differ between the first and second halves of the tensioning section.

Figure 9 shows the relationship between the OCL longitudinal displacement x due to the rotation of the hinged cantilever at the support point, and the force F acting parallel to the track on the OCL caused by the displacement x. This relationship is given by the following eq. (1).

$$F = \pm \frac{T_0 L}{RG} x \quad (+: \text{pull off}, -: \text{push off}) \tag{14}$$

Here, L is the span length on both sides of the hinged cantilever under consideration (in this equation, both sides are assumed to be equal), R is the curve radius, and G is the rotation radius of the hinged cantilever under consideration. From equation (14), it can be seen that in the case of a pull-off-type hinged cantilever, the force acts to return the hinged cantilever to its original position in response to the OCL longitudinal displacement, while in the case of a push-off-type hinged cantilever, the force acts so as to make the hinged cantilever to rotate more.

Equation (14) is in the form of 'force = coefficient × displacement,' and the part of $(T_0L)/(RG)$ can be regarded as the spring

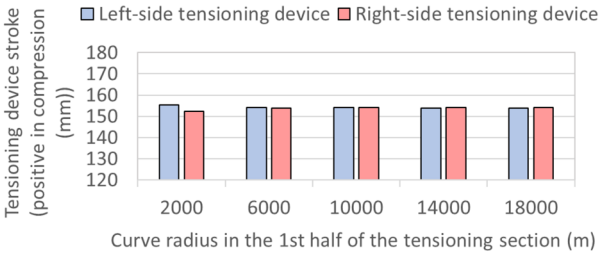

(a) Alternate arrangement of pull-off and push-off type hinged cantilevers

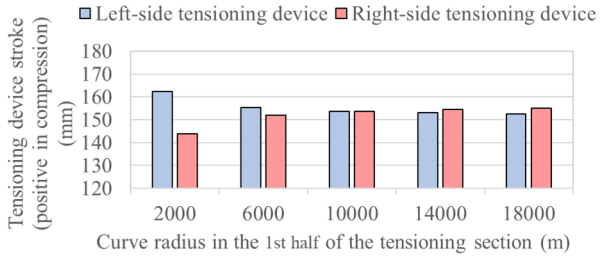

(b) All push-off type hinged cantilevers

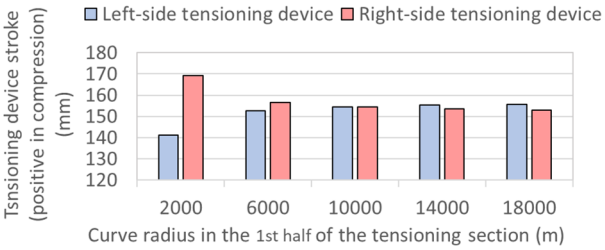

(c) All pull-off type hinged cantilevers

Fig. 8 Calculation example of stroke variation in tension adjustment devices when temperature rises by 20°C from the standard temperature (Influence of asymmetry in track curvature radius within the tensioning section)

***Curvature radius of the left-hand half of the tensioning section is 10,000m**

constant. Therefore, the pull-off- and push-off-type hinged cantilever can be considered to act as springs with positive and negative spring constants, respectively, with respect to the OCL longitudinal displacement. Furthermore, it can be seen that the absolute value of the spring constant is determined by the span length, curve radius, rotational radius of the hinged cantilever, and tension. Therefore, it can be considered that within the tensioning section, in addition to the tensioning devices at both ends, spring elements are distributed at each support point. From the results of Fig. 8 and 9 and eq. (14), it is suggested that a difference in stroke between the tensioning devices at both ends occurs when the spring constants of the spring elements within the tensioning section are distributed asymmetrically with respect to the center of the tensioning section.

In the calculation examples shown in Fig. 8 and 9, the amount of deviation in the OCL longitudinal displacement of the tracks is not particularly large. However, the distribution of spring constants of the spring elements within the tensioning section, which is determined by the curvature radius, the rotational radius of the hinged

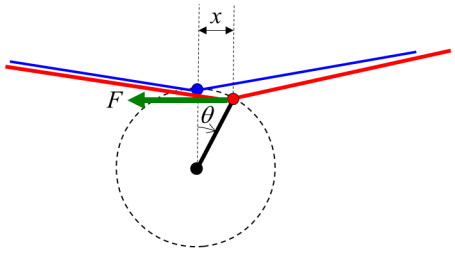

Fig. 9 Displacement and restoring force of the OCL in the direction parallel to the track during rotation of a hinged cantilever

cantilever, and the span length, may be asymmetrical relative to the center of the tensioning section. There may also be significant individual differences between the tensioning devices at both ends [2]. These factors can result in differences in the stroke of the tensioning devices on both sides, which may lead to a case that one of the tensioning devices may reach its stroke limit. The insights gained from the modelling presented in Chapter 3 and the calculation methods presented in Chapter 4 are considered useful when evaluating the hinged cantilever arrangement sequence during design or when countermeasures are deemed necessary to address the biased OCL longitudinal displacement. These insights can help to determine the most effective arrangement sequence of hinged cantilever and the optimal installation positions for anti-creep devices to suppress temperature-induced biased OCL longitudinal displacement. Additionally, this calculation method is useful when replacing hinged cantilevers at appropriate angles during its replacement, taking into account temperature expansion and contraction.

6. Conclusion

In this paper, we have constructed an analytical model to express the OCL longitudinal displacement on curved tracks, including tensioning devices and hinged cantilevers, and have proposed a calculation method to determine the equilibrium point of the OCL longitudinal displacement.

In the future, this calculation method will be used to elucidate phenomena such as biased OCL longitudinal displacement. Tensioning devices and hinged cantilevers are equipment designed to maintain the tension of OCL as uniformly as possible within the tensioning section and to maintain good current collection performance. Therefore, it is most important to investigate the effects of temperature changes not only on the OCL longitudinal displacement, but also on the tension distribution of OCL within the tensioning section and on current collection performance. This is an important challenge for the future. Furthermore, the structure in which multiple wires constituting the OCL are each tensioned by separate tensioning devices, as well as individual differences in the tensioning devices, including friction, are also considered to influence the OCL longitudinal displacement and the tension distribution in the tensioning section. Therefore, improving the model and calculation methods to account for such factors will be a future challenge.

References

[1] Japan Railway Electrical Engineering Association, *Introduction to Electricity for Railway Engineers-Overhead Contact Line Series 3: Overhead Contact Line Equipment*, pp. 109-112, 2003 (in Japanese).
[2] Sato K., Yamashita Y., Suwa, K. and Kawamoto, K., A Study on Creeping move of Overhead Contact Line and Movement of its Neutral Point, *The Institute of Electrical Engineers of Japan-Industry Applications Society-Transportation and Electric Railway/Linear Drives Joint Workshop*, pp. 41-46, 2022 (in Japanese).
[3] Sugihara, M. and Murota, K., *Mathematics of Numerical Methods*, Iwanami Shoten, pp. 75-76, 1994.
[4] Yoshitaka Y., Koki S., "Calculation method of equilibrium points for OCL in the longitudinal degrees of freedom," *Transactions of the JSME*, Vol. 90, No. 932, 2024.

Authors

Yoshitaka YAMASHITA, Dr.Eng.
Senior Chief Researcher, Head of Current Collection Laboratory, Railway Dynamics Division
Research Areas: Current Collection System, Vibration Control, Measurement

Koki SATO
Senior Researcher, Contact Line Structures Laboratory, Power Supply Technology Division
Research Areas: Contact Line Structures, Simulation

Summaries of Papers in RTRI REPORT (in Japanese)

Method for Estimating Causes of AI Decision-making Errors in Train Forward Surveillance

Nozomi NAGAMINE, Wataru GODA

(Vol.39, No.11, 1-10, 2025.11)

In the railway industry, there is a growing trend of using AI and camera images to automate various tasks that were previously performed visually. However, when considering the future application of AI in safetycritical operations such as autonomous driving, it is essential to investigate the causes of AI decision-making errors. Therefore, we have developed a tracing method for train-forward surveillance systems that estimates the causes of AI decision-making errors, such as missed detections, at three stages: input images, AI structure, and training data. This paper reports the developed method for estimating the causes of AI decision-making errors and its verification results.

Prediction Method for Fatigue Strength of Corroded Rails Using Actual Stress and Stress Gradient

Jun MIZUTANI, Riku TAKAYAMA, Tadashi DESHIMARU, Mitsuru HOSODA, Yoshihiro TERASHITA, Ryuichi YAMAMOTO

(Vol.39, No.11, 11-20, 2025.11)

Rail corrosion, especially in humid environments, accounts for around 20% of rail breaks in Japan. However, traditional methods for predicting the fatigue strength of corroded rails, such as using corrosion thickness and S-N curves, have limitations. The study involved collecting corroded rails, scanning their surface profiles, and applying finite element analysis to evaluate stress at breaking points. A new method using stress and stress gradients was proposed to predict the number of load cycles required for corroded rails to break in bending fatigue tests, with an estimated range of 0.5 to 2 times.

Effect of Ground and Structure Damping on Combination of Inertia Force and Ground Displacement in Seismic Deformation Method

Niki TANAKA, Kimitoshi SAKAI

(Vol.39, No.11, 21-29, 2025.11)

The seismic response values of pile foundation structures are calculated using the seismic deformation method, which uses inertia force and ground displacement. This paper presents a study that aims to achieve a highly accurate estimation of the combination of inertia force and ground displacement. Specifically, dynamic analyses were conducted for various types of grounds and structures under conditions where either damping was varied. The combination coefficients of the actions were then compiled and discussed. The result clarified that the combination coefficients of the actions change with the damping of the grounds and structures. Using this trend of change, a simple formula has been proposed to calculate the combination coefficient of the actions, taking into account the effect of damping. Using the proposed method, it is possible to set more appropriate coefficients than before, taking into account the damping effects on the ground and structure.

Long-Term Installation Test of Head-Hardened Rails for Reducing Rolling Contact Fatigue on High Rails in Curved Sections

Yoshikazu KANEMATSU, Yoshihiro TERASHITA

(Vol.39, No.11, 30-37, 2025.11)

Head-hardened rails (HH340) are characterized by reduced wear compared to standard as-rolled rails. As a result, they extend the replacement life of rails due to wear on high rails in curved sections. However, HH340 can develop rolling contact fatigue (RCF) damage in the form of gauge corner cracks. Therefore, to reduce both wear and RCF damage, several new types of head-hardened rails have been developed and its resistance to damage was evaluated in long-term installation tests. These tests showed that some of the developed rails exhibited less wear than standard as-rolled rails. Moreover, fewer horizontal cracks that could develop into gauge corner cracks than HH340 rails.

Application Conditions of the Simplified Calculation Method for the Impact Factor of Steel and Composite Structures

Manabu IKEDA, Munemasa TOKUNAGA, Yusuke KOBAYASHI

(Vol.39, No.11, 38-45, 2025.11)

The application conditions of the simplified calculation method for the impact factors of steel and composite structures were studied, with a view to relaxing some of them. As a result, it was reconfirmed that the current application conditions are reasonable. For simply supported composite girders, the impact factors calculated using the simplified calculation method were compared with those calculated through the standard calculation method for concrete structures. It was confirmed that the relative magnitudes of these calculated impact factors vary depending on the girder span, natural frequency and train speed.

Evaluation Method for the Risk of Scouring based on Case Studies of Railway Bridge Piers damaged by Scouring

Satoshi WATANABE, Shoma FUJIWARA, Ikumasa YOSHIDA

(Vol.39, No.12, 1-13, 2025.12)

In order to optimize the maintenance and management of railway bridges to mitigate scouring disasters that threaten the safety and stability of railway transport, it is crucial to appropriately assess the risk of localized scouring occurring at bridge piers. In this study, we propose an indicator to represent the risk of scouring. This indicator was determined by calculating the dimensionless tractive forces acting on the riverbed from hydrological statistics recorded during scouring disasters, then comparing and organizing the results between disaster-affected and non-affected conditions. As a result, we found a consistent linear relationship between the normalized scouring force and the root penetration ratio when in the event of disasters.

Development of Equipment to Remove Black Leaf Layer Formed on Rail Top Surface by Fallen Leaves

Masaharu KONO, Tatsuya IDO, Masahiro TSUJIE, Junichi SUZUMURA, Kazuki IKOMA

(Vol.39, No.12, 14-22, 2025.12)

On mountain railways in autumn, a black leaf layer is formed when fallen leaves are stepped on by wheels, containing moisture. This layer tends to reduce adhesion in wet conditions, resulting in wheel spinning or sliding. Our focus was on the chelating effect of citric acid, and we verified its effectiveness in removing the black leaf layer. We then proposed a method of removing the black leaf layer involving spraying citric acid, sliding a brush and cleaning with water, and developed equipment for carrying out these procedures. Following test on a commercial line using this equipment, we confirmed that it had sufficient performance to remove the black leaf layer.

Proposal of Evaluation Metric for Train Rescheduling and Analysis and Evaluation Method for Train Rescheduling Arrangements

Mayu TAKADA, Taketoshi KUNIMATSU, Shunichi TANAKA

(Vol.39, No.12, 23-31, 2025.12)

To support dispatchers in their traffic rescheduling operations during transport disruptions, the authors propose the concept of "number of late-arriving passengers," develop a new operational adjustment simulator, and propose an analysis method for evaluating the impact of implemental adjustment plans on passenger convenience. Specifically, each item is as follows: Firstly, the "number of late-arriving passengers" is used as an evaluation metric for comparing different traffic rescheduling plans, representing the number of passengers whose arrival delay at a station exceeds a threshold. Secondly, the train rescheduling simulator predicts timetables based on different rescheduling arrangements. Finally, the proposed method for analysis uses the number of late-arriving passengers to determine which period and section of travel convenience has changed due to changes in traffic rescheduling arrangements. In this paper, we describe the three items mentioned above in detail.

A Survey on Switch-and-Lock Equipment Maintenance and Utilization of Point Machines Monitors

Shunsuke SHIOMI, Yoshikazu OSHIMI, Sohei SHIGEMORI

(Vol.39, No.12, 32-40, 2025.12)

We carried out a survey on maintenance methods for switch-and-lock equipment in order to search for future research and development. Actual states of facility conditions were investigated through a questionnaire and interview survey to 87 railway operators in Japan. The specific survey items were maintenance methods, maintenance cycles, replacement criteria, benefits of point machine monitoring systems and its tasks. The results of this survey showed that the condition monitoring data from point machines has been used to extend the inspection periods and reduce the number of inspection items. Furthermore, we also confirmed that R&D on condition monitoring may contribute to help today's maintenance issues, such as a shortage of maintenance workers.

Comparison of Driver's Line of Sight Distribution during Commercial Train Operation by GOA2.5 Automatic and Manual Systems

Chizuru NAKAGAWA, Hajime AKATSUKA, Takahiko AOYAGI, Ayaka FUJII

(Vol.39, No.12, 41-48, 2025.12)

A comparative study of driver gaze allocation during automatic and manual operation on a demonstration train was conducted to verify whether the forward gaze allocation during automatic operation is equivalent to that during normal manual operation. We measured the forward gaze allocation of three drivers on test trains and 15 drivers on commercial trains and analyzed eleven of them. The results showed that 10 of the 11 drivers had the same or greater forward gaze allocation during automatic operation as during manual operation.

Detectability of Residual Stress Anomalies in Various Types of Railway Wheels Subjected to Thermal Overload Based on Back Gauge Change

Kazuyuki HANDA

(Vol.40, No.1, 1-10, 2026.1)

Temperature increases of railway wheels due to frictional braking on the wheel tread can lead to maintenance challenges such as tread wear and thermal cracking. While heating within the anticipated design range should not adversely affect the structural safety of the wheels, excessive temperature rises resulting from brake system failures can induce tensile residual stresses in the rim, potentially leading to wheel fracture. Detecting wheels with abnormal residual stresses is therefore crucial for railway safety, and monitoring residual displacements in the rim due to changes in circumferential residual stresses is an implementable approach. However, the shape of the wheel web varies, and the displacement response to thermal input differs depending on the wheel geometries. This study aims to explore general deformation behaviours related to wheel shape and elucidate the relationship between shape and heat resistance. The elastic-plastic finite element analysis employing simplified intense thermal input revealed that residual deformation after excessive thermal loading consistently results in back gauge expansion, although the deformation and stress responses differ based on the web geometry. Differences in heat resistance are indicated by the variation in the temperature at which compressive yielding due to thermal stress occurs, depending on the web shape. The residual stress detectability of each wheel is determined based on the principle that greater residual displacement at lower stress indicates higher anomaly detectability.

Characterization of Instrumented Wheelset Considering Contact Condition between Wheel and Rail

Takayuki TANAKA, Shoya KUNIYUKI

(Vol.40, No.1, 11-20, 2026.1)

Instrumented wheelsets are widely used for measuring wheel loads and lateral forces acting between wheel and rail. These forces are fundamental quantities in the context of running safety assessment of railway vehicles. Authors proposed a testing apparatus in order to clarify characteristics of strain output of instrumented wheelset which depend on the contact condition acting between wheel and rail. This paper describes some results of characteristic tests conducted using this apparatus. The aim of the tests was to confirm two aspects: the validity of the estimated force by the instrument wheelset, and the validity of an assumption generally utilized in the safety assessment against flange climbing.

Ground Displacement Analysis Method for Chemical Grouting Capable of Estimating Fracturing Grouting Conditions

Yudai YAMASHITA, Takashi NAKAYAMA, Takahiro ISHII

(Vol.40, No.1, 21-28, 2026.1)

With the increasing utilization of underground spaces, the demand for chemical grouting around existing structures has been rising. This makes the control of ground displacement during grouting operations increasingly important. Therefore, a numerical analysis method capable of estimating ground behavior prior to construction is required. This study extends a numerical prediction model, previously limited to permeation grouting, to include fracturing grouting. The proposed method is validated through comparison with the results of water injection tests. The final section presents the results of a parametric study using the proposed model.

A Method for Visualizing Passenger Flow Data from a Passenger Distribution Estimation System in Railway Stations

Ginga TSUSHIMA, Mitsutaka ISHIZUKI, Munenori SHIBATA

(Vol.40, No.1, 29-36, 2026.1)

Monitoring passenger flow in real time within railway stations enables congestion points to be identified effectively, contributing to enhanced station safety management. We verified the estimation accuracy of a passenger distribution estimation system developed beforehand using real video footage recorded within railway stations. As a result, it was confirmed that the system can capture origin-destination (OD) traffic volume trends with a high degree of accuracy. Additionally, we visualized real-time passenger distributions to estimate the passenger flow and verified that the developed

system can generally reproduce the actual dynamics of passenger flow in real time.

Fatigue Life Evaluation of Aged Rails Focusing on The Occurrence State of Hanging Sleepers and Rail-Head Surface Irregularities

Mitsuru HOSODA, Nobutaka TAKAHASHI, Tadashi DESHIMARU

(Vol.40, No.1, 37-46, 2026.1)

This study analyzed the gap under hanging sleepers and the surface irregularities of rail heads obtained on the operating railway track, which affect the fatigue life of aged rails. Fatigue tests were conducted on aged rails exhibiting surface irregularities and on aged rails with a history of being laid on hanging sleepers. On the basis of the fatigue test result, we proposed a quantitative evaluation method for the safety and control value of aged rails for extended use. This method reflects the probability of hanging sleepers, as well as the variability of the fatigue strength of aged rails.

Influence of Smoothness in Skeleton Curve of Railway Bridge and Viaduct on Nonlinear Response Spectrum

Kimitoshi SAKAI

(Vol.40, No.1, 47-56, 2026.1)

This study investigates how the smoothness of the skeleton curve affects the seismic response of a structure before it yields. The bulging of the skeleton curve was characterized by the ratio of initial stiffness in a bilinear model, followed by numerous nonlinear dynamic analyses. The results showed that, for ductility $\mu = 1$, the ratio of the required demand yield seismic coefficient drops below 1 when the natural period of the structure (T_{eq}) is short, reducing the seismic response values. The findings of this study can be applied to seismic response for structures. Particularly, they are expected to improve the accuracy and rationalization of structural behavior before and after yielding, specifically the structural behavior during Level 1 earthquakes and the immediate estimation of structural integrity after an earthquake.

Configuration Proposal of an On-vehicle Insulation Diagnostic Device for Superconducting Maglev Propulsion Coils Using Partial Discharge Detection

Satoru OTA, Ryohei IKEDA, Minoru NAKASHIMA

(Vol.40, No.1, 57-66, 2026.1)

Ground coils are essential components of superconducting maglev systems. Propulsion coils, a category of ground coils, require rigorous insulation diagnostics to withstand mechanical, electrical, and environmental stresses, strong dynamic electromagnetic interactions, and high voltages. This paper reviews the requirements for insulation diagnostics of propulsion coils, emphasizing previously developed efficient methodologies. One such methodology is an advanced diagnostic system that analyzes electromagnetic waves from partial discharges to evaluate coil deterioration and identify discharge locations. Following the discussion, we propose a device design that enables real-time diagnostics to be carried out directly from the vehicle, enhancing operational efficiency and reducing the size of necessary installations.

QUARTERLY REPORT of RTRI

第 67 巻　第 1 号
2026 年 2 月 1 日　発行
監修・発行所：公益財団法人鉄道総合技術研究所
〒 185-8540　東京都国分寺市光町 2-8-38
発行人：芦谷公稔
問い合わせ：鉄道総研広報

Vol. 67, No. 1
Published date: 1 February 2026
Supervision/Publisher: Railway Technical Research Institute
Address: 2-8-38 Hikari-cho, Kokubunji-shi, Tokyo 185-8540, Japan
Issuer: Dr. Kimitoshi ASHIYA
Contact us: Public Relations, Railway Technical Research Institute
Mail Address: rtripr@rtri.or.jp

QUARTERLY REPORT of RTRI

RAILWAY TECHNICAL RESEARCH INSTITUTE

Printed in Japan